Resonant Acoustic Rheometry for High-Throughput, Non-Contact Mechanical Characterization of Viscoelastic Biomaterials

by

Eric Charles Hobson

A dissertation submitted in partial fulfillment
of the requirements for the degree of
Doctor of Philosophy
(Biomedical Engineering)
in the University of Michigan
2021

Doctoral Committee:

Professor Cheri X. Deng, Co-Chair
Professor Jan P. Stegemann, Co-Chair
Professor J. Brian Fowlkes
Professor Andrew J. Putnam

Eric C. Hobson

hobsone@umich.edu

ORCID iD: 0000-0001-7889-900X

Acknowledgements

I would first like to thank my doctoral advisors, Dr. Cheri Deng and Dr. Jan Stegemann for your continual support during my time as a graduate student. Your patience and trust as I shifted directions midway through the Ph.D. was invaluable, working with me to develop a project that I could be truly passionate about. I am deeply appreciative of your guidance, helping me to grow into a more capable and confident researcher. You have both demonstrated a great mixture of curiosity and pragmatism, helping me to both overcome and learn from any roadblocks I encountered in my research, and I hope to take some of that mindset with me into the future.

In addition to my advisors, I would like to thank my dissertation committee members, Dr. Andrew Putnam and Dr. Brian Fowlkes. Your question and insights helped to direct my focus, improve the quality of my final doctoral work, and inspired future directions for my research. I would also like to thank the members my qualifying committee, Dr. Kelly Arnold, Dr. Brandon Baker, Dr. Bethany Moore, and Dr. Ariella Shikanov, for not only advice on the proposal itself, but for helping to teach me how to design and communicate a cohesive research plan.

Special thanks go out to all of my current and former lab mates in the Deng and Stegemann laboratories. To Dr. Adeline Hong, Dr. Ram T. Annamalai, and Dr. Zhenzhen Fan, thank you for all your help getting me started on my project, freely giving your time and expertise. To Dr. Weiping Li, Nick Schott, Nicole Friend, Chuma Nweke, Christina Hendren, Dr. Brandon Walters, Dr. Che-Yu Lin, and Dr. Shiying Liu, I really appreciate all the discussion we have had and all the help you have given me over the years.

I also want to thank Dr. Kelly Arnold for her guidance and support at the start of my PhD, and while I ultimately changed research directions, my time in her lab was invaluable, helping me to develop new skills and interests that I am sure will be a large part of any future career. I am also deeply appreciative of the everyone I worked with in the Arnold and Shea laboratories: Dr. Katy Norman, Melissa Lemke, Dr. Joseph Decker, Dr. Matthew Hall, Dr. Robert Oakes, Dr. Jeffrey Liu, Dr. Kevin Hughes, Dr. Richard Youngblood, Dr. Dominique Smith, and many other.

I have been lucky to work with some amazing collaborators during my PhD. To Dr. Nicole Edwards, Dr. Benjamin Levi, Dr. Carlos Aguilar, Jesus Castor-Macias, and Dylan Neale, I am very thankful for the opportunities I had to work with all of you. I learned so much from our work together and enjoyed these opportunities to broaden my research experiences.

I also want to thank all the members of the Histotripsy Group for their generosity with their time and expertise; hopefully, I can help return the favor one day. I am also indebted to the wonderful BME staff here at UM. To Maria Steele, Kathleen Crumb, Pat Metzler, Chuck Nicholas, Erik Keup, Dana Jackson, and the rest of the staff, thank you so much for all you have done for me and every other student lucky enough to work with you.

Finally, I want to thank everyone who has supported me outside the lab. To my friends, thank you for all the fun times over the years, helping me to not always take things too seriously. To my Parents, Keith and Lisa, and my brother, Sean I am so grateful for all your encouragement and support over the years. Last, but definitely not least, I want to thank my partner, Patricia. You were always there to support and motivate me during the most difficult times. I know I would never have made it to this point without your help.

Table of Contents

Chapter 2 Development and Validation of Resonant Acoustic Rheometry (RAR) 32

List of Figures

List of Appendices

List of Abbreviations

°C	Celsius
2D	Two-dimensional
3D	Three-dimensional
ADE	Acoustic droplet ejection
A-mode	Amplitude mode
ARF	Acoustic radiation force
ARFI	Acoustic radiation force impulse
B-mode	Brightness mode
D10	DMEM with 10% FBS
DI	Deionized
DMEM	Dulbecco's modified Eagle's medium
DMSO	Dimethyl sulfoxide
DT	Dithiol
ECM	Extracellular matrix
FBS	Fetal bovine serum
FDA	Food and Drug Administration
FEA	Finite element analysis
FUS	Focused ultrasound
Gelapin	Gelatin crosslinked with genipin
HIFU	High intensity focused ultrasound
HWHM	Half width at half maximum
LAL	Limulus Amebocyte Lysate
LAP	Lithium phenyl-2,4,6-trimethylbenzoylphosphinate
LOB	Limit of blank
LOD	Limit of detection
LPS	Lipopolysaccharide
MLR	Multiple linear regression
NB	Norbornene
PBS	Phosphate buffered saline
PEG	Polyethylene glycol
PLSR	Partial least squares regression
PRF	Pulse repetition frequency
RAR	Resonant acoustic rheometry
RF	Radiofrequency
rRAR	Rapid resonant acoustic rheometry
SEER	Sonic estimation of elasticity via resonance
SWEI	Shear wave elasticity imaging
TEG	Thromboelastography
UV	Ultraviolet light

Abstract

Mechanical testing of viscoelastic biomaterials is of critical importance in biomedical engineering, enabling basic research into the role of the extracellular matrix, investigatory and diagnostic testing of tissues and biofluids, and the development and characterization of tissue engineered therapeutics. Conventional material testing approaches used for soft biomaterials generally require force application through direct contact with a sample, leading to potential contamination and damage, and thereby limiting these approaches to end-point measurements. To overcome these limitations, we have developed a new measurement technique, Resonant Acoustic Rheometry (RAR), which enables high-throughput, quantitative, and non-contact viscoelastic characterization of biomaterials, soft tissues, and biological fluids.

RAR uses ultrasonic pulses to both generate microscale perturbations and measure the resulting resonant oscillations at the surface of soft materials using standard labware. Resonant oscillatory properties obtained from the frequency spectra of the surface oscillations, including the resonant frequency and the damping coefficient, are used to quantify material properties such as shear modulus, shear viscosity, and surface tension in both viscoelastic solids and liquids.

We developed a prototype RAR system and tested it on a range of soft biomaterials, with shear moduli ranging from under 100 Pa to over 50 kPa, including fibrin, gelatin, and polyethylene glycol (PEG). Shear moduli measured using RAR were validated both computationally using finite element analysis and experimentally using conventional shear rheometry, with excellent linear correlation in measured elasticity between techniques ($R^2 > 0.95$). By performing parallel RAR experiments using microwells of different sizes, we verified that resonant oscillatory behaviors

could be used to quantify the intrinsic viscoelastic properties of a material. We also demonstrated the rapid, non-contact monitoring of changes in material properties over a variety of temporal scales, ranging from processes occurring on the order of milliseconds to those occurring over hours and days. High temporal resolution RAR measurements, with sampling intervals as low as 0.2 seconds, were used to characterize the gelation process. Characteristic features of the resonant surface waves during phase transition were applied to identify the gel point for various hydrogels. High sample throughput was demonstrated by performing longitudinal RAR testing to explore the impact of hydrogel polymer and crosslinker concentration on both reaction kinetics and final mechanical properties in full factorial experiments consisting of over 15,000 unique measurements. We were able to identify individual effects of design parameters as well as interactions that led to unexpected mechanical properties, demonstrating the importance of combinatorial methods and high-throughput mechanical characterization in material design.

These studies demonstrate that RAR can rapidly and accurately assess the mechanical properties of soft viscoelastic biomaterials. The measurements generated are analogous to those produced using conventional mechanical testing, and RAR is further capable of longitudinal viscoelastic studies over time. RAR applies automation in both data collection and analysis, allowing high throughput measurement of an array of samples without contact or the need for manual intervention. Furthermore, RAR uses standard microwell plates, which simplifies sample preparation and handling. The viscoelastic properties of soft biomaterials are relevant in a wide range of applications, including for clinical diagnostic assays and the development of hydrogel materials for regenerative medicine. RAR represents a fast, accurate, and cost-effective method for materials characterization in these applications.

Chapter 1 Introduction

1.1 Motivation

The mechanical properties of the cellular microenvironment have been identified as an important regulator of cellular phenotype. Thus, mechanical characterization of biological tissues or engineered tissue constructs is important for both basic scientific research and engineering applications. Compared to the testing of metals or stiff materials, mechanical quantification of viscoelastic biomaterials can be particularly challenging due to their relatively low elastic modulus, time-dependent mechanical response, and biphasic structure [1]. Conventional material testing approaches used for soft biomaterials include tension, compression, indentation, and shear-based methods. These techniques generally require physical contact with a sample, which can lead to contamination and damage, limiting such approaches to end-point measurements without the ability to track temporal changes longitudinally. This is problematic, as the properties of cell-supporting matrix are not static and undergo continuous change due to cell-mediated mechanical forces and remodeling. In addition, the relevance of quantitative assessment of soft materials has been recognized in a wide range of fields including tissue engineering, regenerative medicine, bioprinting, as well food sciences. The objective of this dissertation is to develop a new technique suitable for longitudinal mechanical characterization of soft biomaterials to meet these needs.

With the capability of penetrating tissue non-invasively, ultrasound elastography techniques, such as acoustic radiation force impulse (ARFI) imaging and shear wave elasticity imaging (SWEI), have provided a non-invasive strategy to assess tissue stiffness in a clinical setting. These techniques demonstrated the utility of ultrasound as an invasive approach to assess tissue properties, however, these techniques are generally semi-quantitative and require large tissue volumes, thus are not applicable to the quantification of small, viscoelastic samples in applications requiring repeated and high throughput examinations [2].

The motivation behind this dissertation was to develop a new technique that addresses the unmet needs for tissue engineers and biomaterials researchers to measure the viscoelastic properties of their materials in a manner that was non-destructive and readily applicable to their experimental methodologies using standard labware and sample volume/size. We determined that an acoustic method would be most effective as ultrasonic waves are able to efficiently propagate through both biomaterial samples and labware, enabling the non-contact generation and measurement of deformation. This thesis establishes a solid foundation towards accomplishing that goal, detailing the development and applications of a novel method, Resonant Acoustic Rheology (RAR), for the non-contact characterization of soft, viscoelastic materials.

1.2 Conventional material testing approaches

While differing in the specific mechanism of action, conventional approaches for testing the mechanics of soft biomaterials all apply some type of deformation to a sample, applying force in tension, compression, or rotation using direct contact.

1.2.1 Tensile testing

Tensile mechanical testing is used for a wide variety of materials [3–7]. Commonly utilizing a universal testing machine (UTM), samples are affixed to two points and then are stretched, measuring the generated tensile force as a function of strain. This testing is relevant in soft tissues, such as tendon, ligament [7], skin [6], and muscle [8], where the primary forces exerted in-situ are in tension. From the stress-strain curves it is not only possible to determine the Young's modulus from the slope of the linear region, but to identify the material's yield stress and ultimate tensile strength where, respectively, the deformation becomes plastic and eventually breaks [1,9]. Additionally, many biomaterials have strain-stiffening or strain-softening behavior, driven by their fibrous microstructure, which can be characterized by the stress-strain relationship [10,11]. The viscous properties of materials can also be obtained from tensile material testing, applying repeated stress-strain cycles to quantify hysteresis, or holding an elevated strain and measuring stress relaxation [3,6,12].

1.2.2 Compression testing

Compressive testing can be performed in a similar fashion to tensile testing, axially compressing a sample and measuring the resulting normal force. Through compressive testing it is also possible to measure the Young's modulus, and for isotropic Hookean materials this should be the same as that measured via tensile testing [9]. However, due the fibrous structure of many soft biomaterials, the assumption of isotropic linear elasticity, may be inaccurate, with prior literature indicating significant differences in elastic moduli with load in different directions [13]. It is also possible to identify the material's yield stress and ultimate compressive strength at the point the material fractures or deforms plastically beyond a certain threshold. In addition to unconfined compression, with samples compressed between two non-porous platens, samples may be confined between a porous platen and non-porous container, allowing for poroelastic characterization [14–16].

1.2.3 Indentation

While conventional compression testing applies force evenly across the entire surface of a sample, alternative approaches utilize the forced indentation of a material surface to measure the mechanical properties [1]. A wide variety of indentation methods exist, utilizing probes of various geometries to measure materials with a wide stiffness and over a range of sizes [17–20]. Unlike tensile and compression testing methods that require a controlled material geometry in order to accurately measure bulk properties, indentation testing can be performed on a variety of irregular surfaces, only measuring the mechanical properties in the vicinity of the probe [1]. At the smallest scales, such as with acoustic force microscopy, measurements can be performed on individual cells or on individual fibers in a fibrous material [21–23]. Because of the localization of indentation measurements, this technique has been applied to measure spatial heterogeneity in a variety of native tissues and engineered biomaterials [24–26]. Indentation methods have also been demonstrated to be suitable for high-throughput testing, where indentation can be rapidly applied to an array of materials [27–31].

1.2.4 Shear Rheometry

In addition to compressive and tensile forces applied in the axial direction, shear forces can be used to deform and characterize the mechanical properties of soft materials. Shear rheometry can be performed using a wide variety of experimental designs including, parallel plates [32–34], cone and plate [35,36], and pin and cup geometries [37,38], intended for liquid or solid materials with a range of viscoelastic properties. For purely viscous liquids, a constant shear rate can be applied with the resulting shear stress enabling the calculation of the material viscosity. Testing for viscoelastic materials, both solid and liquid, is often performed using sinusoidal oscillating strains [1]. The stresses due to shear elasticity are proportional to the shear strain, while the viscous stress is proportional to the shear rate. This results in a phase shift between the imposed shear strains and the measured stresses that is used to calculate the elastic and viscous components of the material, defined as the storage modulus (G') and loss modulus (G'') respectively [39].

The strain and frequency dependence of the viscoelastic material properties can be explored with shear rheometry using sweeps adjusting the amplitude and rate of the shear oscillations [32,33,40]. Changes in the viscoelastic material properties over time can also be explored by repeating the oscillatory measurements either continuously or at regular intervals [41–43]. The ability to measure the viscoelastic properties of both solid and liquid materials over time has made shear rheology a particularly important technique in the study of gelation. Modifications to this measurement modality have been developed for a variety of specialized applications, such as thromboelastography for the characterization of blood coagulation [38,44,45]. While most commonly applied in shear rheometry, frequency-based methods or dynamic mechanical characterization (DMA) can also be implemented with other testing modalities [19,46,47].

A review of literature shows that shear rheometry has been successfully applied to characterize the viscoelastic properties of all materials used in our RAR studies (Chapters 2-4), including fibrin [33,48], gelatin [49,50], agarose [34,40,51], polyethylene glycol (PEG) [52,53], and coagulin gels. The demonstrated capabilities of this technique in relevant materials, combined with the ability to measure both solid and liquid phases during gelation, led us to determine that shear rheometry was the closest conventional analogue to RAR. Therefore, in Chapter 2 we utilized shear rheometry to validate viscoelastic RAR measurements in both mechanically stable and dynamic states.

1.2.5 Measurement of spatial mechanical heterogeneity

In many cases it is beneficial to not only characterize the bulk mechanical properties of a material, but to measure the localized mechanical properties. Medical imaging techniques currently in clinical use, such as ultrasound elastography or magnetic resonance electrography can allow for 2D and even 3D mapping of tissue mechanics, enabling the detection and diagnosis of tumors, cysts, or other diseases affecting the mechanics of soft tissue [2]. Measuring mechanical heterogeneity at the cellular scale is of critical importance in tissue engineering, enabling further understanding of cellular interaction with the extracellular matrix. As mentioned previously, some conventional mechanical testing techniques, such as AFM and nanoindentation, have been applied to measure material mechanical properties with microscale resolution [24–26]. While effective for superficial 2D measurements, these approaches are limited by the need for contact to only probing the surface of a material. Non-contact approaches have been developed to overcome some of these limitations, by allowing for 3D longitudinal measurements of materials undergoing dynamic cellular remodeling. A common strategy involves the application of some type of embedded marker to track microscale deformations that can either be passively generated through cellular remodeling, as with traction force microscopy [10], or can be actively generated using a localized force, as in optical or acoustic tweezers [48,54–57].

1.2.6 Limitations of current approaches

Despite the biological relevance of the tensile testing modality, it can be very challenging to implement with soft biomaterials. Adhesive or clamping methods for affixing samples are ineffective for many hydrogels, requiring extensive sample preparation or the development of custom experimental jigs [1]. Slipping or tearing at the contact points can introduce significant error [58]. While samples do not need to be fixed to the testing apparatus for compressive or shear testing, the sample geometry does need to be carefully controlled, with flat, parallel surfaces at the top and bottom to make complete contact with the platen [59]. Additionally, the low elastic moduli of some biomaterials may result in inaccurate force measurement in testing platforms not specifically designed for extremely soft materials [1,19]. The mechanical properties of biomaterial samples, including soft tissues and hydrogels, can be highly dependent on their hydration, requiring environmental controls or the ability to perform measurements in liquid chamber, increasing the complexity of each test [16,58]. The application of strain to biomaterials samples can introduce significant mechanical changes, often necessitating the introduction of preconditioning protocols, applying low levels of cyclic strain until the materials' viscoelastic properties stabilize. The mechanical properties of preconditioned materials may differ significantly from the unconditioned state, complicating comparison of measured properties between studies with different preloading protocols [3,6,7].

While the methods described above serve important roles in the mechanical characterization of biomaterials, all these approaches require some type of contact with a sample. This introduces the potential to contaminate or damage the material, often limiting these to short-time series or end-point measurements in a study [60]. To minimize this limitation, it is critical to develop non-contact methods for mechanical testing.

1.3 Ultrasound Elastography

A variety of non-contact testing modalities have been exploited using optical, acoustic, or magnetic forces [21,48,54–57]. Ultrasound approaches offer an advantageous strategy for mechanical measurement. Ultrasound is widely used as a non-destructive, non-ionizing modality in medical imaging [60-61]. Ultrasonic pulses can penetrate and propagate in soft tissues, and the scattering or reflection by local inhomogeneity and variation in acoustic impedance along the line of sight may be used to determine the location and properties of the scatterers [61–64]. Specifically, backscattered signals, or echoes, of a single pulse can be used to generate a 1D amplitude mode (A-mode) image of a single axial line through a material, with the timing and characteristics of individual reflections corresponding to the axial positioning of features within the material. A series of A-lines shifted in lateral position or angle can be rapidly generated to form a 2D brightness mode (B-mode) image in a plane parallel to the direction of sound propagation. B-scan images are the most common imaging mode used in clinical sonography, enabling the real-time visualization of tissue structure and morphology. Repeated A-mode or B-mode acquisitions can also be applied to observe motion within tissues in motion mode (M-mode) [65,66].

Ultrasound elastography is an ultrasound imaging modality that detects spatial variation in tissue stiffness based on the difference in internal deformation upon externally applied mechanical compression. These deformations or strains are determined from the temporal shifts of backscattered signals, which correspond to the locations of internal targets before and after the applied compression [2].

1.3.1 Strain Elastography/ARFI

The simplest version of ultrasound elastography, strain elastography, uses a manual compression from an external pad or the transducer itself in contact with the tissue surface [67–69], as shown in Figure 1.1. A 2D strain map is generated for the tissues, allowing for the qualitative measurement of spatial stiffness heterogeneity, where higher local strains indicate a region of lower stiffness and vice versa. While this approach can detect stiffness heterogeneity in a tissue, it generally cannot provide absolute quantitative measures of the intrinsic properties of a material because the stress field cannot generally be predicted in a complex spatial environment [67]. Additionally, because this technique relies on manual force input from a sonographer it suffers from low repeatability and high variability between users.

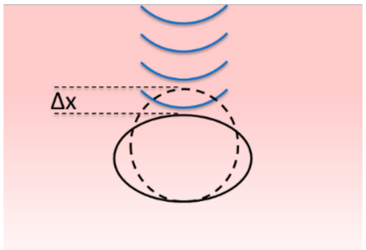

Figure 1.1: Schematic of strain elastography. Blue arcs represent ultrasonic pulses applied to measure axial deformation, Δx.

Acoustic radiation force impulse (ARFI) imaging utilizes longer higher intensity ultrasonic pulses, often from the same transducer used for imaging, to induce a body force, called acoustic radiation force (ARF), to generate internal deformation in tissue [2,70,71]. A-mode tracking pulses are performed before and after ARF pushing or deformation, and a strain distribution along the line of sight is generated in the same manner as conventional ultrasound strain elastography. Pushing and tracking pulses are repeated at different positions to generate 2D elastograms, showing the spatial variation in strain at some time following the push [68]. The use of ARF to generate internal deformation in place of manual compression from the surface of tissue, called remote palpation, may reduce the user variability, but this form of ultrasound elastography is not without limitations.

While the manual pressure used in strain elastography will result in a static strain, ARF pulses induce only a short duration of stress, with the strain returning to baseline shortly after the pushing pulse ends. The kinetics of creep during the pushing pulse and the recovery afterwards can be used to quantify the viscous material properties [69]. A variety of methods have been developed to characterize these kinetic differences, utilizing both the single and multiple pushing pulses [72–75].

As with strain elastography, measurements of stiffness are generally qualitative as the accurate modeling of a stress field within heterogenous tissues with complex geometry can pose a significant challenge. Additionally, the high-intensity pulses used to generate deformations may cause heating both at the transducer and within the tissue [76–78]. Not only is the increase in temperature damaging to tissue and engineered biomaterials, but it can also alter the material properties such as elastic modulus and the speed of sound. To mitigate this effect, it is necessary to limit the duration and framerate of ARFI imaging.

ARFI imaging has had a significant impact in clinical diagnostics as a non-invasive modality to evaluate tissue stiffness, with important applications in the detection of cancer, fibrosis, and heart disease [79–81]. Despite the success of this technique in demonstrating the application of ARF for non-invasive tissue compression, it requires large tissue volume (on the order of centimeters). However, these parameters are not suitable generally for biomaterial testing.

1.3.2 Shear-Wave Elastography Imaging

Shear wave elastography imaging (SWEI) detects shear waves traveling through a material to measure a material's mechanical properties [67,82,83]. Shear waves are generated using a localized ARF pulse and travel radially outward. The speed of these shear waves is measured using a time-of-flight measurement taken some distance from the origin point of the waves, as shown in Figure 1.2. Shear modulus estimates can then be calculated from the shear wave speed according to $c^2\rho = G$, where c is the speed of sound, ρ is the density, and G is the shear modulus [84–86]. Viscous materials properties can also be quantified by measuring the attenuation of propagating shear waves [85,87–89].

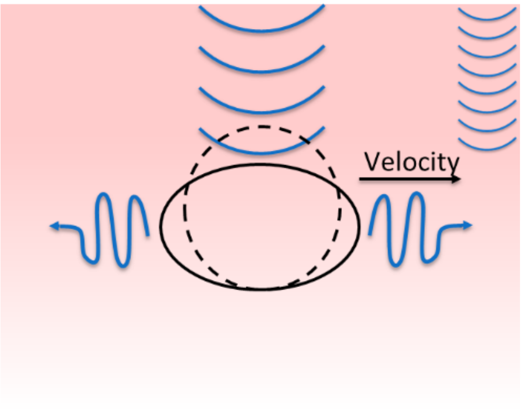

Figure 1.2: Schematic of shear wave elastography. Large blue arcs represent high intensity ultrasonic pulses applied to generate shear waves, and smaller arcs represent the imaging pulses used to measure the shear wave velocity.

While capable of providing quantitative measurement of tissue modulus, overcoming the qualitative limitations of strain elastography and ARFI, SWEI still generally requires large tissue volumes on the order of several centimeters so that the traveling shear waves may be detected and measured without boundary effects, like other clinical ultrasound imaging modalities [90]. Thus, it is not suitable for quantitative assessment of small biomaterial samples.

1.4 Soft Biomaterials

A wide variety of hydrogels have been developed or used within the field of tissue engineering. Here we provide a brief discussion of a few of these material systems that were used in RAR testing, including fibrin, gelatin, agarose, coagulin, and PEG gels.

1.4.1 Natural Biomaterials

Fibrin is a protein essential for hemostasis and thrombosis. It is important for wound healing as well as several other biological functions and pathological conditions involving extracellular matrix (ECM) [91]. During tissue and vascular injury, fibrinogen, a glycoprotein complex that is made in the liver and circulates in the blood, is converted enzymatically by thrombin into fibrin and then a fibrin-based blood clot. Interaction of fibrinogen and thrombin, a serine protease, transforms the liquid solution into a gel meshwork of viscoelastic soft solid characteristics. This gelation occurs in two stages, enzymatic and non-enzymatic. In the enzymatic stage, thrombin cleaves two small peptides, fibrinopeptides A and B, from fibrinogen, forming monomeric fibrin [92]. Monomeric fibrin will then spontaneously self-assemble in a staggered format to form two-stranded protofibrils. Finally, the protofibrils will aggregate laterally to form larger fiber of variable thickness and branching, making up the structure of a fibrin clot [93]. During coagulation *in vivo* this fibrin mesh will be furthered stabilized through covalent crosslinking driven by Factor XIII, a transglutaminase [94]. The unique polymerization mechanism of fibrin allows control of gelation times and network architecture; thus, a range of soft substrates may be formed with tissue-like viscoelastic properties [95]. Fibrin gels are also widely used for fabrication of hydrogel-based cellular scaffolds for tissue engineering and regenerative medicine applications [4,48,96,97]. Assessment of the dynamic changes of the rheological features of fibrin gels may provide insights regarding the complex blood coagulation process and exploration of fibrin as a versatile biomaterial with tunable biochemical and mechanical properties.

Gelatin, formed from the hydrolytic degradation of collagen, has been used for centuries to form gels, long before the advent of tissue engineering [49]. Gelatin has been primarily used in the food industry, acting as a thickener and stabilizer in wide variety of foods [98]. Beyond culinary applications, gelatin is used extensively in tissue engineering, being used in the development of biomimetic platforms that can replicate a wide variety of soft tissues [99]. The precise structure of gelatin polypeptide will vary depending on the source of collagen, as well as the degradation method, but is almost always very thermally responsive. Above ~35-40°C gelatin will generally dissolve and form a solution in water, with lightly crosslinked flexible peptide chains. When cooled below this temperature, the gelatin polypeptide will revert to a more collagen-like helical structure and will form a solid gel [49]. Because gelatin is not stable near physiological temperatures, it is often necessary to form covalent crosslinks between peptide chains, resulting in an increase in the thermal stability and mechanical strength [98]. Crosslinking using bifunctional crosslinkers, like glutaraldehyde or genipin, or using an enzyme, such as transglutaminase has been demonstrated to be effective in altering the mechanical and thermal behavior of gelatin [99–101].

The Limulus Amoebocyte Lysate (LAL) assay is the current FDA standard for the detection and quantification of endotoxin, utilizing the unique immune response of horseshoe crabs where the presence of endotoxin initiates an enzymatic cascade leading to the formation of a solid coagulin gel [102]. The detection of endotoxin in drugs or biomedical implants is critical for patient safety. Endotoxin, or lipopolysaccharide (LPS), are fragments of the cell membrane of gram-negative bacteria. While no longer pathogenic, these fragments are capable of driving a significant innate immune response, leading to severe and potentially fatal symptoms, including fever, diarrhea, and septic shock [103]. The cascade is initiated when endotoxin binds to and activates the enzyme factor C. Activated factor C activates factor B, which in turn cleaves the inactive proclotting enzyme into the active clotting enzyme [104]. The aptly named clotting enzyme is then responsible for cleavage of the hemolymph protein coagulogen to form coagulin, which is polymerizes into the long macromeric chains necessary for the formation of a solid clot [102]. Due to the role as the initiator of clotting cascade, small increases in endotoxin can drive substantial changes in the rate of formation of a solid coagulin gel. Although different in purpose, defense as opposed to hemostasis, this process is mechanistically analogous to the mammalian clotting cascade forming a solid fibrin network [105].

While the materials describe above are all proteinaceous in structure, polysaccharide gels, like agarose, have also been used extensively in tissue engineering. Agarose is extracted from algae, and like gelatin forms a thermal setting gel. However, unlike gelatin which melts or sets reversibly around the same temperature, agarose displays a setting-melting hysteresis, setting around 35°C, but only melting or dissolving at much higher temperatures, often greater than 80°C [34]. Agarose has been demonstrated to be biologically inert, however, it does not have moieties for cell attachment, such as Arg-Gly-Asp (RGD) peptide sequence for integrin binding, requiring modification or addition to support the growth of adherent mammalian cells [106]. Compared to the fibrous structure of fibrin and gelatin, agarose gels have a much more homogenous network structure with smaller pore sizes [107–109].

1.4.2 Synthetic Biomaterials

Polyethylene glycol (PEG) hydrogels represent an important class of synthetic hydrogels [110]. Unlike natural materials, synthetic hydrogels can allow for the independent tuning of a wide variety of mechanical and chemical properties [10]. Changes to the density, length, branching, or cross-linking in the polymeric backbone can all dramatically affect the viscoelastic properties of the hydrogel [111]. While fundamentally biologically inert, these matrices can be chemically modified, such as providing binding sites for the adhesion of cells or attachment of signaling molecules and adding degradable moieties for cellular remodeling, enabling controlled interaction between the cells and their synthetic ECM environment [52,112,113].

Photopolymerization provides an attractive strategy for the fabrication of PEG hydrogels by allowing for crosslinking with a high degree of spatial and temporal control. Due to this versatility, these materials have been used in a wide variety of 3D cell culture applications as a modular artificial ECM. They have also shown efficacy in 3D bioprinting, with precise temporal control of crosslinking enabling rapid gelation only after extrusion of the prepolymer solution [114]. Substantial research has shown the benefits of photopolymerization reactions using thiol and norbornene groups, where the crosslinking reaction is rapid and highly cytocompatible, requiring low free-radical concentrations and a physiological pH [53]. In order to maximize the viability of cell, encapsulated in these hydrogels, is important to characterize the kinetics of a crosslinking reaction, minimizing the exposure of cells to damaging UV light and generated free radicals. RAR is an excellent tool for this application, with the non-contact experimental system allowing for easy UV irradiation and the use of extremely short pushing impulses enabling mechanical sampling rates sufficient to monitor reactions occurring in just a few seconds.

1.5 Resonant Acoustic Rheology

Similar to how a musician tests the tuning of a drum, striking the surface and listening to the generated resonant tones, RAR generates and detects resonant surface oscillation in a material (Fig. 1.3A).

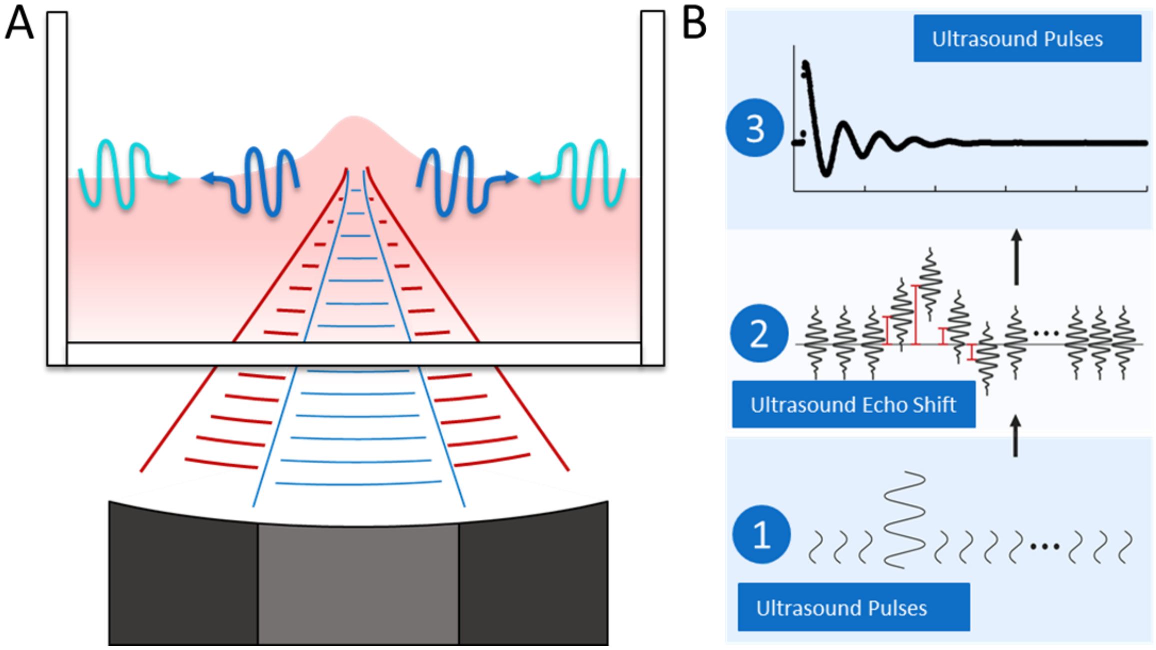

Figure 1.3: A) Schematic of RAR. Large red arcs represent the high intensity ultrasonic pulses generating surface waves and the blue arcs represent pulses used to detect motion. Blue waves are those generated by the initial perturbation, and the teal waves are those reflecting from the boundary. B) RAR experimental protocol, showing 1) a series of tracking pulses with a single push, 2) a representation of shifting surface reflections in collected A-lines, and 3) a calculated displacement time-series.

Modeled as a damped harmonic oscillation, the resonant phenomenon is used to characterize the mechanical properties of soft biomaterials. RAR takes advantage of the rigid, cylindrical wells of the plastic microplates often used in cell culture and tissue engineering applications, applying the ARF of a focused ultrasound pulse to generate an initial surface perturbation at the sample center which leads to surface waves traveling outward, reflecting off the rigid boundaries, and establishing standing 2D surface waves that are radially symmetric through interference (Fig. 1.3A). Specifically, RAR utilizes synchronized ultrasound pulses to not only generate deformation via ARF but also to track the resonant oscillations on the surface of soft biomaterials using pulse-echo ultrasound signals, as shown in Fig.1.3B. As with the ARF driven perturbation, ultrasound pulses used for motion estimation are targeted at the center of the sample surface, where the amplitude of the resonant oscillations is greatest. The characteristics of these resonant surface waves, such as frequency and damping, can be used to calculate viscoelastic material properties, including shear modulus and viscosity [115,116]. RAR is completely non-contact, can be performed in a wide variety of sample materials, and takes only a fraction of a second to perform each measurement [42].

1.5.1 Resonance-based techniques

Several techniques have exploited the use of ultrasound induced resonant phenomena for mechanical characterization. Sonic Estimation of Elasticity via Resonance (SEER) utilizes a resonant shear waves to measure evolving viscoelastic properties during blood coagulation [90]. This technique is used by Hemosonics (https://hemosonics.com/) in their Quantra Hemostasis Analyzer. Blood samples are added to proprietary cartridge system that warms the blood, mixes it with reagents to induce or alter coagulation, and moves it to a conic test chamber where an ultrasound pulse is applied to generate resonant oscillation of the sample volume via the ARF. Although the force application in SEER also utilizes the ARF of an ultrasound pulse, the technique is fundamentally different from RAR, because SEER activates the whole sample through shear forces in the sample volume, while RAR specifically induce and detects surface waves of a sample. Shear waves propagation is driven by elastic forces, limiting this technique to measurements of blood once it has developed an elastic fibrin network. Additionally, ultrasonic tracking of shear waves requires acoustic scattering elements in samples (like blood cells) and would be unable to generate measurements in homogenous materials.

A recent development by Rheolution (https://rheolution.com/) established a technique, called viscoelastic testing of bilayered materials (VeTBiM), which utilizes a custom cylindrical sample holder with a soft elastomeric bottom [41]. Resonant surface oscillations are generated external vibration of the entire holder, and the resonant oscillations of the bilayer construct are measured from the bottom using an optical sensor. The technique is limited by the requirement of these custom sample holders, with their highest throughput system limited to 3 samples at a time. In contrast, RAR uses integrated ultrasound systems for both generation and detection of resonant surface oscillations, enabling the use of standard labware for high-throughput operations.

1.5.2 ARF applied to air-liquid surface

Acoustic droplet ejection (ADE) methods use an ultrasonic toneburst directed through the bottom of a microwell plate to apply localized force due to the ARF of the ultrasound field at the surface [117]. When the ARF exceeds the surface tension and gravity, a droplet of liquid may be generated. ADE techniques use the ARF of the ultrasound pulse to expel nanoliter and picoliter droplets of liquid from the well. While the operation objective of ADE is completely different from that of RAR, a study exploited the use of an ADE system and patented by the company (EDC Biosystems, now acquired by Beckman Coulter, Inc.) for assessing the surface tension and viscosity of liquids by generating a surface perturbation and calculating the surface tension from the oscillation frequency and viscosity from the exponential decay [118,119]. However, this study treated the liquid surface oscillation as a vibrating membrane, not as actual waves on a fluid surface, and calculated the surface tension as $\sigma = \rho c^2$, where ρ is the density of the membrane and c is the wave phase velocity. While treating the liquid surface as a membrane may provide a simplistic model, it did not capture the physical mechanisms of surface waves on liquid and determination of the density and the thickness of a liquid surface was also problematic. Instead of a membrane, the surface wave on a liquid should be described by capillary waves with the dispersion relation of $\omega^2 = \frac{\sigma k^3}{\rho}$, where the angular frequency, ω, and wavenumber, k. Utilizing the dispersion relation, as well as the surface wave phase velocity of $c = \frac{\omega}{k}$, the correct formula for surface tension is calculate as $\sigma = \frac{\rho c^2}{k}$.

In contrast, RAR fully incorporates the surface hydrodynamics analysis of surface waves both in liquid and viscoelastic solids in the treatment of surface waves and oscillations. By generating and detecting resonant surface waves, we develop RAR to not only quantify viscoelastic liquid properties, but also characterize the viscoelastic behavior of solid materials.

1.5.3 Surface hydrodynamics

There is an extensive body of literature exploiting surface hydrodynamics to study mechanical properties of liquid and soft materials [115,116,120–123]. Excited surface wave methods typically generate travelling surface waves using thermal, electrical or direct mechanical perturbations and measure the timing and spatial profile of the waves using laser profilometry or optical imaging, finding the speed (c), wavelength (λ), and damping (Γ) [115,116,121]. Light scattering methods, such as surface quasi-elastic light scattering, detect the surface modes resulting from thermally driven surface roughness [94,96]. However, these techniques generally avoid wave reflections at boundaries and are limited to large surface areas and requires integrations of multiple instruments [115]. While long history of investigations generated significant progress regarding surface hydrodynamics [123], these previous studies were also restricted to slow operation and low throughput. In Chapters 2 and 3 we provide a detailed description of the integration of hydrodynamic models in the RAR method.

1.5.4 Advantages of RAR

Sample Flexibility

By utilizing the air interface above our samples, we are able to gain a number of key benefits. The air-liquid or air-solid interface behaves as a near perfect reflector. The acoustic radiation force generated by reflection at the interface is much greater than that generated by absorption within a material, allowing for higher localized displacements with lower acoustic intensities. The pressure at the surface of a perfect reflector will be $\frac{2I}{c}$, which is double the pressure in the case of perfect absorption, $\frac{I}{c}$, where I is the temporal average intensity and c is the speed of sound [63]. The hydrogels and soft materials that have, and will be, tested using RAR will be far from perfect absorbers, resulting in far lower applied forces. The only exception to this may be in the case of extremely thick samples, where attenuation due to both scattering and absorption may reduce the surface intensity to a degree that the pressure due to reflection no longer dominates the body force described by $\frac{2\alpha I}{c}$, but this is unlikely in any real material in a conventional microplate geometry [2]. Additionally, the high intensity reflections from the interface provide a very high signal-to-noise ratio for tracking displacement.

Another important benefit of our approach is eliminating the need for absorbing and scattering elements in a material. Most ultrasound elastography approaches, including the SEER method, rely on absorption in a material to generate acoustic radiation force for internal displacements and scattering elements in the material, such as cells, to generate echoes that can track these displacements [66,124]. RAR can measure materials regardless of absorption and scatterers, giving use much greater flexibility in the materials we measure.

A key benefit of our technique is being able to measure properties of materials in both solid and liquid states. This is particularly important when exploring material transitions, like the coagulation of blood. Shear waves from internal displacements, as used in SWEI and SEER, can only be generated and tracked in solid materials. Surface waves, on the other hand, can be generated on both solid and liquid materials, and we are able to look at waves propagating due to the elasticity (Rayleigh Waves), surface tension (Capillary Waves), or a combination of the two (Pseudocapillary Waves) [116,122].

Microplate Compatibility

The transducers used in RAR are attached to a 3D motion platform, allowing for the automated control of transducer position relative to a microplate affixed to a custom stage. This motion system allows for rapid movement, enabling high-throughput testing in microplates with as many as 96 samples. This motion system is flexible, allowing for testing of multisample arrays of any geometry or arrangements with only small changes to the automation script required.

It is essential for the transducer to be aligned at the center of the cylindrical sample to generate radially symmetric resonant waves [89]. Taking advantage of the imaging capabilities of ultrasound, an automated protocol was developed, using echoes from pulsed ultrasound to locate the edges of the well and calculating the exact center of each well from these positions. This method can account for translation, rotation, and warp in plates that would otherwise result in inaccurate measurements. Reflections from the surface of samples are used to perfectly align the focal point of the transducer with the sample surface. This allows for the system to compensate for small differences in sample thickness that might otherwise skew results.

1.6 Dissertation structure

A thorough explanation of the RAR theory and methodology is presented in Chapter 2. The independence of RAR measurements from ARF pulse parameters was verified in hydrogels of various stiffness. An FEA model of acoustic stimulation was also developed to predict the modes of resonant oscillation and enable the calculation of viscoelastic material properties. The viscoelastic measurements generated in RAR were validated using shear rheometry for measurements of stable fibrin, gelatin, and agarose gels, as well as for fibrin gels during the process of gelation. The major content of Chapter 2 has been published in a peer-reviewed journal [42].

Chapter 3 of this dissertation presents an expanded exploration of the liquid to solid transition during hydrogel gelation using RAR. This chapter demonstrates the capability of RAR to identify, and utilize, multiple varieties of surface waves to quantify viscoelastic material properties during a multistage transition from liquid to solid. The transition was observed in natural and synthetic hydrogel systems at multiple timescales. Finally, viscoelastic phenomena were identified during the phase transition and applied to the development of a quantitative gel clot LAL assay. A manuscript that contains the content of this chapter is in preparation.

A key difference between RAR and any conventional material testing methodology is the sample throughput capability of this non-contact technique. Chapter 4 highlights the potential for rapid, non-contact measurements to enable combinatorial viscoelastic testing of dynamic materials. This potential is demonstrated through model systems of crosslinked fibrin and gelatin hydrogels, systematically uncovering the interconnected roles of polymer concentration, gelation kinetics, crosslinking kinetics, and crosslinking mechanism. A manuscript including results from this chapter is in preparation.

Chapter 5 summarizes the key findings from Chapters 2, 3, and 4, providing further explanation on how RAR, as demonstrated in these studies, may be able to improve material testing capabilities in a variety of fields. Finally, we discuss future applications, where high-throughput non-contact measurement may be particularly consequential, as well as the continued technical development of RAR, aiming to improve the efficiency and flexibility of this system.

1.7 References

[1] M.L. Oyen, Mechanical characterisation of hydrogel materials, Int. Mater. Rev. 59 (2014) 44–59. https://doi.org/10.1179/1743280413Y.0000000022.

[2] K. Nightingale, Acoustic Radiation Force Impulse (ARFI) Imaging: a Review, Curr. Med. Imaging Rev. 7 (2012) 328–339. https://doi.org/10.2174/157340511798038657.Acoustic.

[3] G.A. Holzapfel, G. Sommer, C.T. Gasser, P. Regitnig, Determination of layer-specific mechanical properties of human coronary arteries with nonatherosclerotic intimal thickening and related constitutive modeling, Am. J. Physiol. Circ. Physiol. 289 (2005) H2048–H2058. https://doi.org/10.1152/ajpheart.00934.2004.

[4] S.L. Rowe, S.Y. Lee, J.P. Stegemann, Influence of thrombin concentration on the mechanical and morphological properties of cell-seeded fibrin hydrogels, Acta Biomater. 3 (2007) 59–67. https://doi.org/10.1016/j.actbio.2006.08.006.

[5] J.L. Drury, R.G. Dennis, D.J. Mooney, The tensile properties of alginate hydrogels, Biomaterials. 25 (2004) 3187–3199. https://doi.org/10.1016/j.biomaterials.2003.10.002.

[6] D. Remache, M. Caliez, M. Gratton, S. Dos Santos, The effects of cyclic tensile and stress-relaxation tests on porcine skin, J. Mech. Behav. Biomed. Mater. 77 (2018) 242–249. https://doi.org/10.1016/j.jmbbm.2017.09.009.

[7] L. Schatzmann, P. Brunner, H.U. Stäubli, Effect of cyclic preconditioning on the tensile properties of human quadriceps tendons and patellar ligaments, Knee Surgery, Sport. Traumatol. Arthrosc. 6 (1998) 56–61. https://doi.org/10.1007/s001670050224.

[8] D.A. Sleboda, T.J. Roberts, Incompressible fluid plays a mechanical role in the development of passive muscle tension, Biol. Lett. 13 (2017). https://doi.org/10.1098/rsbl.2016.0630.

[9] B.D. Ratner, A.S. Hoffman, F.J. Schoen, J.E. Lemons, Biomaterials Science, Elsevier, 2013. https://doi.org/10.1016/C2009-0-02433-7.

[10] M.S. Hall, F. Alisafaei, E. Ban, X. Feng, C.-Y. Hui, V.B. Shenoy, M. Wu, Fibrous nonlinear elasticity enables positive mechanical feedback between cells and ECMs, Proc. Natl. Acad. Sci. U. S. A. 113 (2016) 14043–14048. https://doi.org/10.1073/pnas.1613058113.

[11] S. Munster, L.M. Jawerth, B.A. Leslie, J.I. Weitz, B. Fabry, D.A. Weitz, Strain history dependence of the nonlinear stress response of fibrin and collagen networks, Proc. Natl. Acad. Sci. 110 (2013) 12197–12202. https://doi.org/10.1073/pnas.1222787110.

[12] D. Schuppan, M. Ruehl, R. Somasundaram, E.G. Hahn, Matrix as a modulator of hepatic fibrogenesis, Semin. Liver Dis. 21 (2001) 351–372. https://doi.org/10.1055/s-2001-17556.

[13] A.S.G. Van Oosten, M. Vahabi, A.J. Licup, A. Sharma, P.A. Galie, F.C. MacKintosh, P.A. Janmey, Uncoupling shear and uniaxial elastic moduli of semiflexible biopolymer networks: Compression-softening and stretch-stiffening, Sci. Rep. 6 (2016) 1–9. https://doi.org/10.1038/srep19270.

[14] E.K. Danso, P. Julkunen, R.K. Korhonen, Poisson's ratio of bovine meniscus determined

combining unconfined and confined compression, J. Biomech. 77 (2018) 233–237. https://doi.org/10.1016/j.jbiomech.2018.07.001.

[15] S. Kalyanam, Poro-Viscoelastic Behavior of Gelatin Hydrogels Under Compression-Implications for Bioelasticity Imaging, J. Biomech. Eng. 131 (2009) 081005. https://doi.org/10.1115/1.3127250.

[16] M. Galli, K.S.C. Comley, T.A. V Shean, M.L. Oyen, Viscoelastic and poroelastic mechanical characterization of hydrated gels, J. Mater. Res. 24 (2009) 973–979. https://doi.org/10.1557/jmr.2009.0129.

[17] M. Griffin, Y. Premakumar, A. Seifalian, P.E. Butler, M. Szarko, Biomechanical characterization of human soft tissues using indentation and tensile testing, J. Vis. Exp. 2016 (2016) 1–8. https://doi.org/10.3791/54872.

[18] J.D. Kaufman, C.M. Klapperich, Surface detection errors cause overestimation of the modulus in nanoindentation on soft materials, J. Mech. Behav. Biomed. Mater. 2 (2009) 312–317. https://doi.org/10.1016/j.jmbbm.2008.08.004.

[19] A.S. Mijailovic, B. Qing, D. Fortunato, K.J. Van Vliet, Characterizing viscoelastic mechanical properties of highly compliant polymers and biological tissues using impact indentation, Acta Biomater. 71 (2018) 388–397. https://doi.org/10.1016/j.actbio.2018.02.017.

[20] Z.I. Kalcioglu, R. Mahmoodian, Y. Hu, Z. Suo, K.J. Van Vliet, From macro- to microscale poroelastic characterization of polymeric hydrogels via indentation, Soft Matter. 8 (2012) 3393. https://doi.org/10.1039/c2sm06825g.

[21] K.A. Addae-Mensah, J.P. Wikswo, Measurement Techniques for Cellular Biomechanics *In Vitro*, Exp. Biol. Med. 233 (2008) 792–809. https://doi.org/10.3181/0710-MR-278.

[22] B.M. Baker, B. Trappmann, W.Y. Wang, M.S. Sakar, I.L. Kim, V.B. Shenoy, J. a. Burdick, C.S. Chen, Cell-mediated fibre recruitment drives extracellular matrix mechanosensing in engineered fibrillar microenvironments, Nat. Mater. 14 (2015) 1262–1268. https://doi.org/10.1038/nmat4444.

[23] M. Chyasnavichyus, S.L. Young, V. V Tsukruk, Recent advances in micromechanical characterization of polymer, biomaterial, and cell surfaces with atomic force microscopy, Jpn. J. Appl. Phys. 54 (2015). https://doi.org/10.7567/JJAP.54.08LA02.

[24] F. Liu, J.D. Mih, B.S. Shea, A.T. Kho, A.S. Sharif, A.M. Tager, D.J. Tschumperlin, Feedback amplification of fibrosis through matrix stiffening and COX-2 suppression, J. Cell Biol. 190 (2010) 693–706. https://doi.org/10.1083/jcb.201004082.

[25] A.K. Denisin, B.L. Pruitt, Tuning the Range of Polyacrylamide Gel Stiffness for Mechanobiology Applications, ACS Appl. Mater. Interfaces. 8 (2016) 21893–21902. https://doi.org/10.1021/acsami.5b09344.

[26] B.G. Bush, J.M. Shapiro, F.W. DelRio, R.F. Cook, M.L. Oyen, Mechanical measurements of heterogeneity and length scale effects in PEG-based hydrogels, Soft Matter. 11 (2015) 7191–7200. https://doi.org/10.1039/C5SM01210D.

[27] S.L. Vega, M.Y. Kwon, K.H. Song, C. Wang, R.L. Mauck, L. Han, J.A. Burdick, Combinatorial hydrogels with biochemical gradients for screening 3D cellular microenvironments, Nat. Commun. 9 (2018) 1–10. https://doi.org/10.1038/s41467-018-03021-5.

[28] M. Gnecchi, Mesenchymal Stem Cells: Methods and Protocols, 2016.

[29] D.S. Tzeranis, I. Panagiotopoulos, S. Gkouma, G. Kanakaris, N. Georgiou, N. Vaindirlis, G. Vasileiou, M. Neidlin, A. Gkousioudi, V. Spitas, G.A. Macheras, L.G. Alexopoulos, A device for high-throughput monitoring of degradation in soft tissue samples, J. Biomech. 74 (2018) 180–186. https://doi.org/10.1016/j.jbiomech.2018.04.040.

[30] C.A. Tweedie, D.G. Anderson, R. Langer, K.J. Van Vliet, Combinatorial material mechanics: High-throughput polymer synthesis and nanomechanical screening, Adv. Mater. 17 (2005) 2599–2604. https://doi.org/10.1002/adma.200501142.

[31] B. Mohanraj, C. Hou, G.R. Meloni, B.D. Cosgrove, G.R. Dodge, R.L. Mauck, A high throughput mechanical screening device for cartilage tissue engineering, J. Biomech. 47 (2014) 2130–2136. https://doi.org/10.1016/j.jbiomech.2013.10.043.

[32] B.A. Juliar, C. Strieder-Barboza, M. Karmakar, C.G. Flesher, N.A. Baker, O.A. Varban, C.N. Lumeng, A.J. Putnam, R.W. O'Rourke, Viscoelastic characterization of diabetic and non-diabetic human adipose tissue, Biorheology. 57 (2020) 15–26. https://doi.org/10.3233/BIR-190234.

[33] J. Wedgwood, A.J. Freemont, N. Tirelli, Rheological and turbidity study of fibrin hydrogels, Macromol. Symp. 334 (2013) 117–125. https://doi.org/10.1002/masy.201300111.

[34] V. Normand, D.L. Lootens, E. Amici, K.P. Plucknett, P. Aymard, New insight into agarose gel mechanical properties, Biomacromolecules. 1 (2000) 730–738. https://doi.org/10.1021/bm005583j.

[35] D.-H. Kim, P.K. Wong, J. Park, A. Levchenko, Y. Sun, Microengineered platforms for cell mechanobiology., Annu. Rev. Biomed. Eng. 11 (2009) 203–233. https://doi.org/10.1146/annurev-bioeng-061008-124915.

[36] D.B. Kolesky, R.L. Truby, A.S. Gladman, T.A. Busbee, K.A. Homan, J.A. Lewis, 3D bioprinting of vascularized, heterogeneous cell-laden tissue constructs, Adv. Mater. 26 (2014) 3124–3130. https://doi.org/10.1002/adma.201305506.

[37] H. Sun, P. Miao, Y. Tang, B. Wang, J. Qian, D. Wang, An elastography analytical method for the rapid detection of endotoxin, Analyst. 140 (2015) 4374–4378. https://doi.org/10.1039/c5an00734h.

[38] J.D. Dias, E.I. Haney, B.A. Mathew, C.G. Lopez-Espina, A.W. Orr, M.A. Popovsky, New-generation thromboelastography: Comprehensive evaluation of Citrated and heparinized blood sample storage effect on clot-forming variables, Arch. Pathol. Lab. Med. 141 (2017) 569–577. https://doi.org/10.5858/arpa.2016-0088-OA.

[39] K.S. Anseth, C.N. Bowman, L. Brannon-Peppas, Mechanical properties of hydrogels and their experimental determination, Biomaterials. 17 (1996) 1647–1657. https://doi.org/10.1016/0142-9612(96)87644-7.

[40] Q. Chen, S.I. Ringleb, T. Hulshizer, K.N. An, Identification of the testing parameters in high frequency dynamic shear measurement on agarose gels, J. Biomech. 38 (2005) 959–963. https://doi.org/10.1016/j.jbiomech.2004.05.015.

[41] C. Ceccaldi, S. Strandman, E. Hui, E. Montagnon, C. Schmitt, A. Hadj Henni, S. Lerouge, Validation and application of a nondestructive and contactless method for rheological evaluation of biomaterials, J. Biomed. Mater. Res. - Part B Appl. Biomater. 105 (2017) 2565–2573. https://doi.org/10.1002/jbm.b.33797.

[42] E.C. Hobson, W. Li, B.A. Juliar, A.J. Putnam, J.P. Stegemann, C.X. Deng, Resonant acoustic rheometry for non-contact characterization of viscoelastic biomaterials, Biomaterials. 269 (2021) 120676. https://doi.org/10.1016/j.biomaterials.2021.120676.

[43] V. Adibnia, R.J. Hill, Universal aspects of hydrogel gelation kinetics, percolation and viscoelasticity from PA-hydrogel rheology, J. Rheol. (N. Y. N. Y). 60 (2016) 541–548. https://doi.org/10.1122/1.4948428.

[44] E. Scărlătescu, M.D. Lancé, N.J. White, D.R. Tomescu, Thromboelastometric prediction of mortality using the kinetics of clot growth in critically ill septic patients, Blood Coagul. Fibrinolysis. 29 (2018) 533–539. https://doi.org/10.1097/MBC.0000000000000757.

[45] V.G. Nielsen, R.T. Lyerly, W.Q. Gurley, The effect of dilution on plasma coagulation kinetics determined by thrombelastography is dependent on antithrombin activity and mode of activation, Anesth. Analg. 99 (2004) 1587–1592. https://doi.org/10.1213/01.ANE.0000136843.58799.AB.

[46] S.L. Rowe, J.P. Stegemann, Microstructure and mechanics of collagen-fibrin matrices polymerized using ancrod snake venom enzyme, J. Biomech. Eng. 131 (2009) 1–9. https://doi.org/10.1115/1.3128673.

[47] M.Z. Kiss, T. Varghese, T.J. Hall, Viscoelastic characterization of in vitro canine tissue, Phys. Med. Biol. 49 (2004) 4207–4218. https://doi.org/10.1088/0031-9155/49/18/002.

[48] B.A. Juliar, M.T. Keating, Y.P. Kong, E.L. Botvinick, A.J. Putnam, Sprouting angiogenesis induces significant mechanical heterogeneities and ECM stiffening across length scales in fibrin hydrogels, Biomaterials. 162 (2018) 99–108. https://doi.org/10.1016/j.biomaterials.2018.02.012.

[49] S.B. Ross-Murphy, Structure and rheology of gelatin gels, Imaging Sci. J. 45 (1997) 205–209. https://doi.org/10.1080/13682199.1997.11736407.

[50] M.F. Butler, Y.F. Ng, P.D.A. Pudney, Mechanism and kinetics of the crosslinking reaction between biopolymers containing primary amine groups and genipin, J. Polym. Sci. Part A Polym. Chem. 41 (2003) 3941–3953. https://doi.org/10.1002/pola.10960.

[51] B.C.– E.S. Group, Viscoelastic Characterization of Agarose Gel Scaffolds [White Paper], 2014. http://www.tainstruments.com/pdf/literature/EF018.pdf.

[52] J.A. Beamish, B.A. Juliar, D.S. Cleveland, M.E. Busch, L. Nimmagadda, A.J. Putnam, Deciphering the relative roles of matrix metalloproteinase- and plasmin-mediated matrix degradation during capillary morphogenesis using engineered hydrogels, J. Biomed. Mater. Res. - Part B Appl. Biomater. (2019) 1–10. https://doi.org/10.1002/jbm.b.34341.

[53] M.D. Hunckler, J.D. Medina, M.M. Coronel, J.D. Weaver, C.L. Stabler, A.J. García, Linkage Groups within Thiol–Ene Photoclickable PEG Hydrogels Control In Vivo Stability, Adv. Healthc. Mater. 8 (2019) 1–7. https://doi.org/10.1002/adhm.201900371.

[54] J. Hu, S. Jafari, Y. Han, A.J. Grodzinsky, S. Cai, M. Guo, Size- and speed-dependent mechanical behavior in living mammalian cytoplasm, Proc. Natl. Acad. Sci. 114 (2017) 9529–9534. https://doi.org/10.1073/pnas.1702488114.

[55] Z. Fan, X. Xue, R. Perera, S. Nasr Esfahani, A.A. Exner, J. Fu, C.X. Deng, Acoustic Actuation of Integrin-Bound Microbubbles for Mechanical Phenotyping during Differentiation and Morphogenesis of Human Embryonic Stem Cells, Small. 1803137 (2018) 1–8. https://doi.org/10.1002/smll.201803137.

[56] D. Chen, Y. Sun, M.S.R. Gudur, Y.S. Hsiao, Z. Wu, J. Fu, C.X. Deng, Two-bubble acoustic tweezing cytometry for biomechanical probing and stimulation of cells, Biophys. J. 108 (2015) 32–42. https://doi.org/10.1016/j.bpj.2014.11.050.

[67] Z. Hajjarian, H.T. Nia, S. Ahn, A.J. Grodzinsky, R.K. Jain, S.K. Nadkarni, Laser Speckle Rheology for evaluating the viscoelastic properties of hydrogel scaffolds, Sci. Rep. 6 (2016) 1–12. https://doi.org/10.1038/srep37949.

[58] R.H. Ewoldt, M.T. Johnston, L.M. Caretta, Experimental Challenges of Shear Rheology: How to Avoid Bad Data, in: S.E. Spagnolie (Ed.), Complex Fluids Biol. Syst. Exp. Theory, Comput., Springer New York, New York, NY, 2015: pp. 207–241. https://doi.org/10.1007/978-1-4939-2065-5_6.

[59] S. Zhao, M. Arnold, R.L. Abel, J.P. Cobb, S. Ma, U. Hansen, O. Boughton, Standardizing Compression Testing for Measuring the Stiffness of Human Bone, Bone Jt. Res. 7 (2018) 524–538. https://doi.org/10.1302/2046-3758.78.BJR-2018-0025.R1.

[60] D. Dalecki, K.P. Mercado, D.C. Hocking, Quantitative Ultrasound for Nondestructive Characterization of Engineered Tissues and Biomaterials, Ann. Biomed. Eng. 44 (2016) 636–648. https://doi.org/10.1007/s10439-015-1515-0.

[61] C.X. Deng, X. Hong, J.P. Stegemann, Ultrasound imaging techniques for spatiotemporal characterization of composition, microstructure, and mechanical properties in tissue engineering, Tissue Eng. Part B Rev. 183 (2016) ten.TEB.2015.0453. https://doi.org/10.1089/ten.TEB.2015.0453.

[62] S. Dasgupta, E.J. Feleppa, Empirical validation of the theoretical frameworks underlying ultrasound scattering in tissue, Proc. - IEEE Ultrason. Symp. (2007) 236–239. https://doi.org/10.1109/ULTSYM.2007.70.

[63] F.E. Borgnis, Acoustic radiation pressure of plane compressional waves, Rev. Mod. Phys. 25 (1953) 653–664. https://doi.org/10.1103/RevModPhys.25.653.

[64] F.L. Lizzi, E.J. Feleppa, S. Kaisar Alam, C.X. Deng, Ultrasonic spectrum analysis for tissue evaluation, Pattern Recognit. Lett. 24 (2003) 637–658. https://doi.org/10.1016/S0167-8655(02)00172-1.

[65] F.W. Mauldin, F. Viola, W.F. Walker, Complex principal components for robust motion estimation, IEEE Trans. Ultrason. Ferroelectr. Freq. Control. 57 (2010) 2437–2449.

https://doi.org/10.1109/TUFFC.2010.1710.

[66] J. Luo, E. Konofagou, A fast normalized cross-correlation calculation method for motion estimation, IEEE Trans. Ultrason. Ferroelectr. Freq. Control. 57 (2010) 1347–1357. https://doi.org/10.1109/TUFFC.2010.1554.

[67] J.E. Brandenburg, S.F. Eby, P. Song, H. Zhao, J.S. Brault, S. Chen, K.N. An, Ultrasound elastography: The new frontier in direct measurement of muscle stiffness, Arch. Phys. Med. Rehabil. 95 (2014) 2207–2219. https://doi.org/10.1016/j.apmr.2014.07.007.

[68] B. Peng, Y. Wang, W. Yang, T. Varghese, J. Jiang, Relative Elastic Modulus Imaging Using Sector Ultrasound Data for Abdominal Applications: An Evaluation of Strategies and Feasibility, IEEE Trans. Ultrason. Ferroelectr. Freq. Control. 63 (2016) 1432–1440. https://doi.org/10.1109/TUFFC.2016.2589270.

[69] M. Theodorou, J. Fromageau, J.C. Bamber, A. Phantom, Quantitative poroelastic property imaging combining shear wave and strain elastography, 2015 IEEE Int. Ultrason. Symp. Proc. (2015) 3–6.

[70] K. Nightingale, M.S. Soo, R. Nightingale, G. Trahey, Acoustic radiation force impulse imaging: in vivo demonstration of clinical feasibility, Ultrasound Med. Biol. 28 (2016) 227–235. https://doi.org/10.1016/S0301-5629(01)00499-9.

[71] C. Bruno, S. Minniti, A. Bucci, R. Pozzi Mucelli, ARFI: from basic principles to clinical applications in diffuse chronic disease—a review, Insights Imaging. 7 (2016) 735–746. https://doi.org/10.1007/s13244-016-0514-5.

[72] M.R. Selzo, C.M. Gallippi, Viscoelastic response (VisR) imaging for assessment of viscoelasticity in voigt materials, IEEE Trans. Ultrason. Ferroelectr. Freq. Control. 60 (2013) 2488–2500. https://doi.org/10.1109/TUFFC.2013.2848.

[73] F.W. Mauldin, M.A. Haider, E.G. Loboa, R.H. Behler, L.E. Euliss, T.W. Pfeiler, C.M. Gallippi, Monitored steady-state excitation and recovery (MSSER) radiation force imaging using viscoelastic models, IEEE Trans. Ultrason. Ferroelectr. Freq. Control. 55 (2008) 1597–1610. https://doi.org/10.1109/TUFFC.2008.836.

[74] C.A. Carrascal, S. Chen, M.W. Urban, J.F. Greenleaf, Acoustic Radiation Force-Induced Creep-Recovery (ARFICR): A Noninvasive Method to Characterize Tissue Viscoelasticity, IEEE Trans. Ultrason. Ferroelectr. Freq. Control. 65 (2018) 3–13. https://doi.org/10.1109/TUFFC.2017.2768184.

[75] M.R. Scola, C.M. Gallippi, Multi-Push (MP) ARF assessment of viscoelastic properties in a tissue mimicking phantom: Effect of time separation, IEEE Int. Ultrason. Symp. IUS. (2011). https://doi.org/10.1109/ULTSYM.2011.0161.

[76] Y. Liu, B.A. Herman, J.E. Soneson, G.R. Harris, Thermal safety simulations of transient temperature rise during acoustic radiation force-based ultrasound elastography, Ultrasound Med. Biol. 40 (2014) 1001–1014. https://doi.org/10.1016/j.ultrasmedbio.2013.11.015.

[77] M.L. Palmeri, K.R. Nightingale, On the thermal effects associated with radiation force imaging of soft tissue, IEEE Trans. Ultrason. Ferroelectr. Freq. Control. 51 (2004) 551–565. https://doi.org/10.1109/TUFFC.2004.1320828.

[78] M.L. Palmeri, K.R. Nightingale, Thermal effects associated with acoustic radiation force impulse imaging, Proc. 2003 IEEE Ultrason. Symp. 00 (2003) 232–237. https://doi.org/10.1109/ULTSYM.2003.1293396.

[79] M.L. Palmeri, M.H. Wang, N.C. Rouze, M.F. Abdelmalek, C.D. Guy, B. Moser, A.M. Diehl, K.R. Nightingale, Noninvasive evaluation of hepatic fibrosis using acoustic radiation force-based shear stiffness in patients with nonalcoholic fatty liver disease, J. Hepatol. 55 (2011) 666–672. https://doi.org/10.1016/j.jhep.2010.12.019.

[80] M. Teke, F. Teke, B. Alan, A. Türkoğlu, C. Hamidi, C. Göya, S. Hattapoğlu, M. Gumus, Differential diagnosis of idiopathic granulomatous mastitis and breast cancer using acoustic radiation force impulse imaging, J. Med. Ultrason. 44 (2017) 109–115. https://doi.org/10.1007/s10396-016-0749-2.

[81] Y. Fujita, M. Kitago, T. Abe, O. Itano, M. Shinoda, Y. Abe, H. Yagi, T. Hibi, M. Ishii, Y. Nakano, K. Okuma, M. Hashimoto, A. Takeuchi, Y. Masugi, M. Jinzaki, M. Sakamoto, Y. Kitagawa, Evaluation of pancreatic fibrosis with acoustic radiation force impulse imaging and automated quantification of pancreatic tissue components, Pancreas. 47 (2018) 1277–1282. https://doi.org/10.1097/MPA.0000000000001179.

[82] A.P. Sarvazyan, O. V. Rudenko, S.D. Swanson, J.B. Fowlkes, S.Y. Emelianov, Shear wave elasticity imaging: A new ultrasonic technology of medical diagnostics, Ultrasound Med. Biol. 24 (1998) 1419–1435. https://doi.org/10.1016/S0301-5629(98)00110-0.

[83] P.-L. Kuo, C.-C. Charng, P.-C. Wu, P.-C. Li, Shear-wave elasticity measurements of three-dimensional cell cultures for mechanobiology, J. Cell Sci. 130 (2017) 292–302. https://doi.org/10.1242/jcs.186320.

[84] M. Palmeri, B. Qiang, S. Chen, M. Urban, Guidelines for Finite Element Modeling of Acoustic Radiation Force-Induced Shear Wave Propagation in Tissue-Mimicking Media., IEEE Trans. Ultrason. Ferroelectr. Freq. Control. 64 (2016) 1–1. https://doi.org/10.1109/TUFFC.2016.2641299.

[85] C. Schmitt, A. Hadj Henni, G. Cloutier, Characterization of blood clot viscoelasticity by dynamic ultrasound elastography and modeling of the rheological behavior, J. Biomech. 44 (2011) 622–629. https://doi.org/10.1016/j.jbiomech.2010.11.015.

[86] K.P. Mercado, J. Langdon, M. Helguera, S.A. McAleavey, D.C. Hocking, D. Dalecki, Scholte wave generation during single tracking location shear wave elasticity imaging of engineered tissues, J. Acoust. Soc. Am. 138 (2015) EL138–EL144. https://doi.org/10.1121/1.4927633.

[87] E.E.W. Van Houten, Parameter identification in a generalized time-harmonic rayleigh damping model for elastography, PLoS One. 9 (2014) 1–9. https://doi.org/10.1371/journal.pone.0093080.

[88] S. Kazemirad, S. Bernard, S. Hybois, A. Tang, G. Cloutier, Ultrasound Shear Wave Viscoelastography: Model-Independent Quantification of the Complex Shear Modulus, IEEE Trans. Ultrason. Ferroelectr. Freq. Control. 63 (2016) 1399–1408. https://doi.org/10.1109/TUFFC.2016.2583785.

[89] N.C. Rouze, M.L. Palmeri, K.R. Nightingale, An analytic, Fourier domain description of shear wave propagation in a viscoelastic medium using asymmetric Gaussian sources., J. Acoust. Soc. Am. 138 (2015) 1012–22. https://doi.org/10.1121/1.4927492.

[90] F.S. Corey, W.F. Walker, Sonic Estimation of Elasticity via Resonance: A New Method of Assessing Hemostasis, Ann. Biomed. Eng. 44 (2016) 1405–1424. https://doi.org/10.1007/s10439-015-1460-y.

[91] R.I. Litvinov, J.W. Weisel, Fibrin mechanical properties and their structural origins, Matrix Biol. 60–61 (2017) 110–123. https://doi.org/10.1016/j.matbio.2016.08.003.

[92] J.R. Harris, D.J.S. Hulmes, Fibrous Proteins: Structures and Mechanisms, 2017.

[93] F. Ferri, M. Greco, G. Arcovito, F.A. Bassi, M. De Spirito, E. Paganini, M. Rocco, Growth kinetics and structure of fibrin gels, Phys. Rev. E - Stat. Nonlinear, Soft Matter Phys. 63 (2001) 0314011–03140117. https://doi.org/10.1103/physreve.63.031401.

[94] L. Lorand, Crosslinks in blood: transglutaminase and beyond, FASEB J. 21 (2007) 1627–1632. https://doi.org/10.1096/fj.07-0602ufm.

[95] S. Naahidi, M. Jafari, M. Logan, Y. Wang, Y. Yuan, H. Bae, B. Dixon, P. Chen, Biocompatibility of hydrogel-based scaffolds for tissue engineering applications, Biotechnol. Adv. 35 (2017) 530–544. https://doi.org/10.1016/j.biotechadv.2017.05.006.

[96] P.A. Janmey, J.P. Winer, J.W. Weisel, Fibrin gels and their clinical and bioengineering applications, J. R. Soc. Interface. 6 (2009) 1–10. https://doi.org/10.1098/rsif.2008.0327.

[97] A.Y. Rioja, R. Tiruvannamalai Annamalai, S. Paris, A.J. Putnam, J.P. Stegemann, Endothelial sprouting and network formation in collagen- and fibrin-based modular microbeads, Acta Biomater. 29 (2016) 33–41. https://doi.org/10.1016/j.actbio.2015.10.022.

[98] J. Alipal, N.A.S. Mohd Pu'ad, T.C. Lee, N.H.M. Nayan, N. Sahari, H. Basri, M.I. Idris, H.Z. Abdullah, A review of gelatin: Properties, sources, process, applications, and commercialisation, Mater. Today Proc. 42 (2019) 240–250. https://doi.org/10.1016/j.matpr.2020.12.922.

[99] S.M. Lien, W. Te Li, T.J. Huang, Genipin-crosslinked gelatin scaffolds for articular cartilage tissue engineering with a novel crosslinking method, Mater. Sci. Eng. C. 28 (2008) 36–43. https://doi.org/10.1016/j.msec.2006.12.015.

[100] M. Zhou, B.H. Lee, Y.J. Tan, L.P. Tan, Microbial transglutaminase induced controlled crosslinking of gelatin methacryloyl to tailor rheological properties for 3D printing, Biofabrication. 11 (2019). https://doi.org/10.1088/1758-5090/ab063f.

[101] P.A. Turner, J.S. Thiele, J.P. Stegemann, Growth factor sequestration and enzyme-mediated release from genipin-crosslinked gelatin microspheres, J. Biomater. Sci. Polym. Ed. 28 (2017) 1826–1846. https://doi.org/10.1080/09205063.2017.1354672.

[102] M.E. Dawson, A Wealth of Options: Choosing an LAL Test Method, LAL Updat. 13 (1995) 1–3.

[103] X. Ding, W. Su, X. Ding, Methods of Endotoxin Detection, J. Lab. Autom. 20 (2015) 354–

364. https://doi.org/10.1177/2211068215572136.

[104] T. Liu, W. Zhang, L. Zhou, Z. Guo, Y. Tang, P. Miao, A quartz crystal microbalance sensor for endotoxin assay by monitoring limulus amebocyte lysate protease reaction, Anal. Chim. Acta. 961 (2017) 106–111. https://doi.org/10.1016/j.aca.2017.01.014.

[105] K. Martin, A.D. Ma, N.S. Key, Molecular basis of hemostatic and thrombotic diseases, Second Edition, Elsevier Inc., 2018. https://doi.org/10.1016/B978-0-12-802761-5.00015-8.

[106] A.Y. Rioja, E.L.H. Daley, J.C. Habif, A.J. Putnam, J.P. Stegemann, Distributed vasculogenesis from modular agarose-hydroxyapatite-fibrinogen microbeads, Acta Biomater. 55 (2017) 144–152. https://doi.org/10.1016/j.actbio.2017.03.050.

[107] N. Pernodet, M. Maaloum, B. Tinland, Pore size of agarose gels by atomic force microscopy, Electrophoresis. 18 (1997) 55–58. https://doi.org/10.1002/elps.1150180111.

[108] S.M. Lien, L.Y. Ko, T.J. Huang, Effect of pore size on ECM secretion and cell growth in gelatin scaffold for articular cartilage tissue engineering, Acta Biomater. 5 (2009) 670–679. https://doi.org/10.1016/j.actbio.2008.09.020.

[109] C.L. Chiu, V. Hecht, H. Duong, B. Wu, B. Tawil, Permeability of three-dimensional fibrin constructs corresponds to fibrinogen and thrombin concentrations, Biores. Open Access. 1 (2012) 34–40. https://doi.org/10.1089/biores.2012.0211.

[110] J. Zhu, Bioactive modification of poly(ethylene glycol) hydrogels for tissue engineering, Biomaterials. 31 (2010) 4639–4656. https://doi.org/10.1016/j.biomaterials.2010.02.044.

[111] O. Chaudhuri, L. Gu, D. Klumpers, M. Darnell, S.A. Bencherif, J.C. Weaver, N. Huebsch, H.P. Lee, E. Lippens, G.N. Duda, D.J. Mooney, Hydrogels with tunable stress relaxation regulate stem cell fate and activity, Nat. Mater. 15 (2016) 326–334. https://doi.org/10.1038/nmat4489.

[112] M.S. Weiss, B.P. Bernabe, A. Shikanov, D.A. Bluver, M.D. Mui, S. Shin, L.J. Broadbelt, L.D. Shea, The impact of adhesion peptides within hydrogels on the phenotype and signaling of normal and cancerous mammary epithelial cells, Biomaterials. 33 (2012) 3548–3559. https://doi.org/10.1016/j.biomaterials.2012.01.055.

[113] M.P. Lutolf, J. a Hubbell, Synthetic biomaterials as instructive extracellular microenvironments for morphogenesis in tissue engineering., Nat. Biotechnol. 23 (2005) 47–55. https://doi.org/10.1038/nbt1055.

[114] C. Mandrycky, Z. Wang, K. Kim, D.H. Kim, 3D bioprinting for engineering complex tissues, Biotechnol. Adv. 34 (2016) 422–434. https://doi.org/10.1016/j.biotechadv.2015.12.011.

[115] F. Monroy, Surface hydrodynamics of viscoelastic fluids and soft solids: Surfing bulk rheology on capillary and Rayleigh waves, Adv. Colloid Interface Sci. 247 (2017) 4–22. https://doi.org/10.1016/j.cis.2017.07.006.

[116] P.-K. Choi, E. Jyounouti, K. Yuuki, Y. Onodera, Experimental observation of pseudocapillary and Rayleigh modes on soft gels, J. Acoust. Soc. Am. 106 (2002) 1591–1593. https://doi.org/10.1121/1.427156.

[117] S.A. Elrod, B. Hadimioglu, B.T. Khuri-Yakub, E.G. Rawson, E. Richley, C.F. Quate, N.N. Mansour, T.S. Lundgren, Nozzleless droplet formation with focused acoustic beams, J. Appl. Phys. 65 (1989) 3441–3447. https://doi.org/10.1063/1.342663.

[118] M. Forbush, H. Chow, J. Chiao, A. Rose, Noninvasive Fluid Property Measurements Using Acoustic Methods, Clin. Lab. Med. 27 (2007) 61–73. https://doi.org/10.1016/j.cll.2006.12.002.

[119] R.O. Williams, J. Chiao, H. Chow, M. Forbush, A. Rose, ACOUSTIC METHOD FOR DETERMINING THE VISCOSITY AND/OR SURFACE TENSION OF A LIQUID, 2007.

[120] B.H. Cao, M.W. Kim, H. Schaffer, H.Z. Cummins, Surface modes on polymer solutions by surface light-scattering techniques, J. Chem. Phys. 95 (1991) 9375. https://doi.org/10.1063/1.464543.

[121] H. Takahashi, P.-K. Choi, Sol – Gel Transition in Gelatin Observed with Surface Waves, Jpn. J. Appl. Phys. 35 (1996) 2939–2943.

[122] Y. Onodera, P.-K. Choi, Surface-wave modes on soft gels, J. Acoust. Soc. Am. 104 (1998) 3358–3363. https://doi.org/10.1121/1.423919.

[123] J.L. Harden, H. Pleiner, P.A. Pincus, Hydrodynamic surface modes on concentrated polymer solutions and gels, J. Chem. Phys. 94 (1991) 5208–5221. https://doi.org/10.1063/1.460525.

[124] H. Chen, H. Shi, T. Varghese, Improvement of elastographic displacement estimation using a two-step cross-correlation method, Ultrasound Med. Biol. 33 (2007) 48–56. https://doi.org/10.1016/j.ultrasmedbio.2006.07.022.

Chapter 2 Development and Validation of Resonant Acoustic Rheometry (RAR)

2.1 Introduction

The mechanical properties of the cellular microenvironment are an important regulator of cellular phenotype [1,2]. To this end, hydrogels have been used extensively in the field of tissue engineering as a synthetic extracellular matrix, providing a valuable biomaterial platform to recapitulate the structure and function of a variety of biological tissues. These biomaterials consist primarily of water-infused networks of hydrophilic polymer chains and are typically soft and viscoelastic. Hydrogels can be made from a wide variety of natural and synthetic polymers and can be modified to exhibit specific biochemical cues for regulating cellular phenotype [3]. Their mechanical properties can vary widely despite the high volume-percentage of water common to all hydrogel materials. Both the elastic and viscous components of the extracellular matrix have been implicated as important effectors in controlling cell function [4,5]. Therefore, the capability to measure and analyze the viscoelastic properties of biomaterials is important in tissue engineering applications.

Compared to solid polymers or metals, mechanical testing of hydrogels can be particularly challenging due to their relatively low elastic modulus, viscoelastic nature, and biphasic structure [6]. Common material testing approaches include tension, compression, indentation, and shear-based approaches [6,7]. Each of these methods operates by applying a defined deformation or force to a sample and then measuring the material response. The viscoelastic behavior can be assessed from time-dependent material responses, such as creep and stress relaxation [8]. However, the deformation required by these techniques is generally achieved by physical contact, which can result in contamination and damage, thereby limiting these approaches to a single end-point measurement for each sample [9]. In addition, the viscoelastic properties of hydrogels are rarely static, as they undergo continuous change due to swelling, enzymatic degradation or crosslinking, and in some cases cell-mediated remodeling [10,11]. Therefore, there is a need for methods capable of longitudinal tracking of the mechanical properties of these materials as they change over various time scales.

Ultrasound techniques that use acoustic radiation force (ARF) to induce deformation to a sample have been exploited as a non-invasive strategy to evaluate both the static [12–14] and dynamic [15–18] mechanical properties of biomaterials and tissues. These approaches can map the spatial mechanical heterogeneity in a tissue region based on the differential deformation within a specific volume. However, they generally do not provide quantification of the intrinsic material properties since this requires knowledge of the ultrasonic field and the acoustic attenuation of the material being tested. Shear wave-based methods [19–21] are independent of the spatial profile of the ultrasonic field but require relatively large sample volumes unless resonant shear waves are examined [22–24]. Importantly, ARF-based elastography techniques require 1) sufficient acoustic absorption in a material to generate the ARF required to induce material deformation and 2) the presence of scattering elements within the material (e.g. cells, microparticles, bubbles), to generate detectable echoes for tracking of deformation using ultrasound imaging. These requirements prevent the use of these techniques in soft materials such as the hydrogel constructs commonly used in tissue engineering studies, which are often small in size, with low acoustic absorption coefficients and weak acoustic scattering.

To overcome these limitations, we have developed a new non-contact technique, resonant acoustic rheometry (RAR), to quantitatively characterize the intrinsic mechanical properties of soft hydrogel materials. RAR uses a focused ultrasound pulse to generate a controlled perturbation at the surface of a liquid or hydrogel sample and detects the ensuing resonant modes of surface waves using pulse-echo ultrasound imaging. Measurement can be performed in a standard cell culture microwell plate, and the process can be automated for high-throughput analysis. RAR capitalizes on the specific resonant modes of a hydrogel sample to extract viscoelastic material properties [25,26]. Importantly, the air-sample interface is a near-perfect reflector of ultrasound, and therefore the generation and detection of surface movements are highly efficient and do not rely on the absorptive or scattering behaviors of the bulk material [27]. In the present study, we have explored the use of RAR for characterizing the mechanical behaviors of hydrogel biomaterials commonly used in tissue engineering. In particular, the technique was used to noninvasively measure the viscoelastic properties of fibrin, gelatin, and agarose hydrogels at a variety of polymer concentrations. The results were validated using finite element analysis, as well as through comparison with conventional shear rheometry. In addition, the change in mechanical properties over time was measured in fibrin hydrogels during the process of thrombin-catalyzed gelation. Taken together, these studies demonstrate that RAR has the potential to be a valuable new tool in the characterization of soft biomaterials used in a variety of applications.

2.2 Materials and Methods

2.2.1 Sample perturbation using ultrasound

Figure 2.1 shows the experimental setup used for RAR. A custom ultrasound transducer with two collinearly aligned elements was submerged in a temperature-controlled water tank and directed upwards at the center of a well in a microplate to excite and detect movement at the surface of a sample (Fig. 2.1A). The bottom of the microplate was affixed just below the water surface for efficient acoustic coupling. The transducer was attached to a 3D motion control platform (Velmex), allowing for automated positioning for initial alignment and testing of

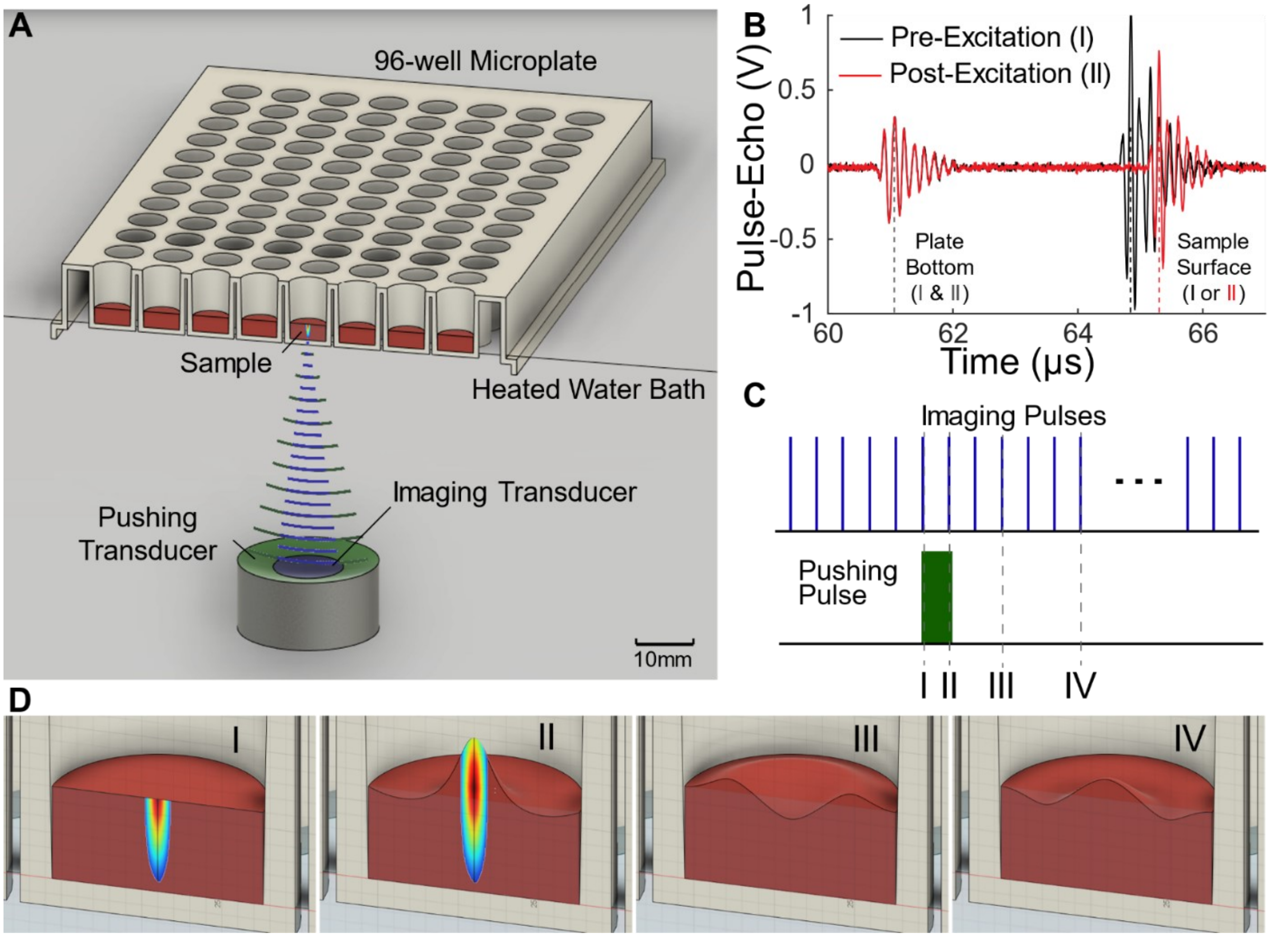

Figure 2.1: (A) Schematic diagram of the RAR experimental system with a focused ultrasound transducer aligned beneath a microplate for generating measurements through the sealed plate bottom. (B) A-line generated from pulse-echo at time points just prior to (time I) and following (time II) ARF excitation. (C) Schematic of coordination of imaging and excitation pulse sequences. (D) Exaggerated illustrations showing surface deformations at selected time points (I, II, III, and IV) during a RAR experiment. ARF intensity field is depicted at times during excitation (I and II).

materials in multiple wells in a single experiment (Fig. 2.2A shows an image of transducer alignment with a sample in a 96-well plate). The transducers were aligned with the center of the circular sample surface in order to minimize the generation of asymmetric modes of surface oscillation and to maximize the measured displacement by focusing at the central antinode. The outer annular element of the ultrasound transducer had a center frequency of 1.5 MHz and the inner circular element had a center frequency of 7 MHz and a focal distance of 48 mm. The lower frequency of the pushing transducer minimized attenuation and enabled high power transmission through the microplate and sample, while the higher imaging frequency allowed for higher axial resolution. The 1.5 MHz annular element was driven by a waveform generator (33220A; Agilent) and a power amplifier (75A250; Amplifier Research) and was used to generate an exciting ultrasound pulse to induce surface deformation through application of a controlled ARF.

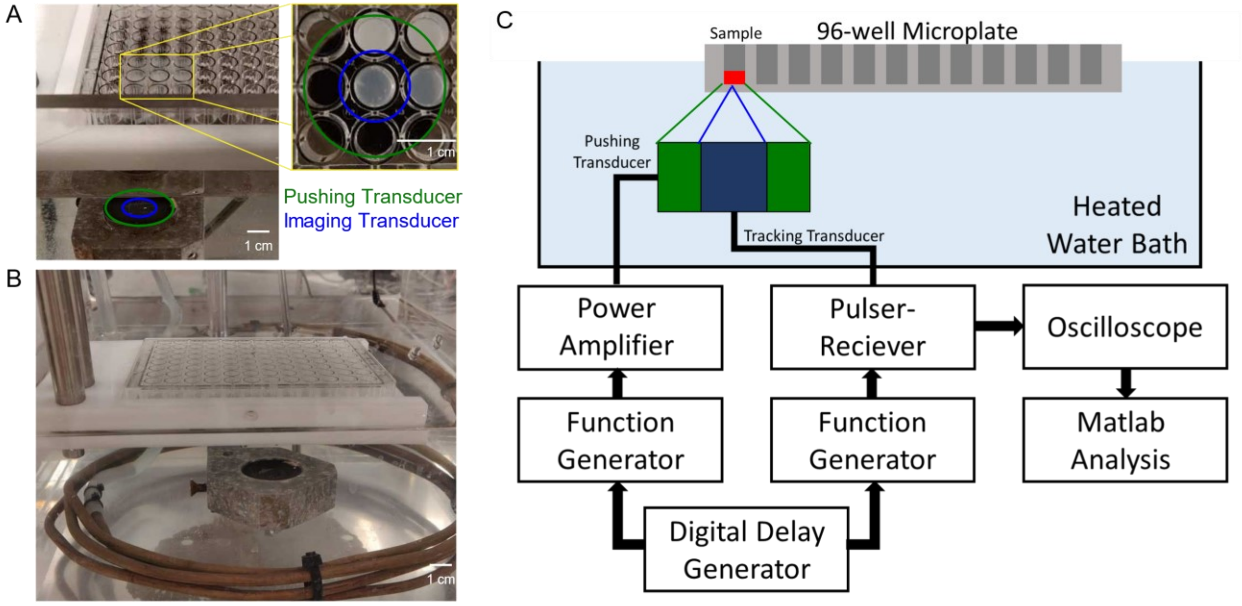

Figure 2.2: A) Image of RAR setup, showing a two-element ultrasound transducer submerged in a heated water bath, beneath a 96-well microplate. The inner (imaging) transducer is outlined in blue and outer (excitation) transducer is outlined in green. Inset shows the centered alignment of transducers directly beneath a microplate well containing a hydrogel sample. B) Expanded image of RAR setup showing entire 96-well plate and copper heating coils. C) Block diagram of RAR experimental system, showing equipment used to generate and record ultrasound signals for each transducer element.

2.2.2 Ultrasound pulse-echo detection of surface movement

The inner imaging transducer (-3 dB beam width ~ 0.5 mm) was used in pulse-echo mode to identify the bottom and top surfaces of the samples. This was facilitated by the strong reflections from the air-sample and sample-microplate interfaces (Fig. 2.1B). The microplates used in this study are polystyrene (acoustic impedance (Z) of 2.49x10^5 g/cm^2-sec, density of 1.06 g/cm^3, and sound speed of 2350 m/s) with an acoustic intensity reflection coefficient of approximately 0.065 at an interface with water (Z of 1.48x10^5 g/cm^2-sec, density of 1.0 g/cm^3, and sound speed of 1480 m/s). While sufficient for the detection of the plate bottom, this reflection coefficient is much less than the air-liquid surface, which is a nearly perfect reflector (reflection coefficient of almost 1) due to the huge impedance difference between water and air. The transducer elements are focused on the sample surface using an automated protocol: measuring the delay of the echo from the air-sample interface, calculating the position of the sample surface, and moving the transducer to the correct distance. Surface displacement was determined from the temporal shifts of the second peak relative to the pre-excitation signal using a normalized cross-correlation algorithm with a ten-wavelength window. The sample was stationary at the bottom surface and therefore the relative change of the sample surface location was used to represent the surface displacement, without systemic electrical or mechanical biases. The imaging element was driven by a pulser/receiver (5900PR; Olympus) and A-line backscattered RF signals are received and digitized at a sample rate of 250 MSamples/s using a digital oscilloscope (54830B; Agilent). A pulse generator (Model 565; BNC) was used to synchronize the excitation and tracking ultrasound pulses from the two transducer elements (Fig. 2.1C). All instruments were controlled using a custom MATLAB (MathWorks) script, allowing for high-throughput automated testing. Single time point RAR involved application of one excitation ultrasound pulse to induce surface perturbation followed by a series of rapid pulse-echo interrogations (pulse repetition frequency 4000 Hz, or a 250 μs time interval) to detect the kinetics of surface perturbation. For longitudinal monitoring over time, RAR was applied at regular intervals to track changes in mechanical properties as the materials gelled. This mode of analysis was possible because the time scale of material changes was much longer than that of the surface oscillation.

2.2.3 Hydrogel material preparation

A 10.0 mg/ml (clottable) fibrinogen stock solution was prepared by dissolving lyophilized bovine fibrinogen (F8630, Sigma) in phosphate buffered saline (PBS; Gibco) at 37°C. The fibrinogen solution was filtered using a 0.2 um PVDF syringe filter and diluted with PBS to generate 2.0, 4.0, 6.0, and 8.0 mg/ml concentrations. A 50 Unit/ml bovine thrombin (T6634; Sigma) stock solution was prepared in a sterile-filtered solution of 0.1 %w/v bovine serum albumin (Sigma) in DI water. A 10.0 mg/ml agarose stock solution was prepared by dissolving agarose powder (Type 1-A; Sigma) into PBS with continuous stirring heating and stirring. The solution was transferred to a 50 °C water bath and was diluted with pre-heated PBS to generate additional solutions with 1.0, 2.0, 4.0, 6.0, and 8.0 mg/ml agarose concentrations. A 100 mg/ml gelatin stock solution was prepared by dissolving bovine gelatin powder (200 Bloom, 30 mesh; Gelatin Innovations) into PBS with continuous stirring heating and stirring. The 100 mg/ml gelatin solution was diluted with pre-heated PBS to generate solutions with 10, 20, 40, 60, and 80 mg/ml gelatin concentrations.

2.2.4 Hydrogel preparation for end-point characterization of viscoelastic properties

Fibrin gels were prepared for end-point measurement by combining the prepared fibrinogen solutions with 50 U/ml thrombin at a 500:1 ratio and pipetting to mix. Immediately after mixing, 100 μl volumes were pipetted into 96-well untreated polystyrene microplates with a

190 µm polystyrene film bottom (µClear, Greiner) for RAR and 500 µl volumes were pipetted into 24-well untreated microplates (Falcon) for shear rheometry measurements. Adhesive plate seals were applied to minimize sample dehydration and samples were allowed to gel at 37 °C for 24 hours and then 4 °C for 24 hours prior to testing. Agarose and gelatin samples were prepared in a similar fashion by direct pipetting into the appropriate sample holders for RAR and shear rheometry and were then sealed and allowed to gel at 4 °C for 48 hours prior to testing.

2.2.5 Hydrogel preparation for dynamic measurements of mechanical properties

To demonstrate measurement of changes in mechanical properties of samples over time, fibrinogen solutions were pre-heated to 37 °C and combined with 50 U/ml thrombin at a 500:1, 250:1, or 125:1 ratio to produce solutions with thrombin concentrations of 0.1, 0.2 and 0.4 U/ml, respectively. After mixing, 100 µl volumes were immediately pipetted into 96-well microplates (µClear, Greiner) that had been coated with a fluorosiloxane (Syl-Off; Dow). Adhesive plate seals were applied to minimize sample dehydration and testing was initiated exactly 60 seconds following the addition of thrombin. A custom MATLAB script was utilized to automatically test each sample every 30 seconds for a total 30 minute tracking period.

2.2.6 Determination of mechanical properties using RAR

We employed specific hydrodynamic models to extract elastic and viscous properties of hydrogels from RAR measurements of surface wave motion. Selection of a specific model to be used was based on the nature of the surface waves and state of the materials, as described in the following subsections.

Rayleigh waves. Rayleigh waves are the dominant mode of surface waves propagating on solid hydrogels, where the restoring force associated with elasticity dominates over surface tension or gravity. In the solid-like regime, $\frac{\Omega}{\Gamma} \gg 1$, where $\Omega = \omega + i\Gamma$ is the complex angular frequency, the angular frequency of Rayleigh wave has been found to follow the ideal law [28]

$$\omega_0 = \sqrt{\frac{\beta G k^2}{\rho}}, \tag{1}$$

where ρ is the material density, k the wavenumber, and β a Rayleigh/shear wave proportionality [29]. Therefore, shear modulus G can be obtained based on RAR measurements of angular frequency and wave number of the surface waves, using the following equation

$$G = \frac{{\omega_0}^2 \rho}{\beta k^2}. \tag{2}$$

Since hydrogels have a density close to water, we used $\rho = 1000\, kg\, m^{-3}$ and $\beta = 0.91$ in this study [29]. A 100 µl sample volume was used per well for 96-well untreated microplates in RAR, resulting a sample thickness of h ~ 3 mm. Depth effects are ignored in the surface wave dispersion relation since *tanh(kh)* > 0.99 for wavenumbers in this study (k > 1000 m^{-1}).

The damping coefficient of Rayleigh surface waves [30] is determined as

$$\Gamma = \frac{0.45 \eta k^2}{\rho}, \tag{3}$$

from which the viscosity η of the material can be determined as

$$\eta = \frac{\Gamma \rho}{0.45 k^2}. \tag{4}$$

Capillary waves. In liquids that do not have an elastic component, small wavelength (< 1 cm) surface waves are driven primarily by surface tension. In liquid-like regimes and low viscosity, the real part of the angular frequency Ω can be approximated by the Kelvin frequency

$${\omega_0}^2 = \frac{\sigma k^3}{\rho} + gk, \tag{5}$$

where k is the wavenumber, σ the surface tension, and g the gravitational acceleration which may be ignored for waves with small wavelength. The damping coefficient of a capillary wave is given by [30]

$$\Gamma = \frac{2\eta k^2}{\rho}, \qquad [6]$$

from which the viscosity η of the liquid is obtained as

$$\eta = \frac{\Gamma\rho}{2k^2}. \qquad [7]$$

Pseudo-capillary waves. For viscoelastic liquids and soft gels, both surface tension and elasticity may act as a restoring force to drive surface waves in the materials. These surface waves may be described as pseudo-capillary waves, and the dispersion relation includes both restoring forces [31]

$$\omega_0{}^2 = \frac{\sigma k^3}{\rho} + 4\frac{Gk^2}{\rho}. \qquad [8]$$

Resonant modes of surface waves. For samples with limited dimensions such as those in our experiments, resonant modes of surface waves are established due to the presence of a boundary, in our case the microwell wall. For a circular surface with a fixed boundary condition, the wavenumber of the resonant waves must satisfy the following relation,

$$k = \frac{\alpha_{m,n}}{r}, \qquad [9]$$

where r is the radius of the circular surface and $\alpha_{m,n}$ the n^{th} root of the m^{th} order Bessel function.

Measurement of material properties such as surface tension and modulus using RAR is not affected by the sample radius. While the sample radius dictates the resonant wavenumbers allowable in RAR measurements (Equation 9), the measured resonant frequency is determined by the material property given the wavenumbers, as described by equation 1, 5, or 8, depending on the nature of the surface wave.

RAR is not limited to samples of specific radius. As examples, RAR measurements in this study were taken of hydrogels cast into 96-well and 48-well microplates, creating samples with diameters of 6.7 mm and 9.8 mm respectively (Fig. 2.10). Sample radius is inversely related to wavenumber (Equation 9), and as predicted by the Rayleigh wave model (Equation 1), the natural frequency decreases with decreasing wavenumber (increasing radius). Calculation of viscoelastic properties from resonant RAR parameters allows for mechanical measurements of samples with various diameters.

The use of resonant surface waves in RAR enable the use of the wavenumbers determined by the geometry of the sample surface, thus eliminating the need to measure both wave frequency and wave speed ($c = \frac{\omega}{k}$) to determine material properties from the corresponding dispersion relations. This distinction is important because measurement of traveling surface waves requires a large surface area.

Data analysis and determination of mechanical properties from RAR measurements. We modeled the resonant surface displacement generated and detected in RAR, $x(t)$, as an underdamped harmonic oscillator

$$x(t) = A_0 e^{-\Gamma t} \sin(\omega_1 t), \qquad [10]$$

where A_0 is the initial surface displacement amplitude, ω_1 the apparent frequency, and Γ the damping coefficient.

A_0 was determined directly by fitting experimental data of surface displacement to Equation (10). We performed a least-squares curve-fitting for Lorentzian peaks on the main peak of the power spectrum from the measured surface displacement data using the findpeaksL function (https://terpconnect.umd.edu/~toh/spectrum/PeakFindingandMeasurement.html) for MATLAB to identify ω_1, the peak position, and Γ, the half-width at half-maximum (HWHM) [32]. We then calculated the intrinsic or natural frequency ω_0 of the surface oscillation

$$\omega_0 = \sqrt{{\omega_1}^2 + \Gamma^2}, \qquad [11]$$

which was used to determine the modulus and viscosity using the correspondingly appropriate dispersion relation, in conjunction with Equation (4) or Equation (7), depending on the nature of the surface waves.

2.2.7 Finite element analysis (FEA) modeling of RAR using COMSOL

Empirical RAR data were validated by simulating the response of a 3-dimensional (3D) hydrogel to ultrasound excitation and determining the expected surface displacement at the center of the sample using finite element analysis (FEA). An FEA model was generated using COMSOL by replicating the specific sample and excitation parameters used in RAR measurements (100 µl samples in a 96 well plate). A 2D axisymmetric model was created for the cylindrical sample geometry with a 3.2 mm radius and 3 mm height. The Structural Mechanics module was used to model the mechanical behavior of the sample as a linear viscoelastic material with fixed boundaries on the bottom and cylindrical sides, where the sample would contact the rigid microplate, as well as a free boundary on the surface of sample. A pulsed boundary load was defined on the sample surface using a Gaussian distribution to model the acoustic pressure field of the focused transducer. A time dependent study was performed to model the displacement distribution both inside the material and at the top surface as a function of time, capturing the response of the material to ultrasound excitation.

2.2.8 Shear rheometry

The storage modulus G' and loss modulus G'' of hydrogels were measured using a parallel-plate AR-G2 rheometer (TA Instruments) with an 8 mm diameter head using samples made in the same manner as those characterized by RAR. Due to the rapid stress relaxation of low concentration hydrogels, a gap height of 1.7 mm was used for all samples to ensure full contact with 500 µl gels cast in 24-well microplates. The plate was centered in the microwell to minimize edge effects. An 8 mm disk of 800 grit sandpaper was adhered to the measurement head prior to testing to prevent slipping. Endpoint shear measurements of fibrin, gelatin, and agarose hydrogels with known concentrations were performed at 20 °C. A frequency sweep was performed for each sample, ranging from a 0.1 to 10 Hz oscillatory frequency. Oscillatory frequencies greater than 1 Hz showed substantially increased variability due to the instrument inertia, which was observed in raw phase angles greater than 90° [33]. A strain sweep was subsequently performed for each sample using an oscillation frequency of 1 Hz with strain amplitude ranging from 0.1% to 10%. Measurements used in subsequent analysis were taken from the strain sweep with strains selected for each material to stay within the linear viscoelastic region.

Fibrin gels for dynamic shear measurements were prepared using the same protocol as with RAR, except that 500 µl volumes were pipetted into 24-well microplates that had been heated to 37 °C on the rheometer's Peltier stage. One minute after thrombin addition, a 30 minute time sweep was started, with an angular frequency of 1 Hz and strain amplitude of 1 %.

2.2.9 Comparison of RAR and shear rheometry measurements

To directly compare the viscoelastic parameters of hydrogels measured using RAR (G and η) and shear rheometry (G' and G''), a Kelvin-Voigt (KV) model was used to relate the complex shear modulus G^* with the values of $G, \eta,$ and ω_0 obtained from RAR [29],

$$G^* = G + i\omega_0\eta, \tag{12}$$

and with the G' and G'' obtained from shear rheometry [34]

$$G^* = G' + iG''. \tag{13}$$

Equating equation (12) and (13) produces

$$G = G', \tag{14}$$

$$\omega_0 \eta = G''. \tag{15}$$

To examine the relative contribution of viscous and elastic components of the complex modulus for both techniques, the loss factor $\tan(\delta)$ was calculated using

$$\tan(\delta) = \frac{G''}{G'} = \frac{\omega_0 \eta}{G}, \tag{16}$$

which provides a measure of how well a dynamically deformed material dissipates energy.

2.2.10 Statistical analysis

All data are presented as mean ± 95% confidence interval. Analysis of variance (ANOVA) was performed for results involving more than two variables, using an F-test with significant variable defined according to $p < 0.05$. Differences between groups were determined using a Student's two-tailed t-test with a Bonferroni multiple comparison correction, such that differences were considered statistically significant when $p < \frac{\alpha}{m}$ for $\alpha = 0.05$ and m is the number of comparisons tested on a figure.

2.3 Results and Discussion

2.3.1 Generation and detection of resonant surface waves using RAR

Figure 2.3 shows RAR data collected on fibrin hydrogel samples with varying concentrations. The left panels of Figs. 2.3A, B, and C are representative M-mode images from fibrin gels with concentrations of 4.0, 6.0, and 8.0 mg/ml, respectively. The vertical axis in these images represents the vertical location (z) along the line-of-sight of the ultrasound pulse, with reference point z = 0 set at the equilibrium location of the sample surface (z = 0, t = 0) before RAR excitation. The horizontal axis represents the time course of pulse-echo imaging at a PRF of 4 kHz

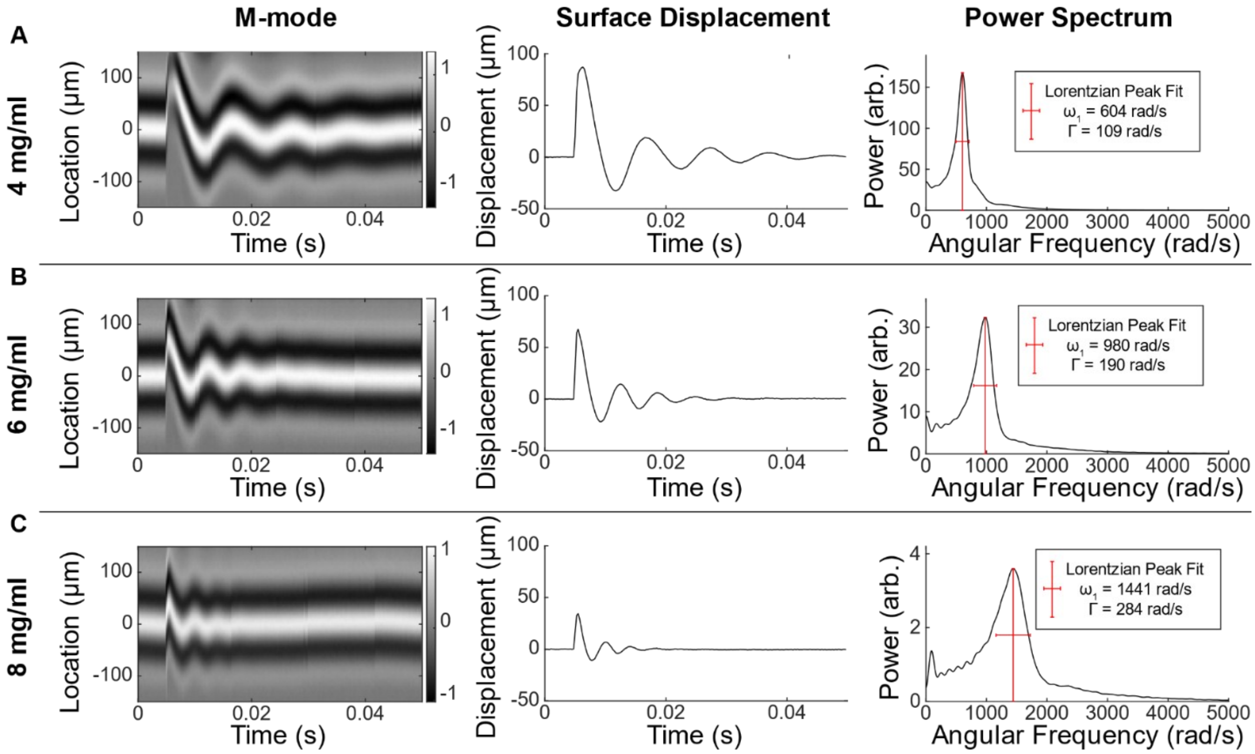

Figure 2.3: M-mode grayscale images showing pulse-echo surface reflections during RAR measurements (left panels), surface displacement versus time (center panels), and frequency power spectrums for oscillatory surface displacements (right panels). Experiments used fibrin hydrogels at concentrations of (A) 4.0 mg/ml, (B) 6.0 mg/ml, and (C) 8.0 mg/ml.

(i.e. time interval of 250 μs between pulses). Brightness in the image represents the amplitude of the received RF signals. The strong reflection from the air-sample interface is clearly evident. Upon application of the excitation ultrasound pulse at t = 0.005 s, the surface location was displaced upwards, and the evolution of the surface oscillation could be observed over time from these images. The center panels of Fig. 2.3A-C show line plots of z(t) to more clearly show the surface oscillations for these samples. The amplitude of the waves decreased with increasing fibrin concentration and the displacement time curves clearly exhibited the characteristics of a damped harmonic oscillator. The corresponding power spectra of the surface oscillations (right panels of Fig. 2.3A-C) show that the resonant frequency (ω_1) increased with increasing fibrin concentration, which was accompanied by widening of the HWHM, indicating increased stiffness and damping coefficients in gels at higher fibrin concentration.

2.3.2 Characteristic parameters of resonant surface waves measured using RAR

Figure 2.4 shows the characteristic parameters of surface waves produced in hydrogels and how they were affected by the amplitude and duration of the excitation ultrasound pulse. In this study, fibrin gels of defined polymer concentration (2-10 mg/ml) were characterized with RAR using one of two acoustic pressures (2 MPa or 3 MPa), and for a duration of either 33 µs or 66 µs. At a given fibrin gel concentration, the natural frequency of the resonant mode of the surface waves (ω_0) was unaffected by the amplitude and duration of the acoustic excitation (Fig. 2.4A).

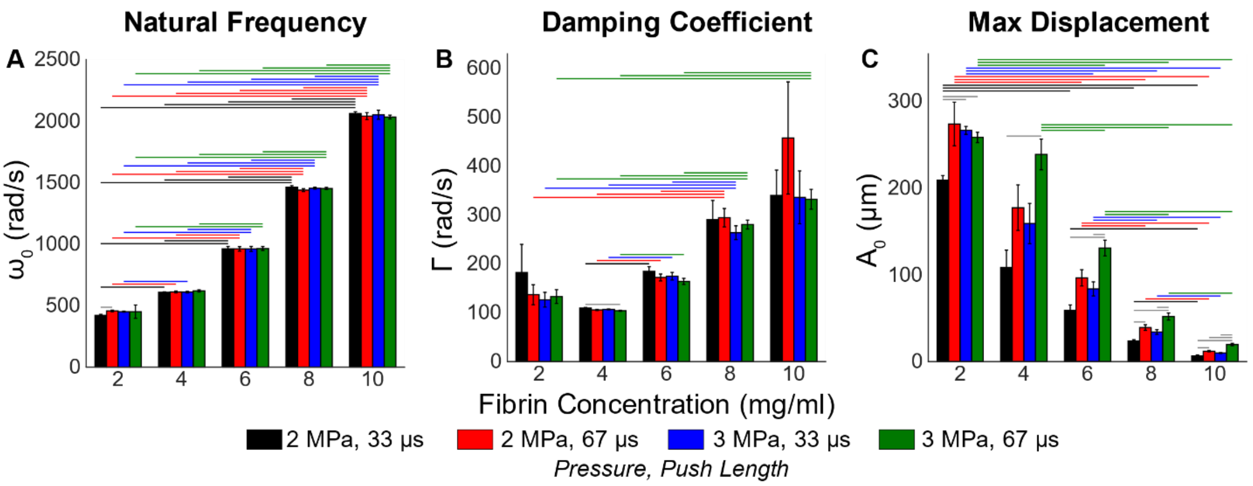

Figure 2.4: Comparisons of A) natural frequency ($\boldsymbol{\omega_0}$), B) damping coefficient (**Γ**), and C) maximum displacement ($\boldsymbol{A_0}$) extracted from RAR experiments using multiple ARF excitation pressures (2 and 3 MPa) and durations (33 and 66 µs) on fibrin gels with concentrations between 2 and 10 mg/ml. Error bars represent a 95% confidence interval (n=4). Lines above bars indicate statistically significant differences at $p < 0.05$.

Similarly, the damping coefficient (Γ) showed little change with varying excitation acoustic pressure and duration (Fig. 2.4B). However, increasing the fibrin concentration significantly and consistently increased the resonant frequency and damping coefficient, indicating that gels with higher fibrin concentration have a higher modulus and exhibit more viscous damping. Importantly, these results demonstrate that RAR measures intrinsic material characteristics independent of the excitation pulse amplitude and duration. In contrast, the amplitude of the maximum surface deformation (A_0), exhibited strong dependence on both excitation parameters as well as polymer concentration (Fig. 2.4C). For gels with a low fibrin concentration (2 mg/ml), the deformation amplitude increased when excitation pulse duration increased from 33 μs to 66 μs at the acoustic pressure of 2.0 MPa but stayed constant with increased duration at the acoustic pressure of 3.0 MPa. This behavior suggests a possible saturation of response in the soft gels at higher acoustic pressure, since the maximum amplitude of the surface wave is limited. For gels with higher fibrin concentrations (4-10 mg/ml), the amplitude of deformation increased with increasing acoustic pressure and pulse duration, as expected. Similarly, higher fibrin concentration, which leads to stiffer gels, consistently resulted in lower deformation amplitudes under the same excitation pulse parameters.

2.3.3 Characterization of hydrogels using RAR

Figure 2.5 shows RAR data generated from hydrogel materials commonly used in tissue engineering: fibrin (2.0-10.0 mg/ml), gelatin (20 - 100 mg/ml), and agarose (2.0 – 10.0 mg/ml). In all materials, the resonant frequency of surface waves (ω_0) increased significantly with increasing

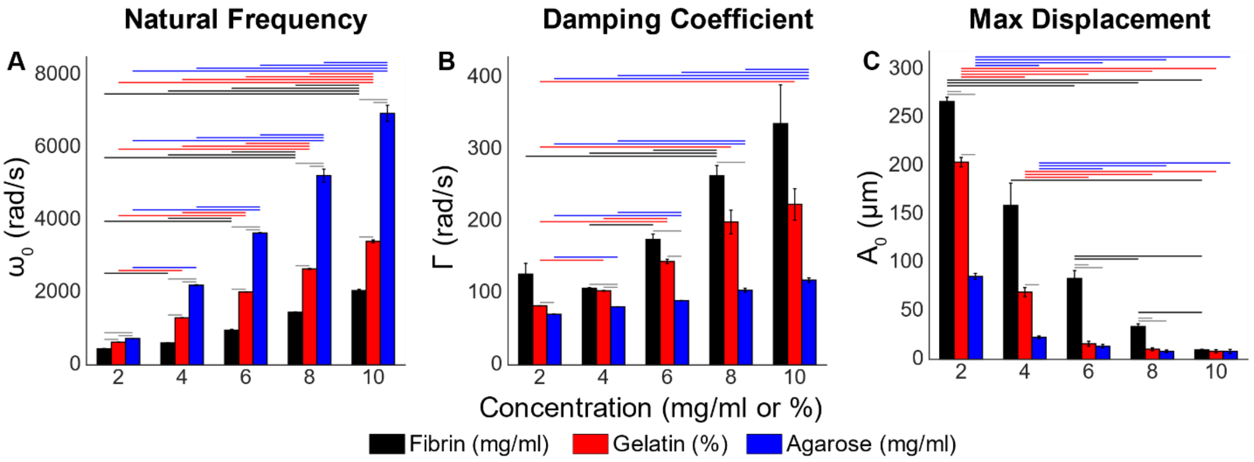

Figure 2.5: Comparisons of A) natural frequency ($\boldsymbol{\omega_0}$), B) damping coefficient ($\boldsymbol{\Gamma}$), and C) maximum displacement ($\boldsymbol{A_0}$) extracted from RAR experiments on fibrin (2-10 mg/ml), gelatin (2-10 wt%), and agarose (2-10 mg/ml) gels. Error bars represent a 95% confidence interval (n=4). Lines above bars indicate statistically significant differences at p < 0.05.

polymer concentrations (Fig. 2.5A), suggesting increasing stiffness. Fibrin gels had the lowest and agarose gels had the highest ω_0 values at the same polymer concentration. The damping coefficient (Γ) also increased with polymer concentration in all hydrogels (Fig. 2.5B). Interestingly, fibrin gels had the highest and agarose gels the lowest damping coefficient, in a trend opposite to that of the resonant frequency. The maximum surface deformation amplitude (A_0) decreased with increasing polymer concentration (Fig. 2.5C). In general, higher A_0 values were measured in fibrin, though at higher polymer concentrations the wave amplitude was relatively low, and this effect was not statistically significant.

Taken together, these data show that RAR measurements of resonant frequency and damping coefficient were independent of the ultrasound excitation parameters, while surface displacement amplitude depended on the magnitude and duration of the pushing pulse. Corresponding experiments performed using gelatin and agarose hydrogels at varying acoustic pressure and pulse duration showed similar results (Fig. 2.6). Statistical analysis of the combined fibrin, agarose and gelatin data set revealed that polymer type and concentration significantly affected the resonant frequency (ω_0), damping coefficient (Γ), and maximum amplitude (A_0) of the surface resonance. However, only the amplitude was significantly impacted by acoustic pressure or impulse duration. While displacement amplitude can provide important information on the relative stiffness of different materials, this parameter depends on the energy of the excitation pulse and thus is system dependent.

Due to the finite transverse focal size of the ultrasound beam used for pulse-echo measurement, the received echo signals from the sample surface will be an average of the reflections within the focal zone. While this averaging may affect the absolute values of the echo signal amplitude, it is not expected to influence the temporal characteristics, thus the frequency of the surface movements. Therefore, in this study the amplitude parameters were not used for material characterization, instead we used the measurements of system-independent resonant frequency and damping coefficient in subsequent materials characterization.

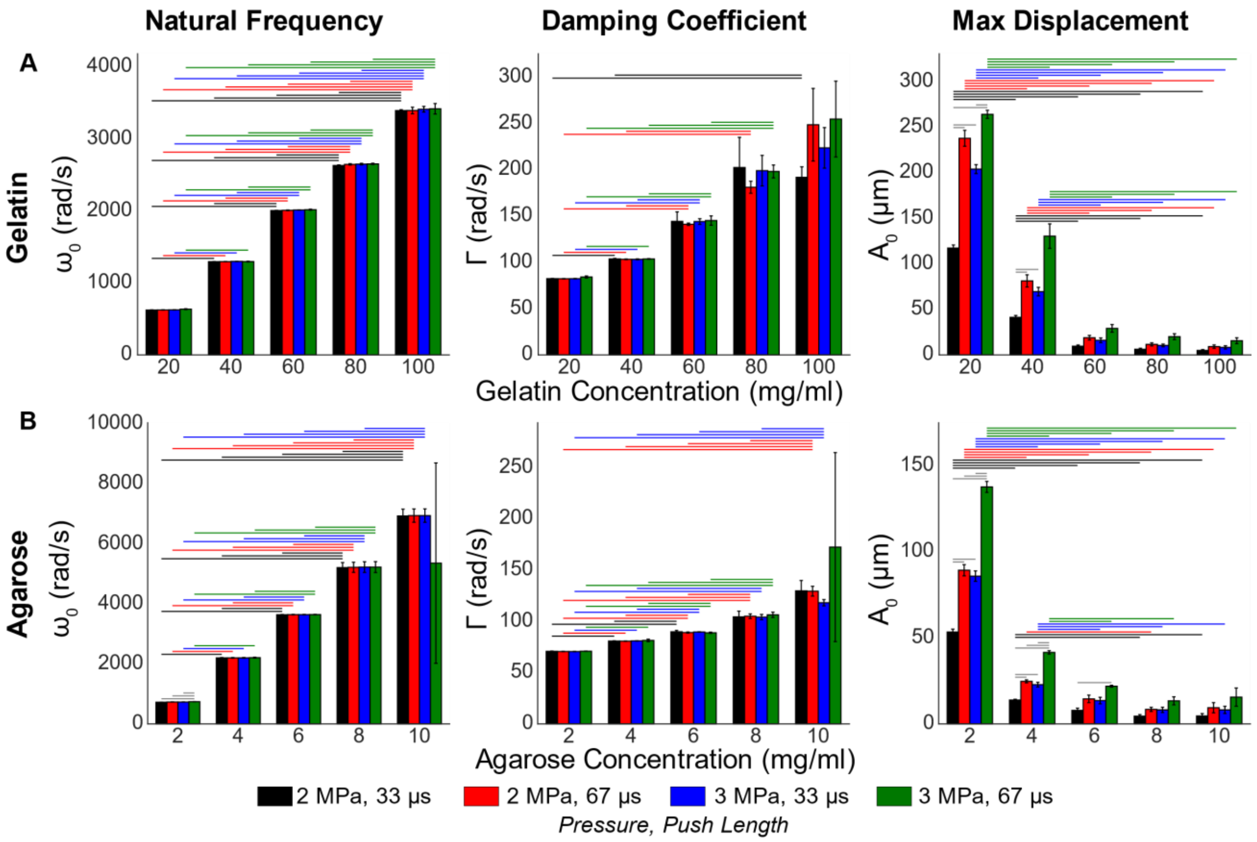

Figure 2.6: A) Comparisons of natural frequency ($\boldsymbol{\omega_0}$), damping coefficient ($\boldsymbol{\Gamma}$), and maximum displacement ($\boldsymbol{A_0}$) extracted from RAR experiments using multiple ARF excitation pressures (2 and 3 MPa) and durations (33 and 66 µs) on gelatin gels with concentrations between 20 and 100 mg/ml. B) Pressure and duration sweeps were also performed for agarose gels (2-10 mg/ml), comparing $\boldsymbol{\omega_0}$, $\boldsymbol{\Gamma}$, and $\boldsymbol{A_0}$. Error bars represent a 95% confidence interval (n=4). Lines above bars indicate significant differences according to a two-tailed students t-test with a Bonferroni correction ($p < 0.05$).

We also examined the sensitivity of RAR to changes in the concentration of the hydrogels. A linear regression was performed for polymer concentration as a function of measured RAR frequency, identifying the 95% prediction interval over the whole concentration range (Fig. 2.7).

The standard error for fibrin concentration over the entire 2 mg/ml to 10 mg/ml concentration range was 0.66 mg/ml, very high compared to the concentration (Fig. 2.7A).

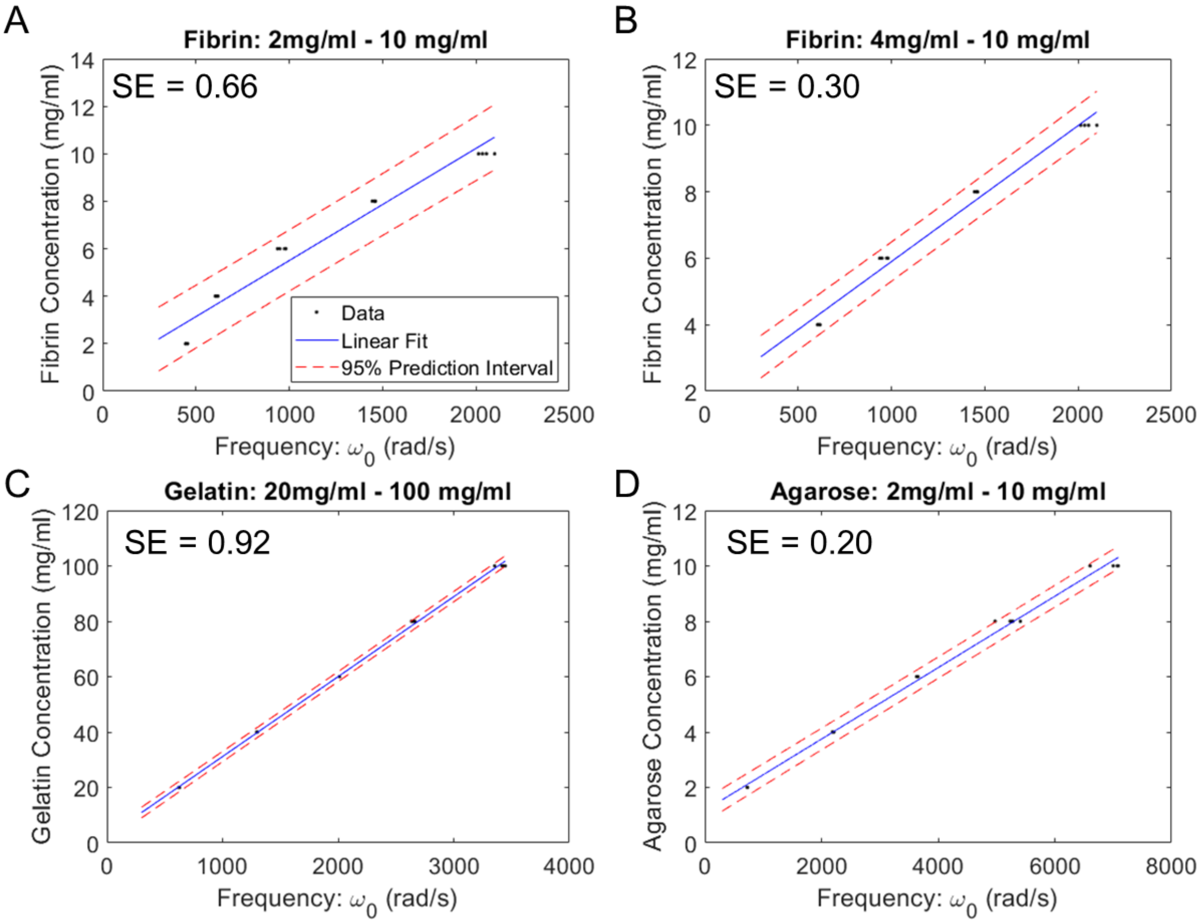

Figure 2.7: Comparison of concentration sensitivity in RAR frequency measurements for A) the full range of fibrin, B) a subset of fibrin, C) gelatin, and D) Agarose. Red dashed lines represent the 95% prediction interval (n=4).

Interestingly, omitting the lowest fibrin concentration resulted in a substantial reduction in the standard error to 0.30 mg/ml (Fig. 2.7B). Low standard errors relative errors were calculated for the gelatin (Fig.2.7C) and agarose (Fig.2.7D) samples, 0.92 mg/ml and 0.20 mg/ml, respectively. While higher than other materials, the gelatin standard error is extremely low compared to the concentrations used in this study which were 10-fold greater than those of agarose or fibrin. Taken together, these results indicate that RAR measurements of natural frequency are highly sensitive to changes in material concentration, with a linear relationship for all but the softest materials.

2.3.4 Validation of surface wave models using finite element analysis

Finite element analysis (FEA) conducted using COMSOL was used to simulate the 3D behavior of hydrogel samples subjected to ultrasound excitation, with the goals of verifying the resonant mode of surface waves in our RAR experiments and validating the analytical models of surface waves on viscoelastic solids (Equations 1-8). Figure 2.8 shows the results of COMSOL simulations of surface movement following a single ultrasound excitation pulse. The surface displacement map shows an annular node (Fig. 2.8A - B), indicating that $(0,2)$ is the dominant resonant mode using our experimental set-up. The time evolution of the surface displacement at the center of the circular surface (Fig. 2.8C) exhibits similar behaviors as the data from RAR experiments, and the power spectrum of the surface oscillation corresponding to a (0, 2) resonant mode (Fig. 2.8D) match well with those from RAR measurements. Simulation was also performed to investigate the impact of the magnitude and duration of the excitation pulses, as in our empirical studies, and similar trends were observed (Fig. 2.9A). In addition, the effect of changing the geometry of the excitation beam was investigated (Fig. 2.9B).

To further validate the RAR technique, the COMSOL model was applied to systematically investigate how surface waves are affected by varying shear modulus (0.05-30 kPa) and viscosity (0.001-0.3 Pa·s) for the dominant (0, 2) mode. We used the surface movement at the center of the circular surface to determine the resonant frequency and damping coefficient, which were then used to calculate G and η, in the same manner as for experimental RAR results. Plots of the input material properties against those derived from the surface movements from COMSOL model showed strong correlation for both G and η. The COMSOL model exhibited a 15% under-prediction of shear modulus compared to RAR; however, excellent linear correlation ($R^2 > 0.99$) was observed (Fig. 2.8E). The model-derived shear viscosity also demonstrated a strongly linear

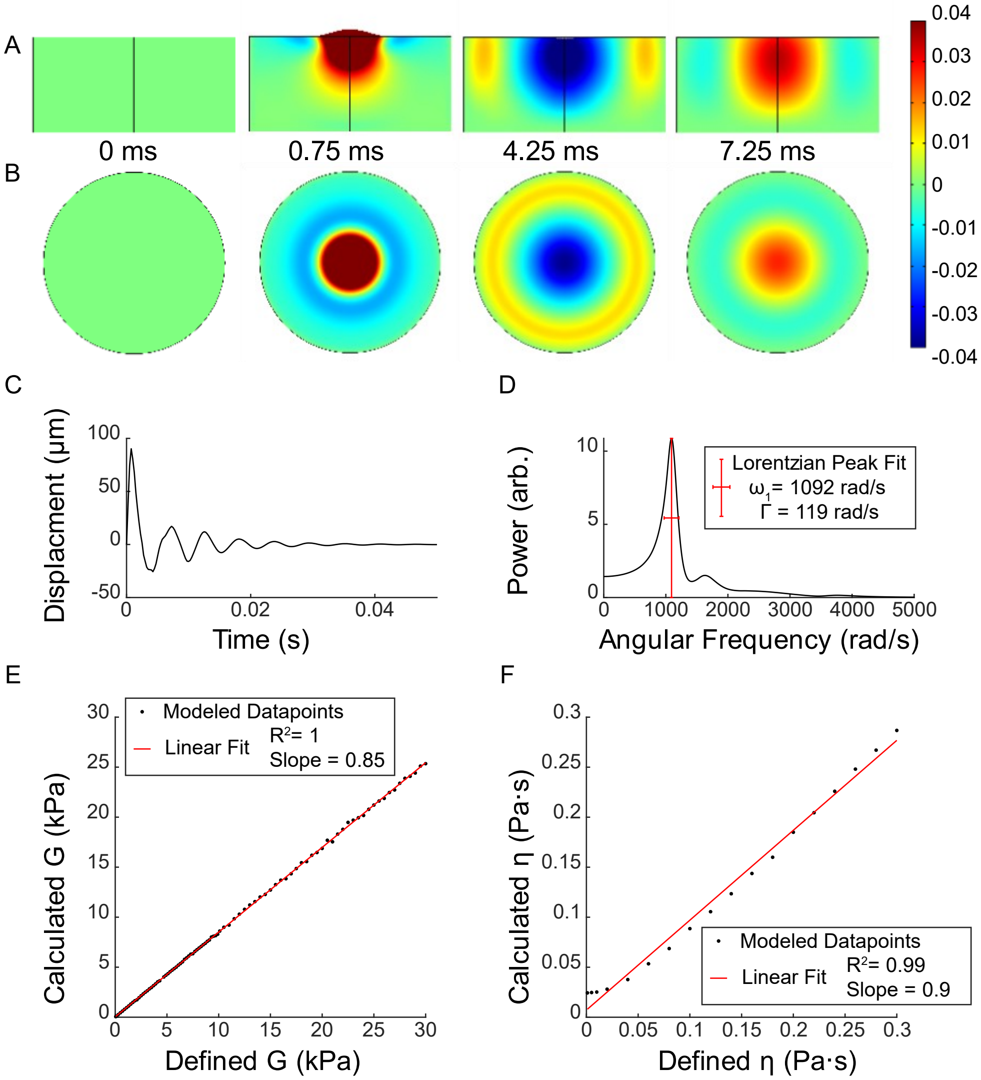

Figure 2.8: FEA displacement maps generated using a COMSOL simulation of an RAR experiment for A) vertical cross-section and B) top surfaces at multiple time points. From left to right, displacement maps show sample baseline preceding ARF excitation (0.0 ms), maximum deformation at end of ARF excitation (0.75 ms), and downward (4.25 ms) and upward (7.25 ms) center deformation during subsequent resonant oscillation. C) Modeled displacement versus time from center of sample surface. D) Frequency power spectra for modeled surface displacements. Viscoelastic material properties were defined as G = 500 Pa and $\boldsymbol{\eta}$ = 0.1 Pa·s for A-D. Comparison of E) shear moduli (G) and F) shear viscosities ($\boldsymbol{\eta}$) defined in FEA with those calculated using RAR analytical method.

relationship with the input values ($R^2 = 0.99$), although the analytical model over-predicted when $\eta < 0.03$ Pa·s (Fig. 2.8F). This discrepancy is due to the very narrow peaks of resonant frequency from simulation, resulting in a poor fitting of the Lorentzian peak width. These discrepancies may also be attributed to other viscous effects in the empirical system that are not considered in the COMSOL model.

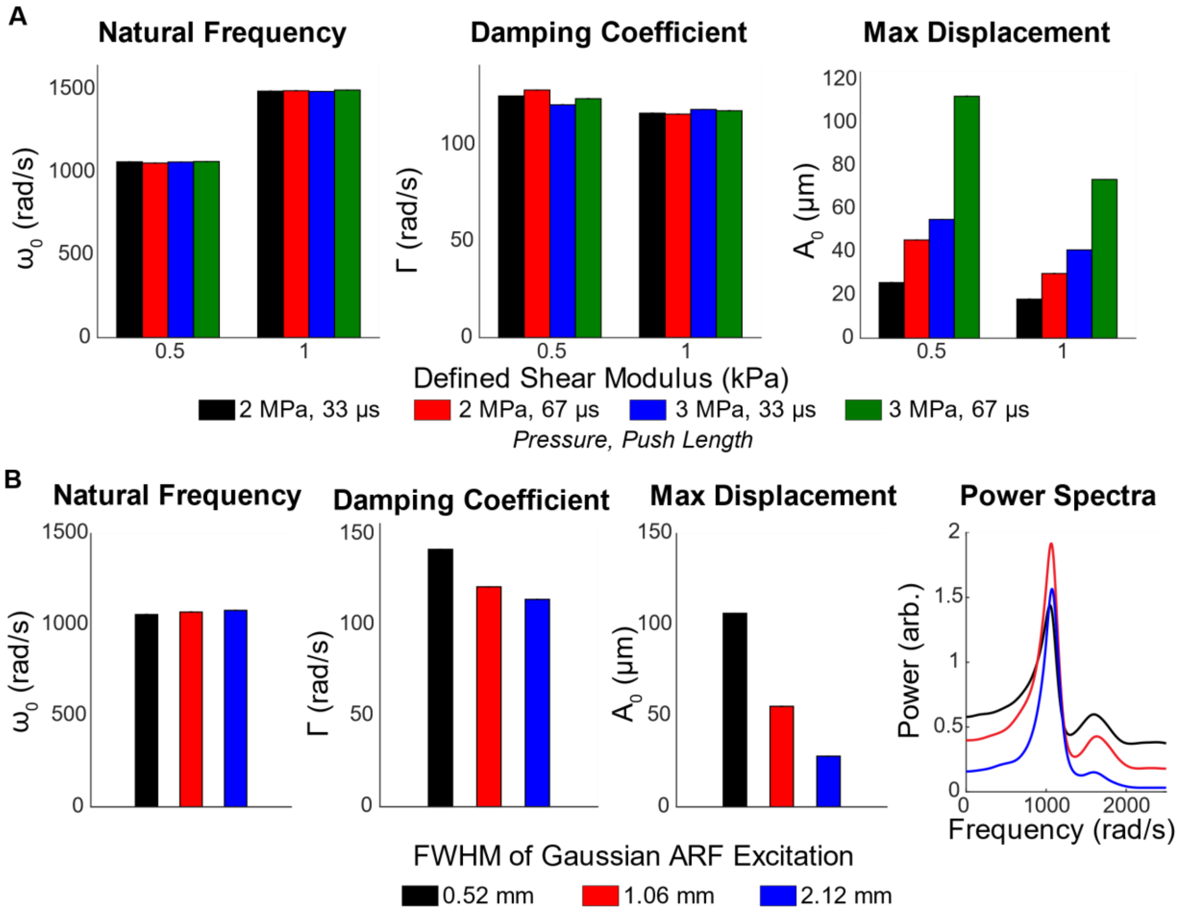

Figure 2.9: A) Comparisons of natural frequency ($\boldsymbol{\omega_0}$), damping coefficient ($\boldsymbol{\Gamma}$), and maximum displacement ($\boldsymbol{A_0}$) extracted from FEA models using multiple ARF excitation pressures (2 and 3 MPa) and durations (33 and 66 µs) with viscoelastic samples (G = 0.5 or 1 kPa, and $\boldsymbol{\eta}$ = 0.1 Pa·s). As with the experimental RAR, the modeled resonant surface behavior showed minimal effect of excitation parameters on the resonant frequency ($\boldsymbol{\omega_0}$) or damping coefficient ($\boldsymbol{\Gamma}$), while maximum amplitude ($\boldsymbol{A_0}$) varied substantially between each setting. B) Comparisons of natural frequency ($\boldsymbol{\omega_0}$), damping coefficient ($\boldsymbol{\Gamma}$), and maximum displacement ($\boldsymbol{A_0}$) extracted from FEA models using multiple Gaussian excitation geometries with FWHM of intensity between 0.52 mm and 2.12 mm with viscoelastic samples (G = 0.5 kPa, and $\boldsymbol{\eta}$ = 0.1 Pa·s). As with changes in excitation intensity and duration, changes in ARF excitation lateral beam profile affect maximum amplitude ($\boldsymbol{A_0}$) but not the resonant frequency ($\boldsymbol{\omega_0}$). Comparisons of power spectra showed that narrower beam profile led to more energy distribution outside the main mode, effectively resulting in a slight increase in the damping coefficient ($\boldsymbol{\Gamma}$) for the main mode.

2.3.5 Comparison of RAR with shear rheometry

The intrinsic viscoelastic properties of hydrogels were calculated using RAR measurements according to the hydrodynamic models for Rayleigh waves (Equations 2 and 4). Results in Figure 2.10 show that the RAR could be validated against with those obtained with

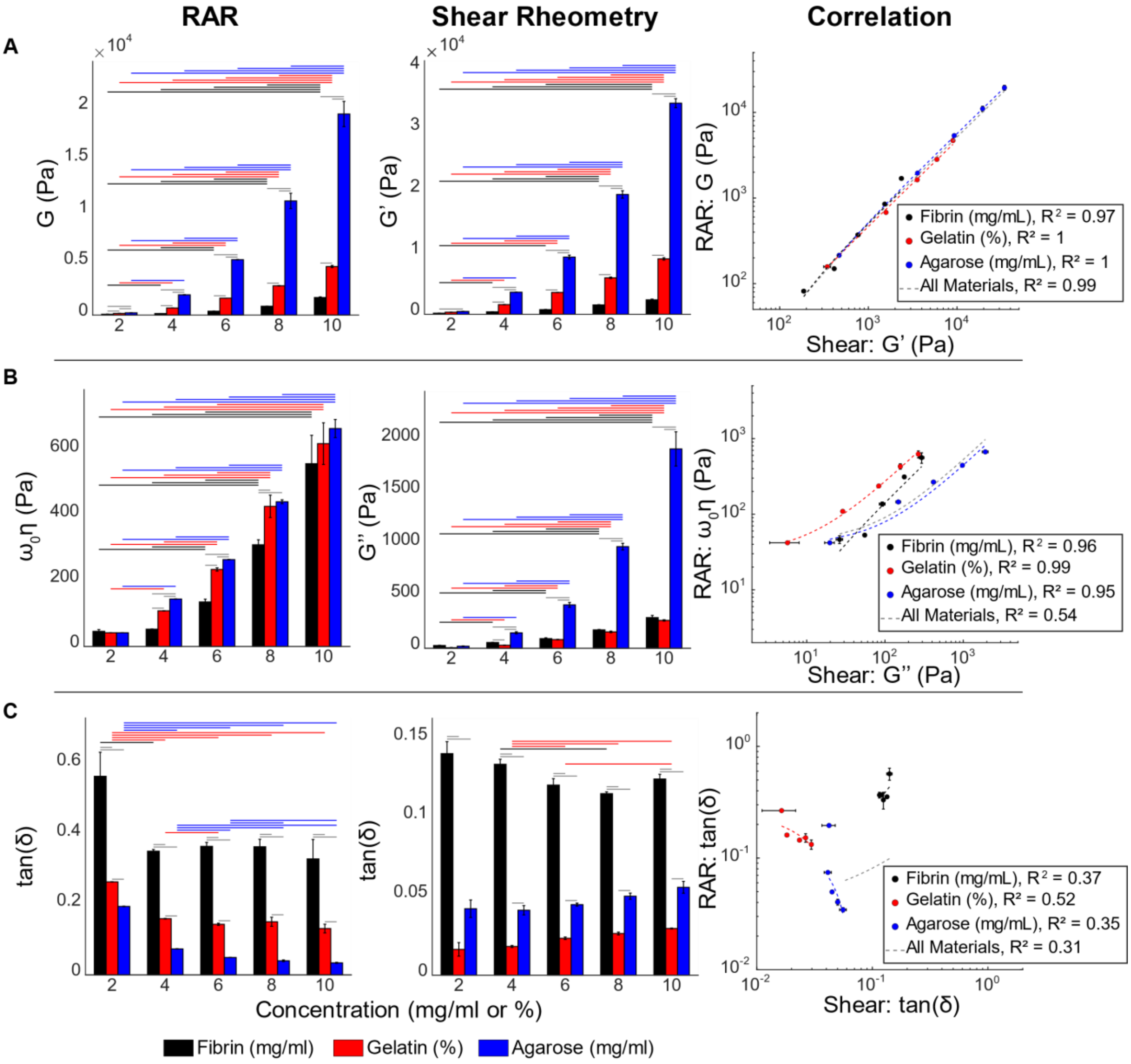

Figure 2.10: RAR and shear rheometry measurements of the viscous and elastic properties of fibrin (2-10 mg/ml), gelatin (2-10 wt%), and agarose (2-10 mg/ml) gels. A) Elastic parameters (G, G') and correlations. B) Viscous parameters ($\boldsymbol{\omega_0 \eta}$, G'') and correlations. C) Loss factor (tan(δ)) and correlations. Error bars represent a 95% confidence interval (n=4). Lines above bars indicate statistically significant differences at $p < 0.05$.

rotational shear rheometry, a commonly used technique to characterize soft biomaterials.

Figure 2.10 shows RAR and shear rheometry data for fibrin hydrogels, as well as the correlation between the values generated by each method. The elastic modulus consistently increased with increasing polymer concentration for all types of hydrogels (Fig. 2.10A) when measured using RAR (G) or with shear rheometry (G'). The correlation between the two methods was high ($R^2 > 0.95$), with slopes ranging from 0.47 to 0.56, showing that these techniques can provide very similar information on material stiffness.

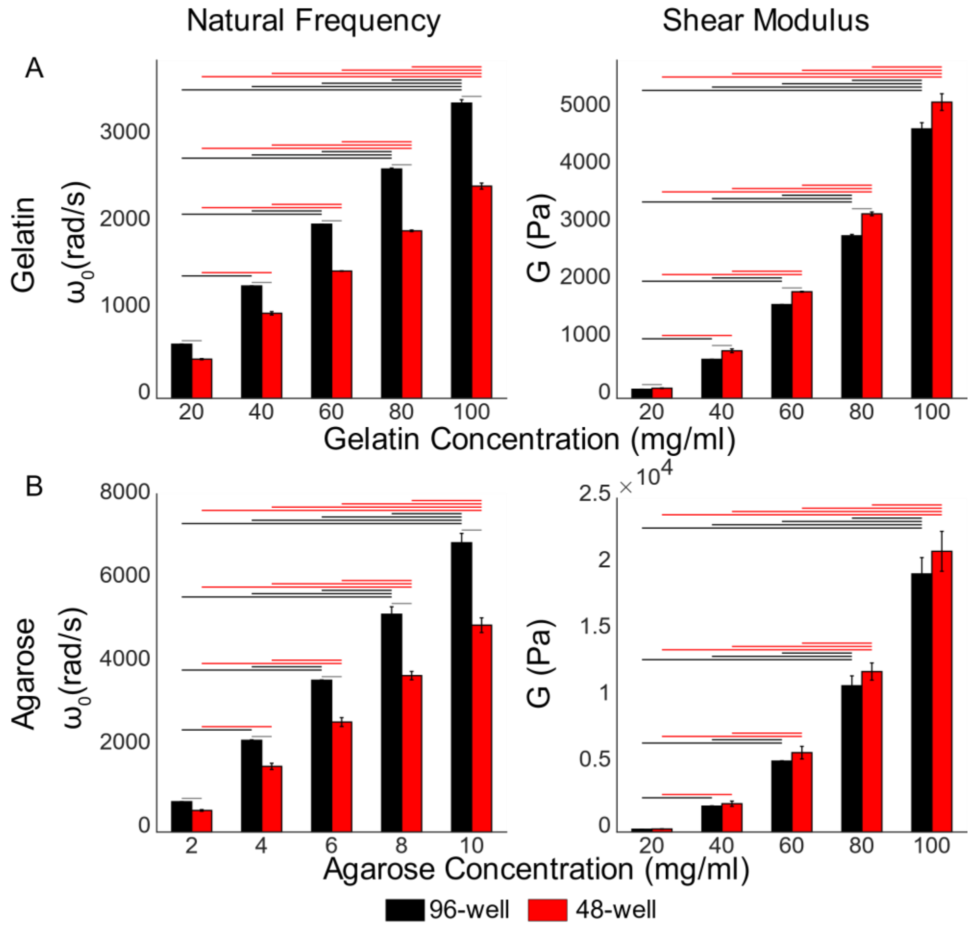

Figure 2.11: A) Comparisons of natural frequency ($\boldsymbol{\omega_0}$), and shear modulus (**G**) extracted from RAR experiments on gelatin gels cast into 96-well and 48-well microplates with concentrations between 20 and 100 mg/ml. B). Agarose gels were also cast into 96-well and 48-well microplates at concentrations between 2 and 10 mg/ml, comparing $\boldsymbol{\omega_0}$ and **G** measured with different geometries. Error bars represent a 95% confidence interval (n=4). Lines above bars indicate significant differences according to a two-tailed students t-test with a Bonferroni correction ($p < 0.05$).

Viscosity parameter measurements from both RAR ($\omega_0\eta$) and shear rheometry (G'') were also consistent and increased with increasing polymer concentration (Fig. 2.10B), though the absolute value of the parameters differed between techniques. Interestingly, the viscous parameters were highly correlated for each individual material ($R^2 > 0.95$), but not for all materials grouped together ($R^2 = 0.54$). The slopes of the linear regression curves ranged from 0.41 for the polysaccharide agarose hydrogels, to 1.5 and 2.4 for the peptide-based fibrin and gelatin materials.

In RAR, the frequencies measured are the discrete frequencies of the resonant surface wave modes in a specific experiment, determined by both the radius and the mechanical properties of the sample. In the current study, we did not perform experiments to systematically investigate the frequency dependence of the modulus, although it is possible to measure viscoelastic parameters, (e.g. G', G", viscosity, and tan-delta) as a function of frequency using custom fabricated sample holders with variable radius.

It should be noted that the undriven resonant surface waves generated during RAR oscillated with relatively high frequencies (70-1100 Hz were measured for the range of hydrogel samples tested) compared to the driven oscillations of shear rheometry (1 Hz). The Kelvin-Voigt model of viscoelasticity assumes Newtonian behavior, whereas the measured shear viscosity of these hydrogels may be affected by the shear rate [35]. More complex models of viscoelastic behavior, such as the Standard Linear Solid may be applied to in future studies to improve comparisons of the two measurement techniques. The wavenumber and thus the measured resonant frequency of the surface wave is dependent on the sample radius in RAR. Due to the potential dependence of material properties on frequency, the material properties derived from measured resonant frequency in RAR may be affected by the sample radius.

The relative contribution of elastic and viscous components of the complex modulus is described by the loss factor ($\tan(\delta)$). Measurement using RAR suggested that the loss factor decreased initially as polymer concentration increased, but generally plateaued at higher concentration (Fig. 2.10C). The loss factor for the hydrogels tested ranged from 0.03-0.6, suggesting that elastic behavior dominated the viscoelastic response to deformation. The loss factor as measured by shear rheometry generally ranged from 0.01-0.15, suggesting an even stronger dominance of the elastic component, approaching the behavior of an ideal elastic solid. The shear rheometry measurements also showed a relatively weak dependence on polymer concentration, and fibrin had the most viscous character. A direct comparison of the $\tan(\delta)$ values showed only weak correlations between the methods. The values for fibrin clustered, while both gelatin and agarose had a generally negative slope with only modest correlation. These results suggest that RAR and shear rheometry measure different aspects of the viscoelastic behavior of materials associated with viscous energy losses.

2.3.6 Dynamic characterization of fibrin gelation using RAR

RAR is suitable for characterizing both liquid and hydrogel phases, and therefore was used to monitor the dynamics of the sol-gel transition in fibrin after addition of varying concentrations (0.1-0.4 U/ml) of thrombin. Figure 2.12 shows RAR data from non-contact measurements taken every 0.5 min for a period of 30 min. The initially liquid fibrinogen solution exhibited a consistent natural resonant frequency of about 420 rad/s (Fig. 2.12A), corresponding to capillary waves induced by the ultrasound pulse. There was a concentration-dependent lag in the action of thrombin, after which the resonant frequency increased rapidly, before plateauing at a maximum value. This three-phase profile corresponds to the mechanism of thrombin-catalyzed fibrin gelation, which includes cleavage of fibrinopeptides, formation of protofibrils, and aggregation of

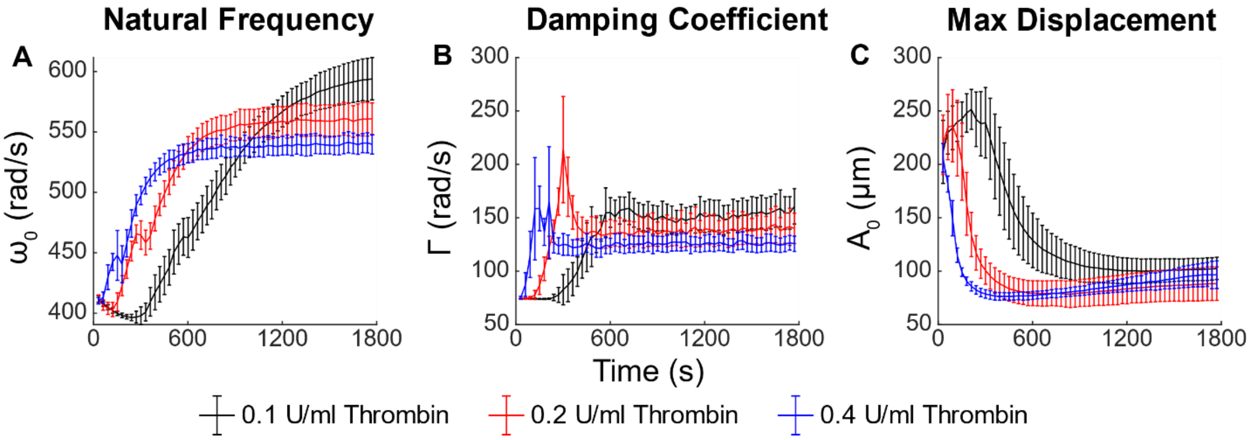

Figure 2.12: Dynamic RAR measurements of A) natural frequency ($\boldsymbol{\omega_0}$), B) damping coefficient ($\boldsymbol{\Gamma}$), and C) maximum displacement ($\boldsymbol{A_0}$) extracted during gelation of 4.0 mg/ml fibrin gels with thrombin concentrations of 0.1, 0.2, and 0.4 U/ml. Error bars represent a 95% confidence interval (n=7).

the gel network [36,37]. Increasing thrombin concentration resulted in a shortened lag period, higher rate of resonant frequency increase during the aggregation phase and decreased maximum frequency.

The damping coefficient of the materials also exhibited a three-phase profile, with a lag phase, a rapid rise to a peak value, and then a drop to a plateau level (Fig. 2.12B). The peak in the damping coefficient occurred earlier at higher thrombin concentration, indicative of faster gelation kinetics, while the plateau level was lower for higher thrombin concentrations. Damping coefficients for Rayleigh waves are nearly 5-fold smaller than for capillary waves at the same material viscosity [30]. Therefore, the distinct peak in damping coefficient during gel formation may indicate a phase transition from viscoelastic fluid to viscoelastic solid, during which the viscosity effect increases to a maximum in the liquid phase followed by a decrease in the solid phase.

Examination of the maximum surface displacement (A_0) over time (Fig. 2.12C) can be informative, given that the ultrasound parameters are kept the same for all the samples. Generally, A_0 increased initially after thrombin addition, but then steadily decreased as gelation progressed, until reaching a plateau level. The time-varying value of A_0 was dependent on the thrombin concentration, with higher concentrations resulting in a more rapid trajectory to the plateau level. Interestingly, A_0 appeared to increase slightly at first after thrombin addition for the samples with 0.1 and 0.2 U/ml thrombin, before peaking and then decreasing steadily to a plateau level. The peak is not evident at 0.4 U/ml thrombin, possibly because it occurred prior to the initiation of measurements (there was a 60 s delay after thrombin addition before detection could be achieved in our system). Interestingly, the peak in A_0 occurred before the phase transition time point associated with the damping coefficient peak (Fig. 2.12B), suggesting that distinct processes are occurring during fibrin gel formation.

2.3.7 Comparison of dynamic material properties using RAR and shear rheometry

RAR data was used to characterize the viscoelastic properties of fibrin materials over time as they gelled *in situ*. The local maximum in the damping coefficient was thought to indicate the phase transition from liquid to a solid fibrin gel [32]. The capillary wave model, Equation 1, was used at the beginning of the experiments when the samples were liquid. The pseudocapillary model, described by Equations 7 and 8, was applied to RAR measurements prior to this transition and the Rayleigh model, Equations 2 and 4, as applied to measurements following this phase transition. Figure 2.12. shows values of G, $\omega_0\eta$, and $\tan(\delta)$ from RAR data, the corresponding shear rheometry measurements, as well as correlation plots between these parameters. The elastic modulus parameters (Fig. 2.13A) generally exhibited an initial lag followed by a sigmoidal increase to a plateau value over time. The duration of the lag and the slope of the curve were dependent on thrombin concentration, reflective of faster gelation due to increased thrombin availability. RAR measurements show that the maximum shear modulus increased with decreasing thrombin concentration, a behavior that has been observed in prior studies and is attributed to

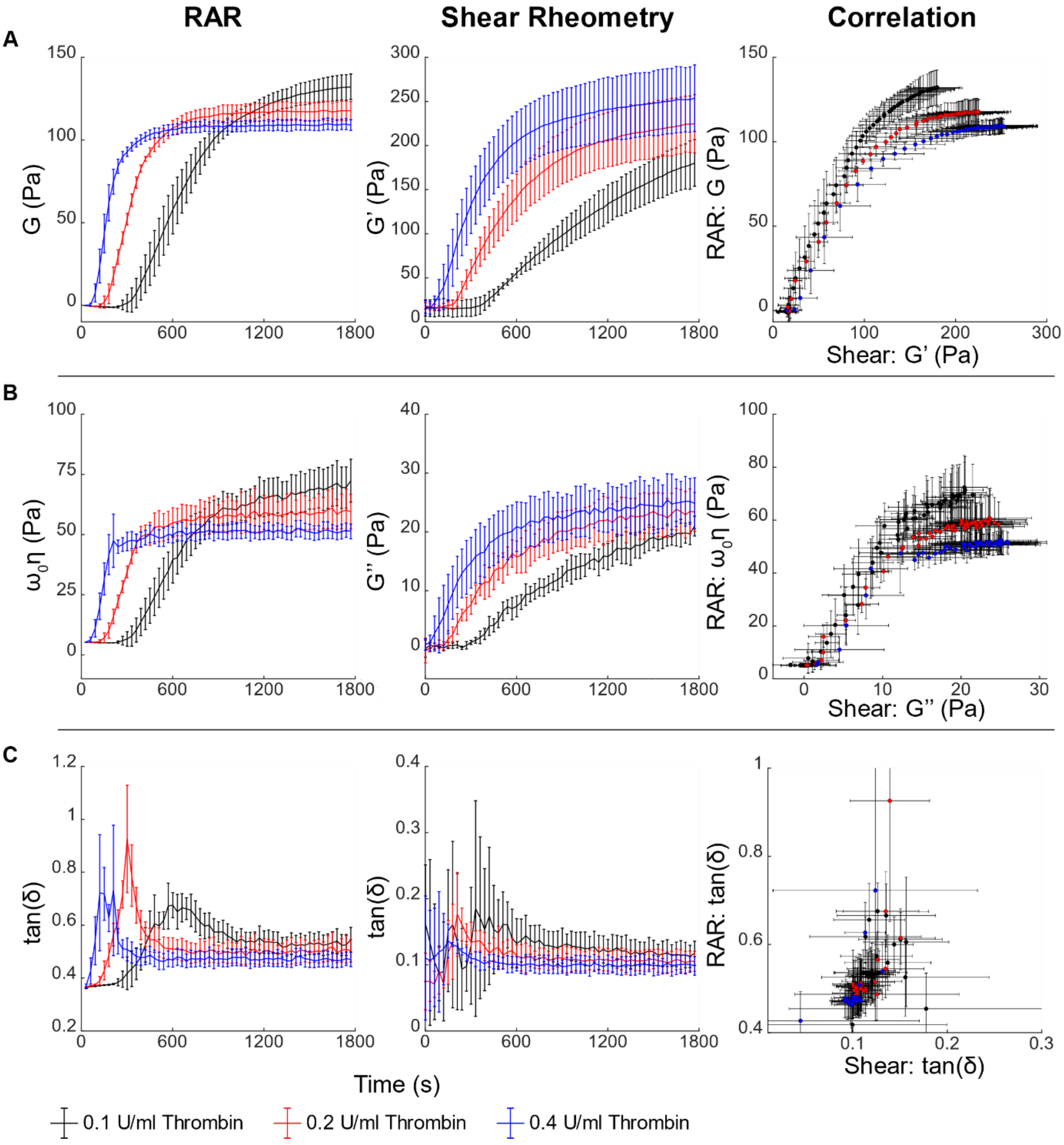

Figure 2.13: Dynamic RAR and shear rheometry measurements of the viscous and elastic properties during the gelation of 4 mg/ml fibrin with 0.1, 0.2, or 0.4 U/ml thrombin. A) Elastic parameters (G, G') and correlations. B) Viscous parameters ($\boldsymbol{\omega_0\eta}$, G'') and correlations. C) Loss factor (tan(δ)) and correlations. Error bars represent a 95% confidence interval (n=4). Error bars represent a 95% confidence interval (n ≥4).

formation of thicker fibrin fibrils with slower gelation kinetics [38,39]. The values of storage modulus measured by shear rheometry were generally higher than the corresponding RAR values. The results were correlated at low magnitudes, but diverged with increasing material stiffness, with the RAR measurements reaching a plateau more quickly than the corresponding shear rheometry data. The viscous modulus parameters over time (Fig. 2.13B) also exhibited a lag followed by an increasing phase and a plateau, with a similar thrombin concentration-dependent lag and plateau behavior as the elastic modulus parameters. The correlation between the viscous parameters shows that RAR values were consistently higher than shear rheometry data and reached their maximum more rapidly.

To provide a simple parameter to directly and quantitatively compare fibrin gelation kinetics, we defined two time constants related to the kinetics of elastic modulus (Fig. 2.14). T_0 was defined as the time at which the modulus reached 1/10th of the maximum value and T_1 was defined as the time at which the modulus reached 1/2 of the maximum value. The values of both T_0 and T_1 decreased significantly with increasing thrombin concentration, reflecting a faster

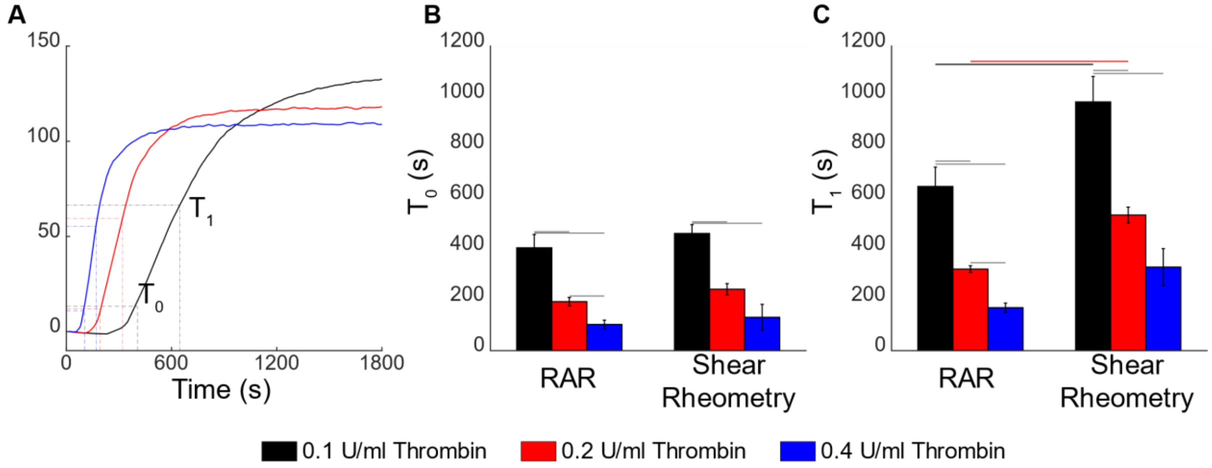

Figure 2.14: A) Schematic showing the definition of time constants, T0 and T1, used to quantify elastic dynamics in RAR (shown) and shear rheology. T0 and T1 are defined as the time at which G or G' reach 1/10th or ½, respectively, of their final value. Comparison of B) T0 and C) T1 values for dynamic RAR and shear rheology measurements of 4 mg/ml fibrin gelation with 0.1, 0.2, and 0.4 U/ml thrombin. T0 and T1 decreased significantly with increasing thrombin concentration for both techniques. No significant differences were observed between T0 values in RAR and shear rheology, but T1 values were significantly higher for shear rheology measurements. Error bars represent a 95% confidence interval (n ≥4). Lines above bars indicate significant differences according to a two-tailed students t-test with a Bonferroni correction ($p < 0.05$).

gelation rate. However, T_1 values from RAR were significantly lower than the corresponding shear rheometry measurements, possibly because the temperature of gelation could be more tightly controlled when using RAR.

The loss factor (Fig. 2.13C) for both RAR and shear rheometry exhibited a rapid initial rise to a peak value, followed by a decrease to a plateau level. The peak of the curve was much more evident in the RAR data, and corresponded to the peak in the damping coefficient, suggesting that RAR measurements provided a more sensitive marker for the sol-gel transition in these materials. The absolute values of the loss factor were consistently higher for RAR measurements. In all cases, the loss factor plateaued at a level between 0.1-0.5, suggesting a viscoelastic behavior that was not strongly dependent on thrombin concentration.

2.4 Summary and Conclusions

RAR has several potential advantages over other methods for the characterization of soft viscoelastic biomaterials. Its use of acoustic energy to deform and interrogate the sample allows non-contact measurement and avoids potential contamination. The generation and tracking of surface waves requires only low acoustic intensity and therefore prevents damage or permanent deformation of the sample. The well-established physics behind surface waves in liquids and hydrogels enables the extraction of intrinsic material properties from RAR measurements, independent of specific ultrasound parameters. Furthermore, the technique does not require an absorbing or scattering medium within the sample, and requires only small material volumes, thereby circumventing some of the limitations of other ultrasound-based techniques [40–42]. Conventional labware and ultrasound probes of a variety of sizes can be used, depending on the sample volume and structure, and the method can be automated for high throughput analysis. These features make the method well-suited for non-destructive, longitudinal tracking of biological samples over short (seconds) to long (weeks) time scales, which is particularly valuable for the types of biomaterials and constructs used in tissue engineering.

At the same time, RAR has several limitations. As a technique that measures the bulk mechanical properties and surface tension, RAR relies on resonant waves that are affected by the geometry of the sample and sample holder. Fortunately, conventional circular microplate wells are well-suited for the technique because of their infinite rotational symmetry. However, shape changes or inhomogeneities in the sample itself may affect the resonant wave modes to be excited. Based on FEA results, this study assumes a consistent *0,2* resonant mode across various samples, however changes to the surface or boundary condition of a sample could influence the dominant oscillatory modes and impact the accuracy of results. In addition, acute contact angles and/or the formation of a meniscus at the well wall may impact the resonant frequency and damping of surface waves [43], requiring the use of hydrophobic surface coatings. While dehydration of hydrogel samples with an air interface can lead to changes in both geometry and mechanics during studies of dynamic viscoelastic properties [33], the non-contact format of RAR allows for samples to be fully sealed, dramatically limiting evaporative effects compared to the exposed samples of many contact based methods. Sample thickness can also impact the resonant frequency of both pseudo-capillary and Rayleigh surface waves [40], though this effect can be reduced by using thicker samples.

In the present study, characterization of material properties using RAR was validated against both computational modeling and conventional shear rheometry. FEA confirmed that our approach applied the appropriate resonant modes and analytical models of surface waves. In general, the results from RAR and rotational shear rheometry correlated well for both end-point and dynamic measurements, though the results suggest that RAR may have advantages in more finely interrogating some material characteristics, particularly as related to gelation kinetics and phase transitions. Overall, RAR was shown to provide consistent, objective, and quantitative data that may enable new insights in the fields of biomaterials and tissue engineering, including improved fundamental understanding of material properties, as well as critical quality control in the translation of engineered tissue products.

2.5 References

[1] A.J. Engler, S. Sen, H.L. Sweeney, D.E. Discher, Matrix Elasticity Directs Stem Cell Lineage Specification, Cell. 126 (2006) 677–689. https://doi.org/10.1016/j.cell.2006.06.044.

[2] D.E. Discher, D.J. Mooney, P.W. Zandstra, Growth factors, matrices, and forces combine and control stem cells., Science (80-.). 324 (2009) 1673–7. https://doi.org/10.1126/science.1171643.

[3] M.P. Lutolf, J. a Hubbell, Synthetic biomaterials as instructive extracellular microenvironments for morphogenesis in tissue engineering., Nat. Biotechnol. 23 (2005) 47–55. https://doi.org/10.1038/nbt1055.

[4] O. Chaudhuri, L. Gu, D. Klumpers, M. Darnell, S.A. Bencherif, J.C. Weaver, N. Huebsch, H.P. Lee, E. Lippens, G.N. Duda, D.J. Mooney, Hydrogels with tunable stress relaxation regulate stem cell fate and activity, Nat. Mater. 15 (2016) 326–334. https://doi.org/10.1038/nmat4489.

[5] O. Chaudhuri, L. Gu, M. Darnell, D. Klumpers, S.A. Bencherif, J.C. Weaver, N. Huebsch, D.J. Mooney, Substrate stress relaxation regulates cell spreading, Nat. Commun. 6 (2015) 1–7. https://doi.org/10.1038/ncomms7365.

[6] M.L. Oyen, Mechanical characterisation of hydrogel materials, Int. Mater. Rev. 59 (2014) 44–59. https://doi.org/10.1179/1743280413Y.0000000022.

[7] V. Normand, D.L. Lootens, E. Amici, K.P. Plucknett, P. Aymard, New insight into agarose gel mechanical properties, Biomacromolecules. 1 (2000) 730–738. https://doi.org/10.1021/bm005583j.

[8] R.S. Lakes, Viscoelastic measurement techniques, Rev. Sci. Instrum. 75 (2004) 797–810. https://doi.org/10.1063/1.1651639.

[9] J.M. Walker, A.M. Myers, M.D. Schluchter, V.M. Goldberg, A.I. Caplan, J.A. Berilla, J.M. Mansour, J.F. Welter, Nondestructive evaluation of hydrogel mechanical properties using ultrasound, Ann. Biomed. Eng. 39 (2011) 2521–2530. https://doi.org/10.1007/s10439-011-0351-0.

[10] K.H. Vining, D.J. Mooney, Mechanical forces direct stem cell behaviour in development and regeneration, Nat. Rev. Mol. Cell Biol. (2017). https://doi.org/10.1038/nrm.2017.108.

[11] B.A. Juliar, J.A. Beamish, M.E. Busch, D.S. Cleveland, L. Nimmagadda, A.J. Putnam, Cell-mediated matrix stiffening accompanies capillary morphogenesis in ultra-soft amorphous hydrogels, Biomaterials. 230 (2020). https://doi.org/10.1016/j.biomaterials.2019.119634.

[12] K. Nightingale, Acoustic Radiation Force Impulse (ARFI) Imaging: a Review, Curr. Med. Imaging Rev. 7 (2012) 328–339. https://doi.org/10.2174/157340511798038657.Acoustic.

[13] D. Dalecki, K.P. Mercado, D.C. Hocking, Quantitative Ultrasound for Nondestructive Characterization of Engineered Tissues and Biomaterials, Ann. Biomed. Eng. 44 (2016) 636–648. https://doi.org/10.1007/s10439-015-1515-0.

[14] J.E. Brandenburg, S.F. Eby, P. Song, H. Zhao, J.S. Brault, S. Chen, K.N. An, Ultrasound elastography: The new frontier in direct measurement of muscle stiffness, Arch. Phys. Med. Rehabil. 95 (2014) 2207–2219. https://doi.org/10.1016/j.apmr.2014.07.007.

[15] X. Hong, R.T. Annamalai, T. Kemerer, C.X. Deng, J.P. Stegemann, Multimode ultrasound viscoelastography for three-dimensional interrogation of microscale mechanical properties in heterogeneous biomaterials, Biomaterials. 178 (2018) e1–e2. https://doi.org/10.1016/j.biomaterials.2018.05.057.

[16] M.R. Selzo, C.M. Gallippi, Viscoelastic response (VisR) imaging for assessment of viscoelasticity in voigt materials, IEEE Trans. Ultrason. Ferroelectr. Freq. Control. 60 (2013) 2488–2500. https://doi.org/10.1109/TUFFC.2013.2848.

[17] F.W. Mauldin, M.A. Haider, E.G. Loboa, R.H. Behler, L.E. Euliss, T.W. Pfeiler, C.M. Gallippi, Monitored steady-state excitation and recovery (MSSER) radiation force imaging using viscoelastic models, IEEE Trans. Ultrason. Ferroelectr. Freq. Control. 55 (2008) 1597–1610. https://doi.org/10.1109/TUFFC.2008.836.

[18] F. Viola, M.D. Kramer, M.B. Lawrence, J.P. Oberhauser, W.F. Walker, Sonorheometry: A noncontact method for the dynamic assessment of thrombosis, Ann. Biomed. Eng. 32 (2004) 696–705. https://doi.org/10.1023/B:ABME.0000030235.72255.df.

[19] K.P. Mercado, J. Langdon, M. Helguera, S.A. McAleavey, D.C. Hocking, D. Dalecki, Scholte wave generation during single tracking location shear wave elasticity imaging of engineered tissues, J. Acoust. Soc. Am. 138 (2015) EL138–EL144. https://doi.org/10.1121/1.4927633.

[20] P.-L. Kuo, C.-C. Charng, P.-C. Wu, P.-C. Li, Shear-wave elasticity measurements of three-dimensional cell cultures for mechanobiology, J. Cell Sci. 130 (2017) 292–302. https://doi.org/10.1242/jcs.186320.

[21] P.Y. Chao, W.W. Liu, S.F. You, P.C. Li, Shear Wave Elasticity Measurements of Three-Dimensional Cancer Cell Cultures Using Laser Speckle Contrast Imaging, Sci. Rep. 8 (2018) 1–10. https://doi.org/10.1038/s41598-018-32763-x.

[22] A.H. Henni, C. Schmitt, G. Cloutier, Shear wave induced resonance: A new excitation mode for dynamic elastography imaging, Proc. - IEEE Ultrason. Symp. (2008) 221–224. https://doi.org/10.1109/ULTSYM.2008.0054.

[23] F.S. Corey, W.F. Walker, Sonic Estimation of Elasticity via Resonance: A New Method of Assessing Hemostasis, Ann. Biomed. Eng. 44 (2016) 1405–1424. https://doi.org/10.1007/s10439-015-1460-y.

[24] M. Bhatt, E. Montagnon, F. Destrempes, B. Chayer, S. Kazemirad, G. Cloutier, Acoustic radiation force induced resonance elastography of coagulating blood: Theoretical viscoelasticity modeling and ex vivo experimentation, Phys. Med. Biol. 63 (2018). https://doi.org/10.1088/1361-6560/aab46a.

[25] M. Forbush, H. Chow, J. Chiao, A. Rose, Noninvasive Fluid Property Measurements Using Acoustic Methods, Clin. Lab. Med. 27 (2007) 61–73. https://doi.org/10.1016/j.cll.2006.12.002.

[26] J.W. Miles, Resonantly forced surface waves in a circular cylinder, J. Fluid Mech. 149 (1984) 15–31. https://doi.org/10.1017/S0022112084002512.

[27] F.E. Borgnis, Acoustic radiation pressure of plane compressional waves, Rev. Mod. Phys. 25 (1953) 653–664. https://doi.org/10.1103/RevModPhys.25.653.

[28] B.H. Cao, M.W. Kim, H. Schaffer, H.Z. Cummins, Surface modes on polymer solutions by surface light-scattering techniques, J. Chem. Phys. 95 (1991) 9375. https://doi.org/10.1063/1.464543.

[29] H. Takahashi, P.-K. Choi, Sol – Gel Transition in Gelatin Observed with Surface Waves, Jpn. J. Appl. Phys. 35 (1996) 2939–2943.

[30] F. Monroy, Surface hydrodynamics of viscoelastic fluids and soft solids: Surfing bulk rheology on capillary and Rayleigh waves, Adv. Colloid Interface Sci. 247 (2017) 4–22. https://doi.org/10.1016/j.cis.2017.07.006.

[31] Y. Onodera, P.-K. Choi, Surface-wave modes on soft gels, J. Acoust. Soc. Am. 104 (1998) 3358–3363. https://doi.org/10.1121/1.423919.

[32] B.H. Cao, M.W. Kim, H.Z. Cummins, Surface waves on polymer solutions: Complete capillary wave-elastic wave crossover, J. Chem. Phys. 102 (1995) 9375–9379. https://doi.org/10.1063/1.468805.

[33] R.H. Ewoldt, M.T. Johnston, L.M. Caretta, Experimental Challenges of Shear Rheology: How to Avoid Bad Data, in: S.E. Spagnolie (Ed.), Complex Fluids Biol. Syst. Exp. Theory, Comput., Springer New York, New York, NY, 2015: pp. 207–241. https://doi.org/10.1007/978-1-4939-2065-5_6.

[34] S. Kazemirad, S. Bernard, S. Hybois, A. Tang, G. Cloutier, Ultrasound Shear Wave Viscoelastography: Model-Independent Quantification of the Complex Shear Modulus,

IEEE Trans. Ultrason. Ferroelectr. Freq. Control. 63 (2016) 1399–1408. https://doi.org/10.1109/TUFFC.2016.2583785.

[35] S.S. Yengul, P.E. Barbone, B. Madore, Dispersion in Tissue-Mimicking Gels Measured with Shear Wave Elastography and Torsional Vibration Rheometry, Ultrasound Med. Biol. 45 (2019) 586–604. https://doi.org/10.1016/j.ultrasmedbio.2018.07.002.

[36] P.A. Janmey, J.P. Winer, J.W. Weisel, Fibrin gels and their clinical and bioengineering applications, J. R. Soc. Interface. 6 (2009) 1–10. https://doi.org/10.1098/rsif.2008.0327.

[37] R. Kita, A. Takahashi, M. Kaibara, K. Kubota, Formation of fibrin gel in fibrinogen-thrombin system: Static and dynamic light scattering study, Biomacromolecules. 3 (2002) 1013–1020. https://doi.org/10.1021/bm025545v.

[38] S.L. Rowe, S.Y. Lee, J.P. Stegemann, Influence of thrombin concentration on the mechanical and morphological properties of cell-seeded fibrin hydrogels, Acta Biomater. 3 (2007) 59–67. https://doi.org/10.1016/j.actbio.2006.08.006.

[39] A.S. Wolberg, Thrombin generation and fibrin clot structure, Blood Rev. 21 (2007) 131–142. https://doi.org/10.1016/j.blre.2006.11.001.

[40] A. Keunho, K.H. Yoon, M.W. Kim, Thickness dependence of surface modes on a gel, Europhys. Lett. 54 (2001) 199–205. https://doi.org/10.1209/epl/i2001-00295-7.

[41] J. Brum, S. Catheline, N. Benech, C. Negreira, Shear elasticity estimation from surface wave: The time reversal approach, J. Acoust. Soc. Am. 124 (2009) 3377–3380. https://doi.org/10.1121/1.2998769.

[42] F. Monroy, D. Langevin, Direct experimental observation of the crossover from capillary to elastic surface waves on soft gels, Phys. Rev. Lett. 81 (1998) 3167–3170. https://doi.org/10.1103/PhysRevLett.81.3167.

[43] R. Kidambi, Meniscus effects on the frequency and damping of capillary-gravity waves in a brimful circular cylinder, Wave Motion. 46 (2009) 144–154. https://doi.org/10.1016/j.wavemoti.2008.10.001.

Chapter 3 Elastocapillary Transition during Formation of Viscoelastic Gels

3.1 Introduction

Mechanical testing of hydrogels can be particularly challenging due to their relatively low elastic modulus, viscoelastic nature, and biphasic structure [1]. Techniques such as shear rheometry and nano-indentation have been used to measure mechanical properties of hydrogels. However, these common approaches typically require direct contact with the samples, thus are limited to mostly end-point measurements due to the risk of sample contamination and damage. As biomaterials, such as hydrogels, often exhibit continuous changes due to factors such as swelling, enzymatic degradation or crosslinking, and cell-mediated remodeling in cellular constructs, techniques capable of longitudinal tracking of materials are needed to monitor changes over time in a non-contact fashion.

Unlike stiff materials for which elasticity dominates, the behavior of soft solids is affected by both surface tension and elastic properties [2]. The unique elastocapillary nature of soft solids has important implications in many applications and fields including surgery, tissue engineering, and flexible electronics [3]. Approaches to study the surface hydrodynamics of viscoelastic fluids and soft solids have provided a unique strategy to investigate the rheology of these materials [4]. In addition, growing interest in bioprinting technologies for generating tissues and organs [5] has further underscored the need for examination of the surface hydrodynamics of soft materials [4,6]. Traditionally, studies of surface waves have relied on measuring the phase velocity of travelling waves and wavenumber/frequency to determine the dispersion relation [4]. Direct mechanical or electrical means are typically used to generate surface waves and detection of the surface movements is achieved using light scattering techniques. Furthermore, as measurements at multiple spatial locations are needed to determine phase velocity and wavenumber, these techniques require a relatively large surface area and volume of material for the experiments, thus are not suitable for biomaterial samples in tissue engineering applications.

As an important characteristics of soft materials, capillary to elastic wave crossover was predicted by the HPP theory [4,7], and experimental observation of the unique phenomenon has been the focus of a number of studies [8–10].Conventional studies of the elastocapillarity relied on measurements obtained from different static polymer solutions each prepared with different polymer concentration to achieve varied viscosity and elasticity [9,10].

In this study, we demonstrate the application of a dual-mode acoustic technique for non-contact mechanical characterization of viscoelastic liquids and soft solids. The technique, named resonant acoustic rheometry (RAR), uses synchronized ultrasound pulses to generate and detect the resonant modes of surface waves on a sample material [11]. We report results of the changing material property as fibrin gels are formed using thrombin and polyethylene glycol-norbornene (PEG-NB) is crosslinked using UV light, identifying consistent phenomena during gelation regardless of whether a material is natural or synthetic. We then applied these findings to identifying the gel point in coagulin gels, improving upon the traditional gel clot LAL assay and enabling quantitative endotoxin quantification.

3.2 Materials and Methods:

3.2.1 Experimental Setup

As previously described, the experimental setup (Fig. 3.1A) for RAR consisted of an ultrasound transducer mounted to a 3D motion platform (Velmex) and submerged a temperature-controlled water tank. The transducer was directed upwards at the bottom of a microplate affixed

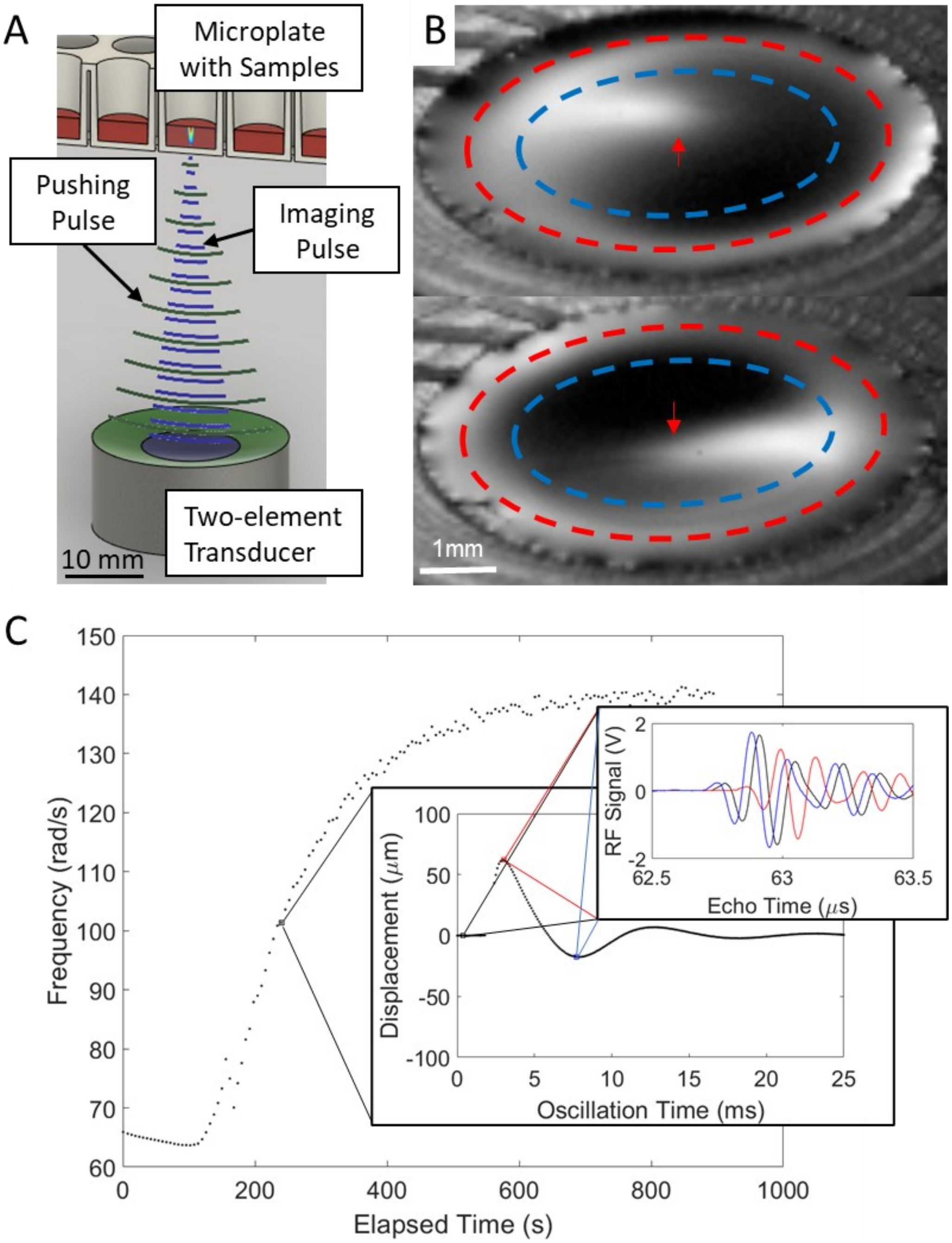

Figure 3.1 A) Schematic diagram of the RAR experimental system with a focused ultrasound transducer aligned beneath a microplate for generating measurements through the sealed plate bottom. B) Images of oscillating fibrin surface taken using high-speed camera with elevated center (above) and depressed center (below). Oscillatory node indicated by dashed blue line and antinodes indicated by red dashed line and red arrow. C) Depiction of the multiple time scales involved in RAR measurements, with individual A-lines used to calculate displacement during a single oscillatory measurement that is then repeated over the course of an extended study.

just below the water surface using a custom microplate holder. The custom transducer was made up of two concentric, cofocused elements aimed at the center of the top surface of the sample. The outer transducer (center frequency 1.5 MHz, -3dB beam width 1 mm, focal length 48 mm), was driven by an arbitrary waveform generator (33220A; Agilent) and a power amplifier (75A250; Amplifier Research) to apply a short ultrasound pulse (duration 33 µs, acoustic pressure 3.0 MPa) and induce a focal surface perturbation due to the acoustic radiation force (ARF) [12]. The inner transducer (center frequency 7 MHz, -3 dB beam width 0.5 mm, focal length 48 mm) was driven by a pulser receiver (PR5900, Panametric) for pulse-echo tracking of the sample surface. The backscattered RF signals were digitized at 250 MSamples/s using a digital oscilloscope (Fibrin and PEG: 5443D, Picoscope; Blood and LAL: 54830B; Agilent) and saved for offline analysis. Standard RAR measurements consisted of a single ARF pulse to generate surface deformation and a series of pulse-echoes performed at a PRF of 5-10 kHz. Dynamic viscoelastic monitoring was performed by repeating individual RAR measurements at regular time intervals.

3.2.2 Surface Wave Detection:

Surface wave displacement was measured as described previously [11], utilizing the inner transducer in pulse-echo mode. The echo time of the backscattered signals, $t_e = \frac{2l}{c}$, where l is the path length from the transducer to sample surface which is the time needed for the ultrasound pulse to travel from a reference location to and back from a scatterer, reflects its spatial location relative to the reference location, with a sound speed, *c*. The temporal shift of the surface echo, Δt_e, following excitation is measured using a normalized cross-correlation with the baseline echo. The displacement of the sample surface, *x*, is then obtained from the temporal shift of the echo signal from the surface relative to its equilibrium position, according to $x = \frac{c\Delta t_e}{2}$. This is repeated for each echo captured during RAR, allowing for calculating the dynamic surface oscillations (Fig. 3.1C).

3.2.3 Rapid RAR (rRAR)

The minimum time interval to perform a single RAR measurement, save the RF data, and reset the instruments for the next measurement was approximately 1 second. To perform measurements of rapid dynamics, we developed an alternative measurement protocol, rapid RAR (rRAR) where excitation pulses were issued repeatedly while continuously sampling the surface using pulse-echo. This allowed for the RAR measurements to be performed at a sampling rate of 5 Hz for up to a 10 second duration (limited by oscilloscope memory depth). The measured displacements for each excitation pulse could then be separated into individual segments and used to calculate displacement time series data as above.

3.2.4 Resonant Parameter Extraction

The resonant modes of surface waves are determined by the boundary conditions at the well wall. Assuming axis symmetry, a fixed boundary condition at the wall of cylindrical well requires,

$$J_0(ka) = 0, \tag{1}$$

where J_0 is the Bessel function of zero-th order, k the wavenumber, and a the radius of the well. For the 96-well microplates (Nunc) used in the majority in this study, $a = 3.25\ mm$. Equation (1) yields discrete wavenumber k_m,

$$k_m a = \alpha_m, m = 1, 2, \ldots \tag{3}$$

where α_m is the m-th root of the zero-th order Bessel function and For example, $\alpha_1 = 2.40$, $\alpha_2 = 5.52$ and $\alpha_3 = 8.65$, for the (0,1), (0,2) and (0,3) mode respectively, resulting in wavenumbers $k_1 = 0.774\ mm^{-1}$, $k_2 = 1.78\ mm^{-1}$, and $k_3 = 2.79\ mm^{-1}$. The resonant frequencies of the surface oscillation are determined by the dispersion relation of the specific surface wave, $\omega_{m0} = \Omega(k_m)$ which depends on material properties such as surface tension and elastic modulus [7,13].The surface movement at the center of the circular surface of the sample is then the summation of a series of resonant modes of surface wave which can each be described as damped harmonic oscillators,

$$x(t) = A_0 e^{-\Gamma t} \cos{(\omega_1 t + \phi)} \,, \tag{3}$$

where t is the oscillation time of the kinetic surface movement following the initial perturbation. A_0, Γ , and ϕ are the amplitude, damping coefficient, and phase shift, respectively. The natural frequency of the surface wave from the dispersion relation, $\omega_0 = \Omega(k)$ is calculated from the damped frequency, ω_1, and the damping coefficient, Γ,

$$\omega_0 = \sqrt{{\omega_1}^2 + \Gamma^2}, \tag{4}$$

The resonant frequency and damping coefficient were calculated from RAR data as described previously [11], utilizing the findpeaksL function (https://terpconnect.umd.edu/~toh/spectrum/PeakFindingandMeasurement.html) for MATLAB to find the position and half-width at half-maximum (HWHM) of Lorentzian peaks in power spectra generated from the time-series displacements. The frequency positions of the fitted peaks are subsequently defined as the damped frequency, ω_1. An exponential decay weighting function,

$$W = e^{-Rt}, \tag{5}$$

with $R = 20$ was applied to broaden narrow peaks to reduce high-frequency noise and spectral ringing from the DFT. This broadening of the peaks could be easily corrected by combining equations 3 and 5,

$$x(t) = A_0 e^{-\Gamma t} \cos(\omega_1 t + \phi)\, e^{-Rt} = A_0 e^{-(\Gamma + R)t} \cos(\omega_1 t + \phi), \tag{6}$$

it is possible to calculate the unfiltered damping as $\Gamma = HWHM - R$.

To better identify the spectral components during Fibrin gelation, we also employed a hamming window during the discrete Fourier transform to narrow the linewidth. The use of a hamming window did not alter the extracted damped frequency when compared to a rectangular window or exponential decay weighting function (Fig. 3.2A) but did alter the $HWHM$ substantially (Fig. 3.2B). The use of a weighting function to broaden the spectral lines did also shift the $HWHM$, but could be corrected as described above (Fig. 3.2C) and enabled the more accurate measurement of narrow peaks which is crucial to accurate measurements of viscosity in minimally damped materials.

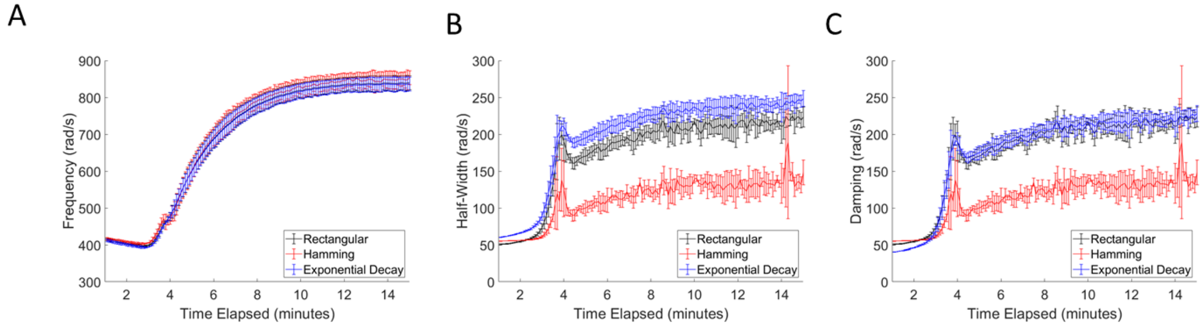

Figure 3.2: Dynamic RAR measurements of A) natural frequency, B) half-width half-max (HWHM), and C) damping coefficient extracted during gelation of 8.0 mg/ml fibrin gels. Parameters were extracted from FFTs produced with rectangular, hamming, and exponential decay windows show. Error bars represent standard deviation (n=4).

3.2.5 Hydrodynamic models of viscoelastic surface waves

Hydrodynamic models were applied to calculate the elastic and viscous properties of hydrogels from extracted RAR resonant parameters. Three distinct models were applied for capillary, pseudocapillary, and Rayleigh waves.

Capillary waves are the dominant mode of surface wave for liquids that do not have an elastic component and are driven by surface tension [4]. In liquid-like regimes and low viscosity, the real part of the angular frequency Ω can be approximated by the Kelvin frequency,

$$\omega_c{}^2 = \frac{\sigma k^3}{\rho}, \qquad [7]$$

where k is the wavenumber and σ the surface tension. Since hydrogels have a density close to water, we used $\rho = 1000\,\frac{kg}{m^3}$ for all materials. The damping coefficient of a capillary wave is given by,

$$\Gamma = \frac{2\eta k^2}{\rho}, \tag{8}$$

where η is the viscosity of the material.

Pseudo-capillary waves are present on viscoelastic liquids, where both surface tension and elasticity may act to drive surface waves as a restoring force. The dispersion relation includes both restoring forces [13]

$$\omega_{pc}{}^2 = \frac{\sigma k^3}{\rho} + 4\frac{Gk^2}{\rho}. \tag{9}$$

Rayleigh waves are the dominant mode of surface waves propagating on solid hydrogels, where elasticity dominates over surface tension or gravity. However, in the case of soft solids with high surface tension, such as a hydrogel, the surface tension cannot be completely ignored. In this case the dispersion relation is slightly modified from Equation 9 to represent the solid, Rayleigh, waves driven by both elasticity and surface tension

$$\omega_r{}^2 = \frac{\sigma k^3}{\rho} + \frac{\beta G k^2}{\rho}, \tag{10}$$

where ρ is the material density, k the wavenumber, and β (0.91 in this study) a Rayleigh/shear wave proportionality [14]. The damping coefficient of Rayleigh surface waves [4] is determined as

$$\Gamma = \frac{0.45\eta k^2}{\rho}, \qquad (11)$$

3.2.6 Hydrogel Stock Preparations

Fibrinogen stock solutions of 4.0 and 8.0 mg/ml (clottable) were prepared by dissolving lyophilized bovine fibrinogen (F8630, Sigma) in phosphate buffered saline (PBS; Gibco) at 37°C. The fibrinogen solutions were filtered using a 0.2 um PVDF syringe filter. Bovine thrombin (T6634; Sigma) was dissolved in a sterile-filtered solution of 0.1 %w/v bovine serum albumin (Sigma) in DI water to form a 50 Unit/ml stock solution. A 150 mg/ml stock solution was prepared of 20 kDa 4-arm PEG norbornene (PEG-NB) in PBS. A 35mM solution of a dithiol crosslinker with a PEG spacer (PEG-DT) was prepared in PBS. Lithium phenyl-2,4,6-trimethylbenzoylphosphinate (LAP) was prepared in PBS at a 5mM stock concentration. LAL reagent and endotoxin standards (Lonza) were prepared in Endotoxin-free water (EF-H_2O) as directed by the manufacture.

3.2.7 Fibrin Gelation Experiments

Fibrin gelation was initiated by adding thrombin to the fibrinogen solutions at a final concentration of 0.4 Unit/ml. The solution was thoroughly mixed and then 100 ul was pipetted into a Syl-Off (Q2-7785, Dow) coated microplate (269620, Nunc) while positioned above a 37C water bath. An adhesive plate seal (, Fisher) was applied to minimize evaporation. RAR measurements were initiated exactly 60 seconds after the addition of thrombin and were repeated at 20 second intervals for a total 15 minute duration.

3.2.8 Porcine Blood Coagulation:

Venous porcine blood was collected into vacutainers containing sodium citrate. Coagulation was initiated by combining 20 µl 0.2M $CaCl_2$ with 340 µl of citrated blood and 100 µl was immediately added to a 96-well microplate (655801, Greiner) on the 37C water tank. RAR measurements were initiated 60 seconds after the combination of recalcification of blood and were repeated at 120 second intervals for the duration of a 90 minute study.

3.2.9 PEG UV Crosslinking

PEG precursor solutions were prepared by combining the PEG-NB, PEG-DT and LAP stock solutions in PBS. PEG-NB concentrations of 30, 50, and 100 mg/ml (1.5, 3 and 5 mM) required respective PEG-DT concentrations of 3, 5, and 10 mM for 100% crosslinking of the 4-arm PEG. LAP was added at final concentrations of 0.5, 1, and 2 mM to alter the rate of free-radical generation. After mixing, 100uL PEG precursor solutions were added to a Syl-Off coated 96-well microplate (269620, Nunc). An initial RAR measurement of the precursor solution was initiated immediately after plating. Exactly 5 seconds later, a 3W 365 nm UV LED positioned 5mm above the microplate well (light intensity of 40 mW/cm^2 at the sample surface) was triggered for a 60 second duration. For 10 seconds following the initiation of UV crosslinking, rRAR measurements were performed with a 200 ms sampling interval. Following the rRAR measurements, standard RAR measurements were performed at 5 second intervals for remainder of the 60 second UV illumination.

3.2.10 Dynamic LAL Measurements

Endotoxin containing samples were generated by diluting the 10 EU/ml Endotoxin stock solution to 1 EU/ml and performing a 2-fold dilution series from 0.5 EU/ml to 0.002 EU/ml in EF-H_2O, Dulbelcco's Modified Eagle Medium (DMEM) or DMEM supplemented with 10% FBS (D10). LAL reagent and endotoxin samples were combined at a 1:1 ratio and 100 µl was added to each well 96-well microplate (Wako) at 37C. RAR measurements were initiated 60 seconds after the combination of reagents and were performed at 180 second intervals for the duration of a 2 hour study.

3.2.11 Statistical analysis

All data is presented as mean ± standard deviation. Significant differences between fitted parameters were determined using a Student's two-tailed t-test with $\alpha = 0.05$.

3.3 Results and Discussion

3.3.1 Visualization of surface waves:

High-speed video of liquid surfaces during RAR measurements was collected to verify the dominant oscillatory modes on the surface of liquid and solid fibrin samples. Still images at time points 180° out of phase with one another (Fig. 3.1B) show a radially symmetric oscillation with concentric circular nodes at the sample edge and roughly halfway between the center and edge, denoted by blue circles. Antinodes are present at the point directly in the center of the circular sample surface and as a concentric ring between the two nodes, denoted by a red arrow and circle. This is consistent with the predicted 0,2 mode of radially symmetric oscillation used in a previous study [11].

3.3.2 Thrombin induced gelation of fibrin:

We applied RAR to generate and detect resonant surface oscillations on freshly prepared fibrinogen and thrombin samples every 6s consecutively for 15 min, at which time a stable fibrin gel was formed. We tracked the oscillatory displacement at each sampling time point, observing an exponentially decaying sinusoid that could be modeled as a damped harmonic oscillator (Fig. 3.3A). To quantify the resonant parameters from the measured displacements, we calculated the power spectrum (Fig. 3.3B) and found the position and width of the main peak. The temporal changes in the individual displacement time-series during the formation of an 8 mg/ml fibrin gel were visualized using a 2D color encoded heat map (Fig. 3.3C). The color indicates the normalized displacement at the sample center for each time-series following the initial push of each individual displacement measurement (vertical axis) and as a function of the elapsed time since the initiation of gelation when RAR measurement was applied (horizontal axis). The transition from a liquid fibrinogen solution to a solid fibrin gel can be seen in the changes to the duration and spacing of the measured oscillations. We also generated heatmap of the evolving power spectrum (Fig. 3.3D) for 4 and 8 mg/ml fibrin gels in both 48 and 96 well microplate geometries.

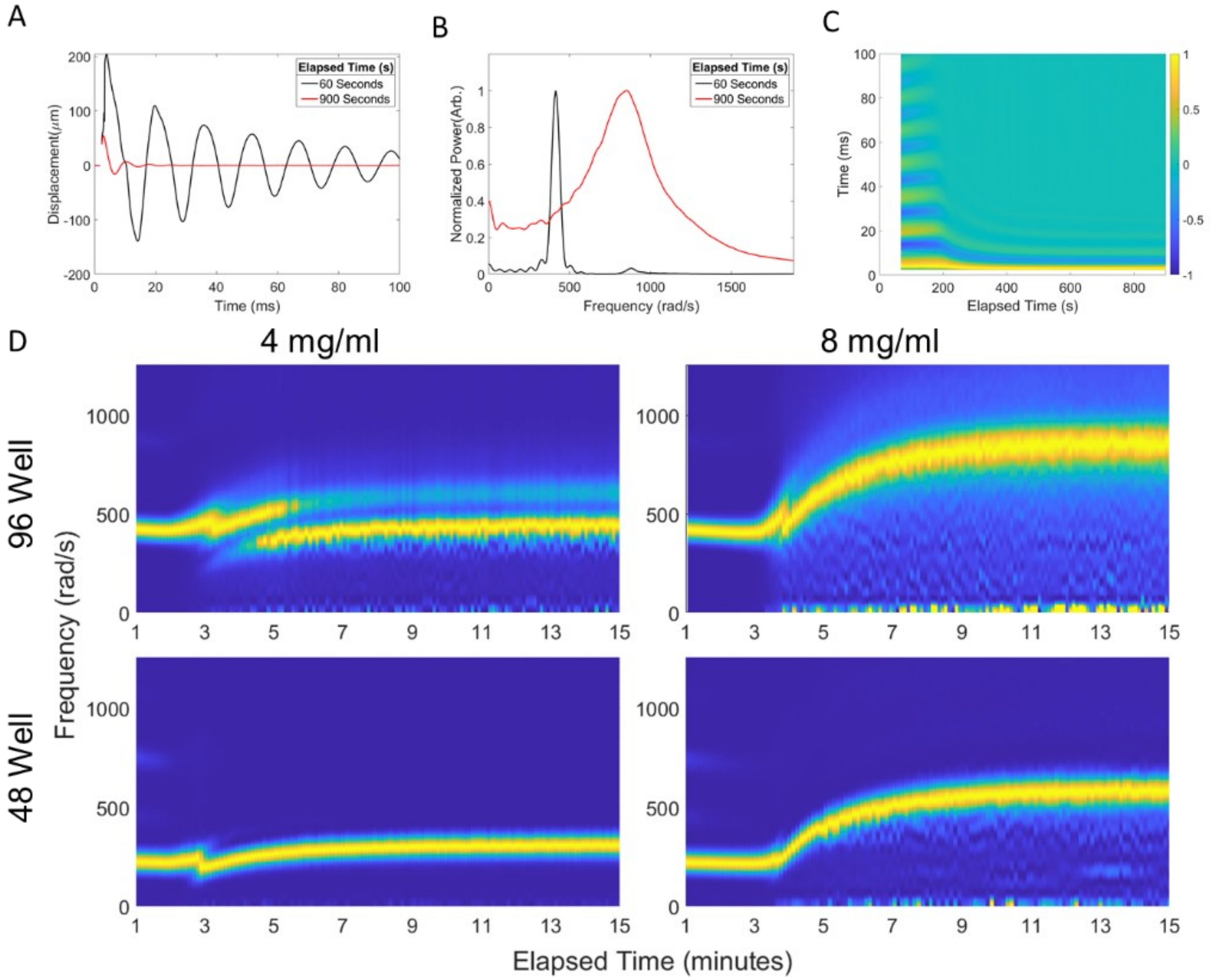

Figure 3.3: A) Surface displacement versus time and B) Power spectra for 8 mg/ml fibrin measured before (black) and after (red) gelation. C) Heatmap showing normalized displacement (color) as a function of oscillation time (vertical axis) and elapsed time since thrombin addition (horizontal axis). D) Heatmaps of changing power spectra for 4 and 8 mg/ml fibrin gels cast into 96 and 48 well plates**.** Color indicates the normalized power over the frequency spectrum (vertical axis) as a function of the elapsed time since the initiation of gelation (horizontal axis).

The color indicates the normalized power over the frequency spectrum (vertical axis) as a function of the elapsed time since the initiation of gelation (horizontal axis). The heat map reveals the temporal evolution of the frequency components of resonant surface oscillation during fibrin gel formation. There are noticeable differences in the spectral heatmaps for each of the fibrin gels and geometries tested. The temporal changes to frequency appear to be smooth and continuous, except approximately 3 to 4 minutes after the addition of thrombin, when there is a brief discontinuity. A combined plot was generated showing frequency (extracted using a hamming window) and damping (extracted using a weighting function with R = 20) is shown in Figure 3.4A.

A four-stage process was observed in the temporal changes, including capillary, pseudocapillary, and Rayleigh waves with a discontinuous transition between periods of dominant pseudocapillary and Rayleigh oscillations. We will subsequently describe in detail the temporal evolution of an 8 mg/ml fibrin gel in a 96 well plate as it goes through these stages.

3.3.3 Capillary wave behavior

From the very beginning of the experiment shortly after addition of thrombin, T_0, and until about $T = T_1 = \sim 180$ s, a dominant mode of surface wave was detected in the sample with an angular frequency of approximately 400 rad/s (Fig. 3.4A). Since the sample was known to be in the liquid phase initially, the surface waves were expected to be capillary waves driven primarily by the surface tension, σ, of the liquid sample with negligible elastic component. Using Equations 7 and 8 and the observed (0, 2) mode, the surface tension and viscosity of the sample were determined to be 36.4 ± 0.6 mN·m and 6.90 ± 0.05 mPa·s when calculated, respectively, from the measured resonant angular frequency, 418 ± 3 rad/s, and damping coefficient, 40.4 ± 0.3 rad/s. During this stage, both the resonant frequency and damping coefficient exhibited little change, suggesting a constant surface tension and viscosity in the sample.

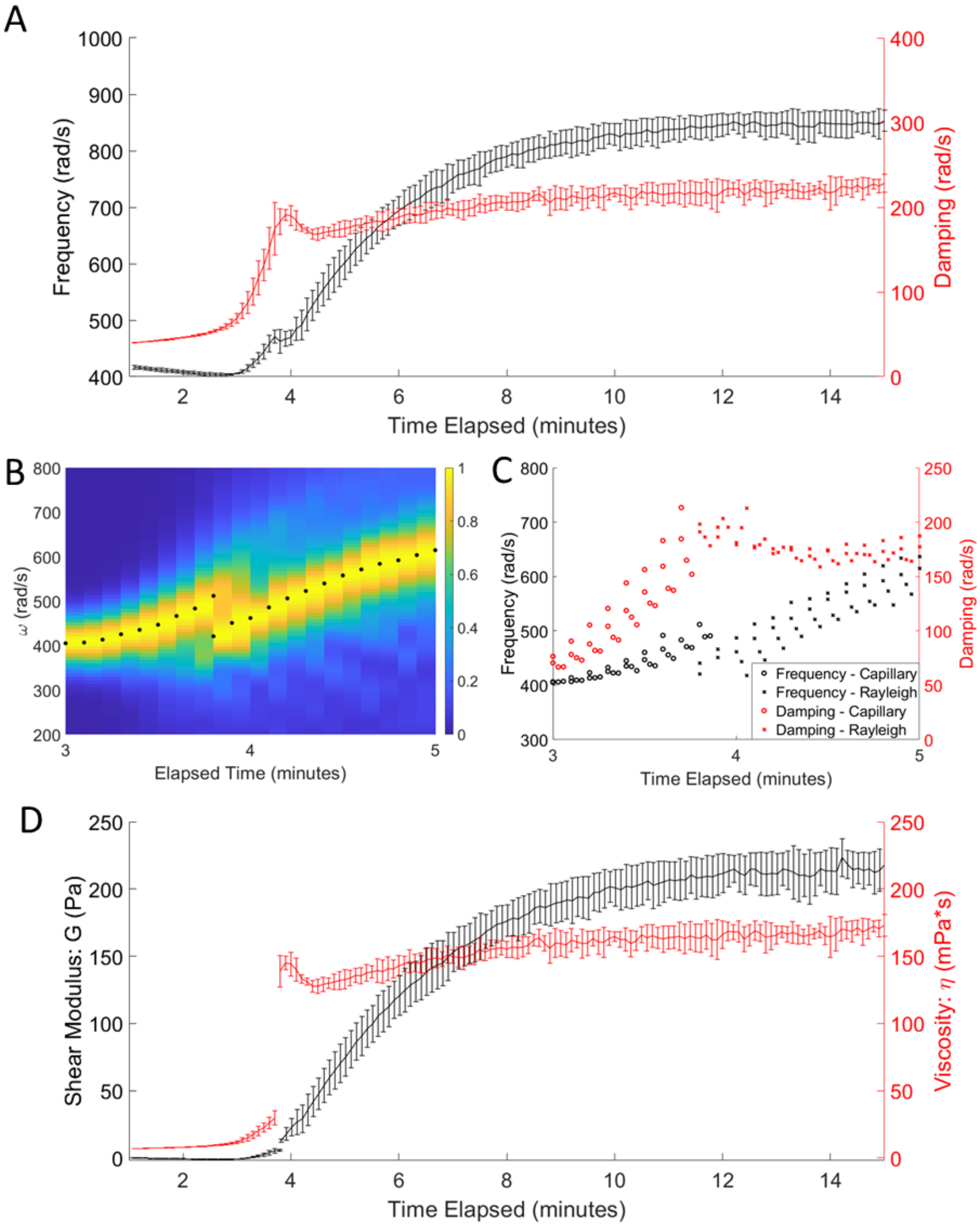

Figure 3.4: Dynamic RAR measurements from the gelation of 8.0 mg/ml fibrin gels in a 96-well plate. A) Natural frequency (left axis) and damping coefficient (right axis) measured over time following the addition of 0.1 U/ml thrombin. B) Close-up view of the power spectrum heatmap at the crossover with black dots indicating fitted peaks. C) Individual natural frequency (left axis) and damping coefficient (right axis) measurements near the crossover point. D) Combined shear modulus (G) and viscosity (***η***) measured over the entire gelation. Error bars represent standard deviation (n=4).

3.3.4 Pseudocapillary elastic increase

During the next stage ($T = T_1 - T_2 = 180$ - 220 s), the resonant frequency increased, along with a rapid increase in damping coefficient suggesting that the sample was becoming more viscous and exhibiting viscoelastic behavior, as predicted by the HPP theory. Extended from the classical Landau-Levich description of surface waves, the HPP theory of the hydrodynamics of viscoelastic fluids includes the impact of elastic component on the surface wave characteristics. The wavelength of the (0,2) resonant mode, $\frac{1}{k_2} \sim 0.6\ mm$ is comparable with the characteristic shear length $l_s = \frac{G_0}{\rho g} \sim 1\ mm$ for shear modulus $G_0 \sim 10$ Pa. Now with both surface tension and elasticity as restoring force, the surface waves in the sample are characterized as pseudocapillary waves with a dispersion relation defined in Equation 9. Using this equation, we determined the shear modulus of the sample at a given time *T* from the measured resonant frequency $\omega_{pc}(T)$ and ω_c measured at T_0 previously by assuming the surface tension remains constant during the gelation process.

3.3.5 Rayleigh progression

Interestingly, as the dominant angular frequency increased to a peak value around 4 minutes into gelation, a new frequency component appeared besides the pseudocapillary wave (Fig. 3.4A). For a short duration, the two distinct frequency components co-existed, as shown in the power spectrum (Fig. 3.4B), which coincides with a sharp peak in the damping coefficient at $T = Tc = 235$ s (Fig. 3.4C). These observations are consistent with the prediction and observation by Onodera and Choi [13,15] that pseudocapillary wave and Rayleigh waves can co-exist on soft gels in an elastocapillary crossover region [13]. Importantly, these changes suggest that the material was in the process of transforming from viscoelastic fluid to viscoelastic solid, and the increasing contribution of the elastic component of the restoring force resulted in the emergence of a Rayleigh wave, following the dispersion relations detailed in Equations 10 and 11. In the final stage, immediately after the crossover, the pseudocapillary wave disappeared while the Rayleigh wave became the dominant wave mode, accompanied by a sharp drop in the damping coefficient to a stable level (Fig. 3.4A), suggesting that the material had progressed into the solid-like regime. The measured frequency and damping coefficient of the (0, 2) mode at the end of gelation, 851 ± 20 rad/s and 219 ± 9 rad/s, were used to calculate the final shear modulus and viscosity to be 214 ± 14 Pa and 166 ± 7 mPa·s.

The dynamic shear modulus and viscosity was plotted (Fig. 3.4D) using a piecewise function with Equations (9) and (8) calculating the shear modulus and viscosity from pseudocapillary waves before the liquid-solid crossover and Equations (10) and (11) calculating the viscoelastic parameters from the Rayleigh wave afterwards. This approach eliminates the discontinuity seen the resonant frequency during gelation, reflecting the more likely continuous development of an elastic fibrin network with a monotonically increasing shear modulus.

However, this approach does not fully account for the local peak in damping coefficient. The difference in the hydrodynamic equations relating damping to viscosity for pseudopapillary and Rayleigh (Equations 8 and 11) account for some of the initial spike in damping. For a given material viscosity, the damping of pseudocapillary waves will be greater than that for Rayleigh waves. The transition between dominant oscillatory modes will therefore be accompanied by a resulting shift in damping. This transition is accounted for in the piecewise calculation of viscosity of time, but there is still a discontinuity and a local peak observed in Figure 3.4D, indicating transitional phenomena not accounted for in the current model. A similar phenomena has been observed in studies looking at the phase transition of hydrogels as a function of temperature [14] or as a function of polymer concentration [8,16]. However, these studies were examining static materials, where the phase transition was simulated. Our study is looking at the dynamic transition, measuring the changing surface wave properties in real-time over the course of gelation. One possible explanation for this behavior is that as a material transitions between liquid and solid states there will be a high degree of spatial phase heterogeneity. This will lead to a much greater variation in the oscillatory frequencies generated, with destructive interference from out of phase oscillations leading to an elevated damping. Additionally, it is also possible that this measured result is reflecting an actual temporary increase in viscosity as the gel goes an intermediate structure during gelation. Conventional approaches for the measurement of dynamic changes in viscosity during hydrogel formation do not show this intermediate peak, but this difference may partially attributed to structural alterations caused by contact-based measurement that alter structure of a partially formed gel.

3.3.6 Crossover (elastocapillary number and length)

To examine further the dynamic crossover from the capillary to elastic regimes due to the interplay of both surface tension and shear modulus in the material, we define a dimensionless elastocapillary number for RAR, $\Lambda = \frac{aG_0}{\sigma} = \frac{a}{l_e}$, where $l_e = \sigma/G_0$ is the elastocapillary length, to describe the relative importance of elasticity to surface tension in the resonant surface oscillations. By scaling the resonant angular frequency of the pseudocapillary and Rayleigh waves by the capillary wave frequency, we obtain

$$\frac{\omega_{pc}}{\omega_c} = \sqrt{1 + \frac{4G_0}{\sigma k_m}} = \sqrt{1 + \frac{4}{\alpha_m}\Lambda} \quad , \qquad \text{for } \Lambda < \Lambda_{CR} \qquad [12]$$

$$\frac{\omega_R}{\omega_c} = \sqrt{1 + \frac{\beta G_0}{\sigma k_m}} = \sqrt{1 + \frac{\beta}{\alpha_m}\Lambda} \quad , \qquad \text{for } \Lambda \geq \Lambda_{CR} \qquad [13]$$

where Λ_C is a critical value associated with the capillary to elastic transition in RAR measurements. At the crossover, $\left(\frac{\omega_{pc}}{\omega_c}\right)^2 = 1 + \frac{4}{\alpha_m}\Lambda_{CR}$ and $\left(\frac{\omega_R}{\omega_c}\right)^2 = 1 + \frac{\beta}{\alpha_m}\Lambda_{CR}$, thus

$$\Lambda_{CR} = \frac{\alpha_m}{4-\beta}\left[\left(\frac{\omega_{pc}}{\omega_c}\right)^2 - \left(\frac{\omega_R}{\omega_c}\right)^2\right]. \qquad [14]$$

From the measured angular frequency of a capillary wave at T_0, as well as the measured angular frequency for pseudocapillary wave and Rayleigh wave at the crossover region 509 ± 13 and 425 ± 7 rad/s, we determined Λ_{CR} = 0.82 ± 0.15. This corresponds to a critical shear modulus G = 9.1 ± 1.7 Pa, if we assume the surface tension remained unchanged during the fibrin gelation in this study.

3.3.7 Multiple plate size comparisons

Importantly, data obtained from experiments using different size of microwells was used to verify that RAR measurements are able to identify the intrinsic viscoelastic properties of a material and are not limited to comparisons of materials with identical geometry. Dynamic RAR measurements were performed over the course of gelation for fibrin gels in 96 and 48-well microplates. The different geometries of these plates resulted in circular samples surfaces with diameters of 6.5 and 11 mm, respectively. Comparing measured frequencies over time for an 8 mg/ml fibrin gels in 96 and 48 well plates (Fig. 3.4A and 3.5A) showed similar gelation kinetics, but with a clear negative shift in frequencies for samples with a larger sample diameter. Calculations of the surface tension from initial frequencies, representing the capillary waves on a fibrinogen solution, were extremely close at 36.4 ± 0.6 and 36.1 ± 0.7 mN·m, for 96-well and 48-well geometries. There was not a clear discontinuity in the heatmap at the start of gelation for the 48-well samples (Fig. 3.5B), but dynamic damping measurements for these samples (Fig. 3.5C) displayed a small local peak, indicative of gel point, at approximately the same time as the 96-well

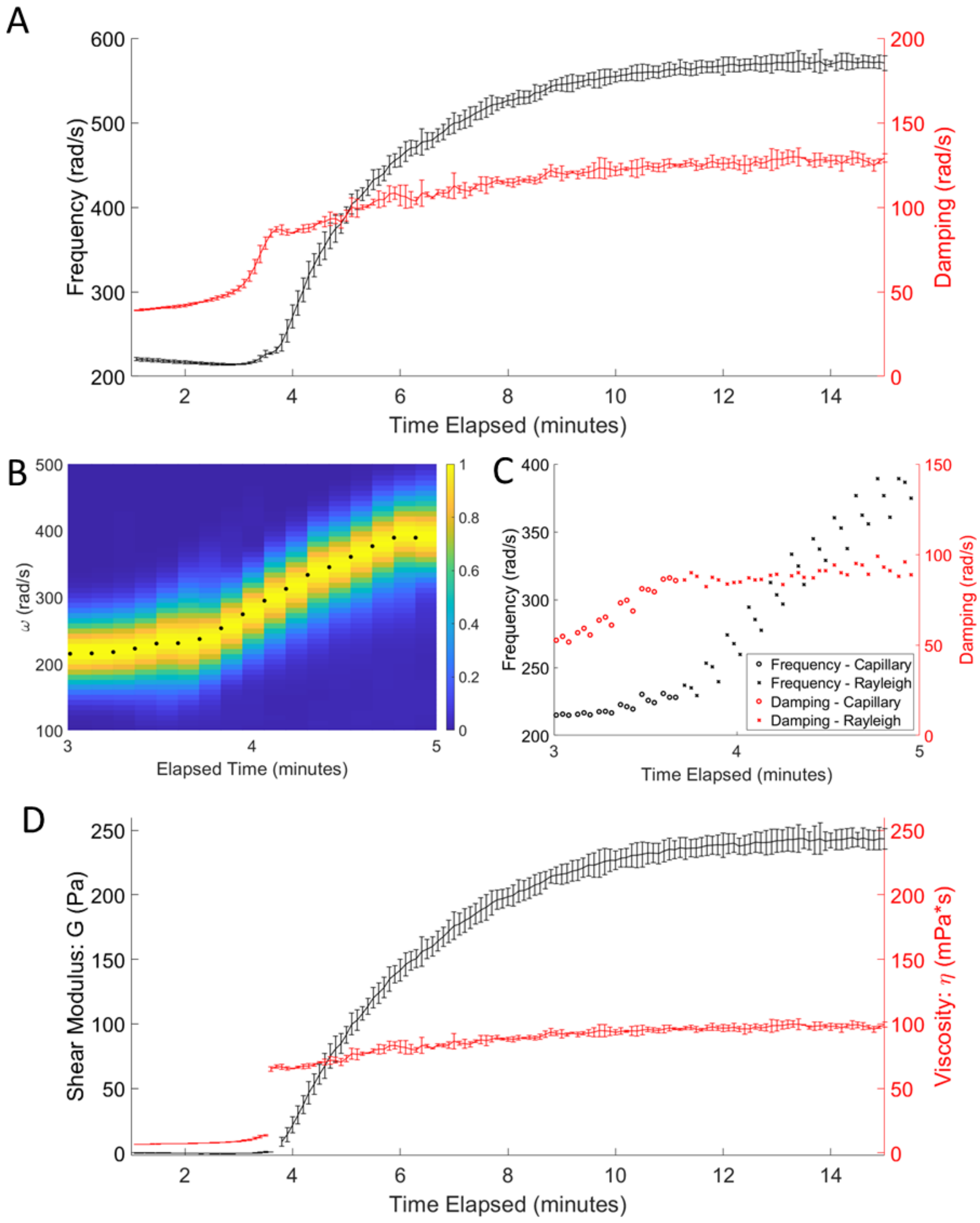

Figure 3.5: Dynamic RAR measurements from the gelation of 8.0 mg/ml fibrin gels in a 48-well plate. A) Natural frequency (left axis) and damping coefficient (right axis) measured over time following the addition of 0.1 U/ml thrombin. B) Close-up view of the power spectrum heatmap at the crossover with black dots indicating fitted peaks. C) Individual natural frequency (left axis) and damping coefficient (right axis) measurements near the crossover point. D) Combined shear modulus (G) and viscosity (***η***) measured over the entire gelation. Error bars represent standard deviation (n=4).

geometry, T = ~220s, showing that the measured kinetics of gelation are very similar for the two samples. The shear modulus and viscosity were calculated piecewise using the appropriate hydrodynamic equations during the pseudocapillary phase (T<220s) and Rayleigh phase (T>220s) (Fig. 3.5D). While not identical, these comparisons show that the final measured shear moduli, 214 ± 14 Pa and 244 ± 10 Pa for 96 and 48 well geometries, have only a 13% difference, compared to the 38% difference between the final resonant frequencies.

Additional experiments performed with 4 mg/ml fibrin gels confirmed the kinetic similarities between gels formed with different geometries in both frequency and damping. However, unlike the 8 mg/ml fibrin gels, accounting for different geometries in the calculation of the shear modulus and viscosity did not adequately correct for differences in the resonant properties. While the final shear moduli are similar in magnitude for the 8 mg/ml samples, the lower concentration fibrin samples had more than a 50% difference in the final calculated shear moduli (Figure 3.6). A previous study, shown in Chapter 2, comparing the shear moduli of stable gelatin and agarose samples in different sized microplates confirmed the results seen in high concentration fibrin, where geometric correction in modulus calculation was successful (Fig. 2.10). These results indicate our modulus calculations are accurate for stiffer materials (> 100Pa) but require further refinement in softer gels. The greater elastocapillary lengths in these softer gels may allow for the development of resonant oscillations outside the 0,2 mode previously observed.

An additional resonant mode appears during the gelation of the 4 mg/ml fibrin in a 96 well plate (Fig. 3.3D) for all replicates. Approximately 3 minutes after the addition of thrombin, near the crossover point, a lower frequency peak appears, in addition to what we assume to be the 0,2 mode seen in other materials. This peak in the power spectrum increases in frequency, like the peak for the 0,2 oscillation, and in amplitude relative to the 0,2 peak, quickly overtaking it as the highest peak over the next few minutes. This additional mode raises the possibility that the single oscillatory mode measured after crossover for the 4 mg/ml fibrin in a 48 well plate may not actually be the 0,2 mode. Further experimentation, using high-speed imaging in conjunction with RAR for a variety of sample geometries and at low fibrin concentrations may be necessary to elucidate what oscillatory mode we are measuring and improve our ability to correct for geometric variations with very soft hydrogels.

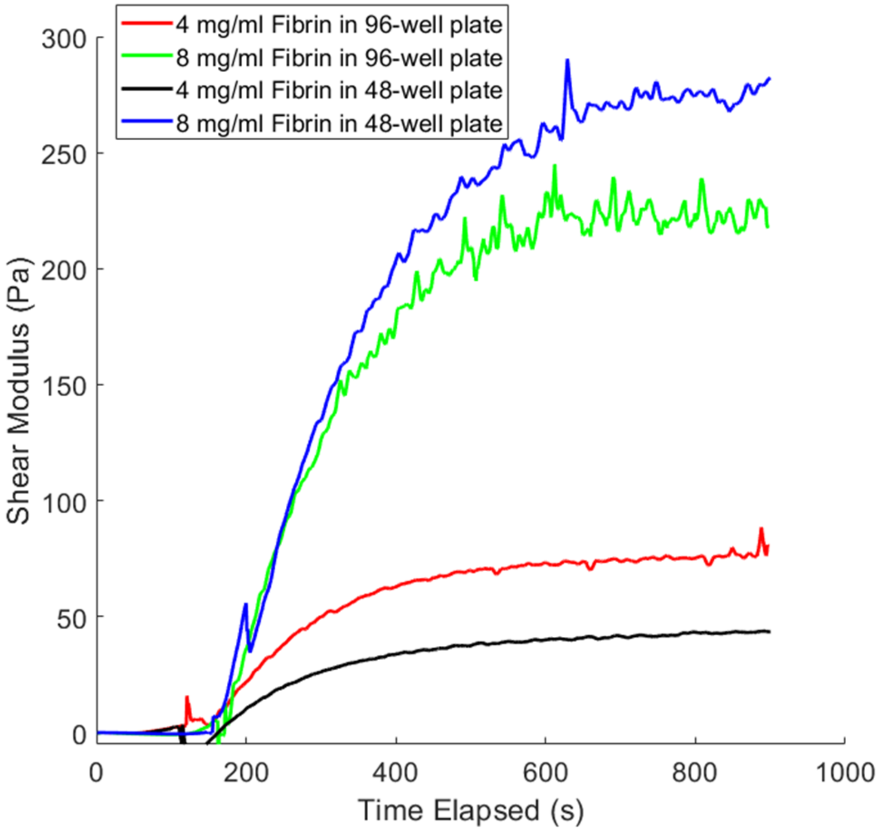

Figure 3.6: Rough calculation of average shear moduli shear kinetics for 4 and 8 mg/ml fibrin gels in 48 and 96 well plate geometries (n=4).

3.3.8 Blood coagulation kinetics

Following the initiation of coagulation in citrated porcine blood through the addition 0.02M $CaCl_2$ dynamic changes in blood mechanics were measured using RAR. Heatmaps of dynamic displacement and power spectra were generated (Fig. 3.7A and B) in the same manner as Figures

3.3C and 3.3D. The heatmaps closely resembled those of fibrin gels. As with fibrin, initial measurements of high amplitude and low frequency resonant waves followed by a rapid increase in frequency represent the transition from capillary waves on the surface of liquid blood to pseudocapillary and finally Rayleigh waves as coagulation progresses. While the initial frequencies and kinetics are similar to that of purified fibrin, the maximum frequency achieved

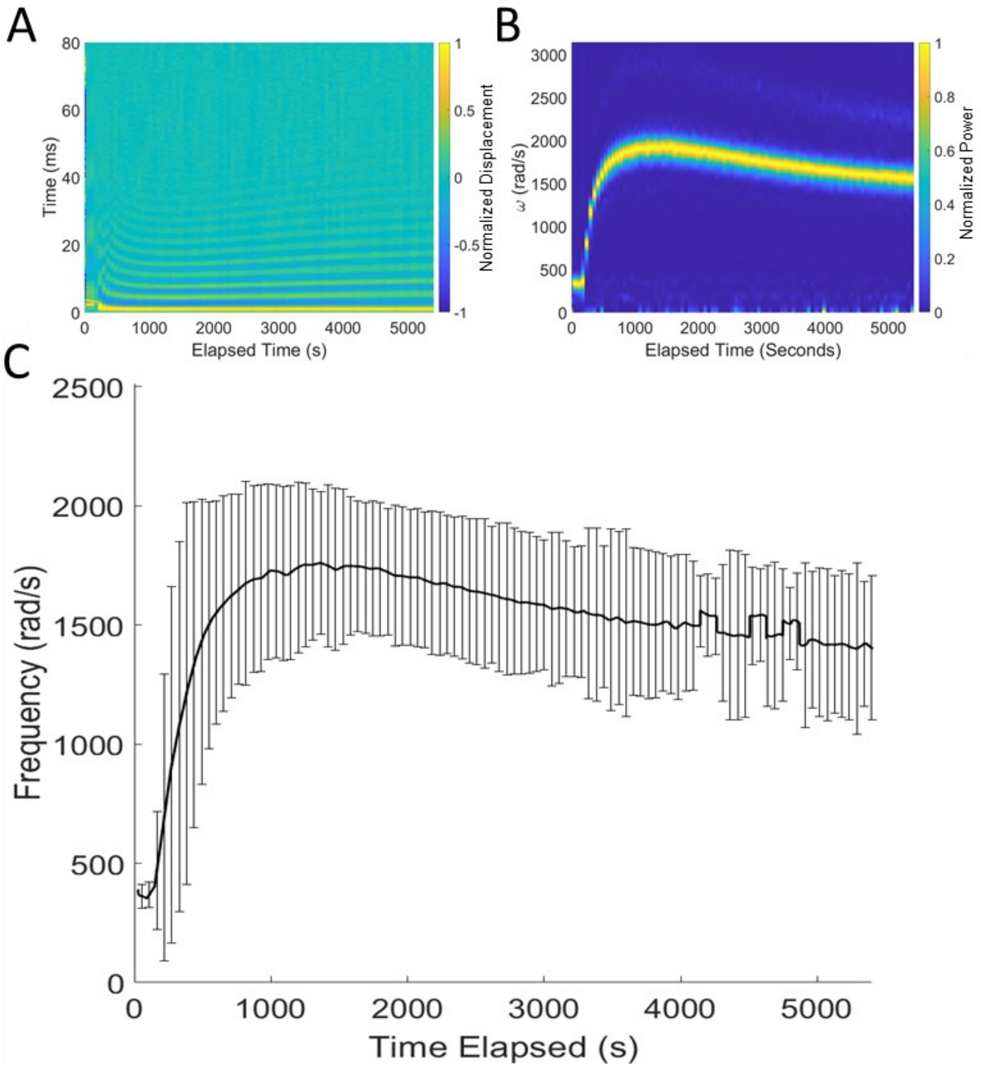

Figure 3.7: A) Heatmap showing normalized displacement (color) of whole blood sample as a function of oscillation time (vertical axis) and elapsed time since $CaCl_2$ addition (horizontal axis). B) Heatmap of changing power spectra for whole blood**.** Color indicates the normalized power over the frequency spectrum (vertical axis) as a function of the elapsed time since $CaCl_2$ addition (horizontal axis). C) Dynamic RAR measurements of natural frequency from the coagulation of whole porcine blood in a 96-well plate. Error bars represent standard deviation (n=4).

with coagulated whole blood was approximately 2-fold higher than 8 mg/ml fibrin and 3-fold higher than 4 mg/ml fibrin (Fig. 3.7C). Typical fibrinogen concentrations in blood range from 1.5 to 4 mg/ml [17]. The increased stiffness measured in the clots, must therefore result from the additional elements not present in the pure fibrin gels, such as platelet contraction and fibrin crosslinking via Factor XIII [18]. An additional dynamic phenomenon is observed in the long-term viscoelastic properties of the blood clot, where a peak shear modulus was achieved approximately 30 minutes after initiation but was followed by a gradual reduction in stiffness. This reduction was not observed in pure fibrin-thrombin gels, and therefore may be the result of the additional elements found in whole blood, such as plasmin mediated degradation of fibrin networks or the relaxation of platelets [19]. The separate components of clot softening can be explored individually in order to compare the diagnostic insights from RAR and conventional thromboelastography, measuring fibrinolysis in plasma and whole blood clots while utilizing various plasmin activators or inhibitors, such as tPA or aprotinin, to isolate specific mechanisms.

3.3.9 PEG-NB Kinetics

Unlike the enzymatic reactions driving fibrin polymerization, PEG-norbornene (PEG-NB) gels required the application of UV light to initiate crosslinking. Dynamic RAR measurements were performed, tracking the mechanical development of solutions with 30, 50, and 100 mg/ml PEG-NB with 0.5, 1, or 2 mM LAP during a 1 minute illumination with a 365nm UV LED. Spectral heatmaps were generated for each composition measured (Fig. 3.8). Clear trends in the maximum frequencies can be observed moving from left to right, with increased PEG-NB concentration leading to a higher frequency after UV crosslinking. Additionally, there were observed differences in the kinetics of gelation for samples with variable LAP concentration, increasing from top to bottom.

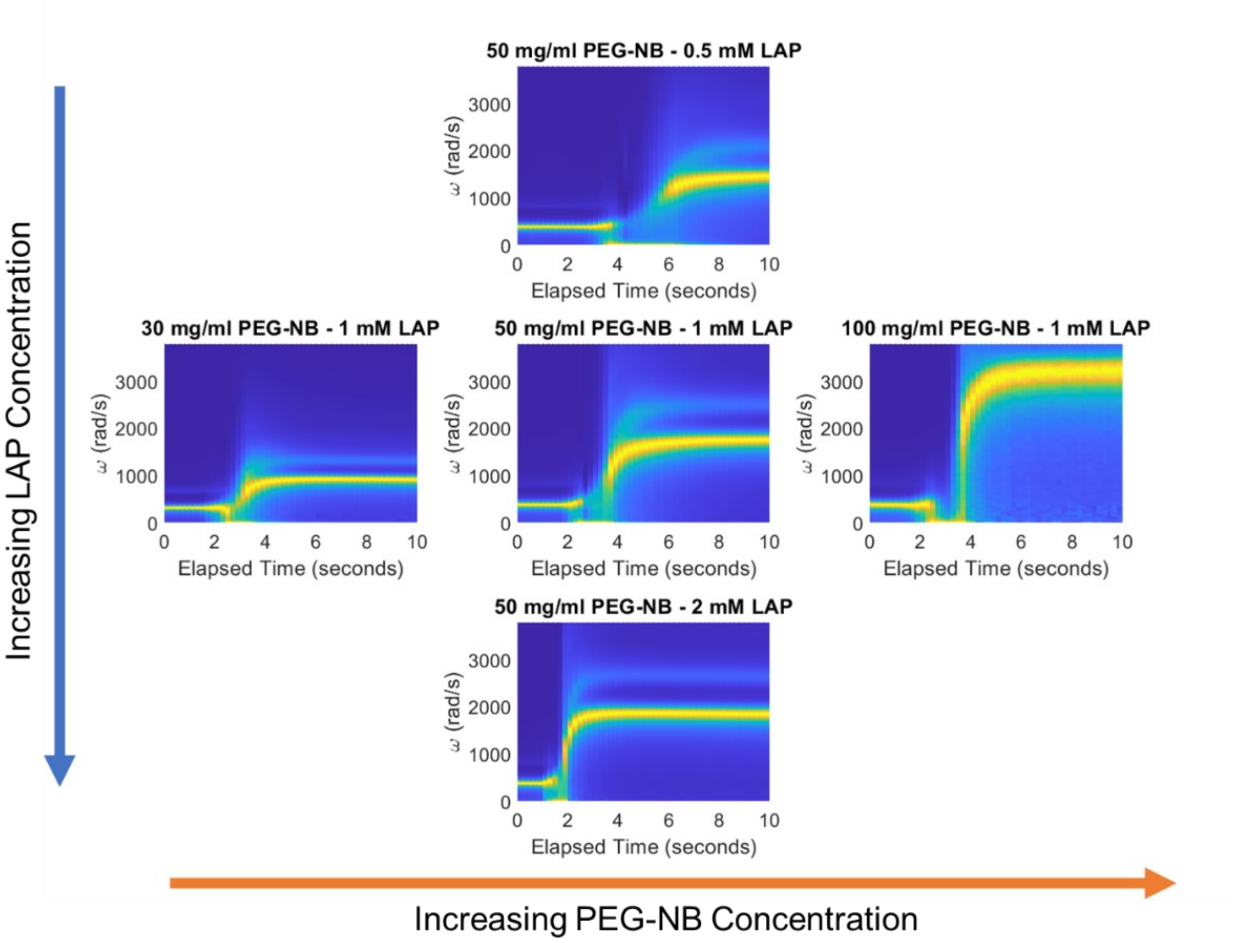

Figure 3.8: Heatmaps of changing power spectra for PEG-NB gels crosslinked using UV with variable PEG and LAP concentrations**.** Color indicates the normalized power over the frequency spectrum (vertical axis) as a function of the elapsed time since the initiation of gelation (horizontal axis).

The dynamic shear modulus was calculated using the piecewise method described above (Fig. 3.9A) and showed a sinusoidal increase with time. While similar in shape to the dynamic measurement of fibrin gelation, the PEG-NB crosslinking occured almost 2 orders of magnitude faster, starting to increase as soon as 2 s after the initiation of UV illumination and reaching a stable maximum value in less than 10 seconds. To measure changes with this high temporal resolution we developed the rRAR protocol, combining multiple excitation pulses into a single tracking measurement which enabled sampling rates as high as 5 Hz.

The concentrations of PEG-NB and LAP have substantial effects on the dynamic viscous measurements (Fig. 3.9B). Like the impact of polymer concentration on shear modulus, PEG concentration impacts the magnitude of viscosity in the crosslinked gels without noticeably impacting the kinetics of gelation. The viscosities of 30, 50, and 100 mg/ml PEG-NB gels after fully crosslinking were significant different, measuring 50 ± 1, 87 ± 3, and 232 ± 15 mPa·s, respectively. Increases in the LAP concentration of 50 mg/ml PEG gels did not impact the viscosity after fully crosslinking, but did decrease the delay before the sharp peak in damping.

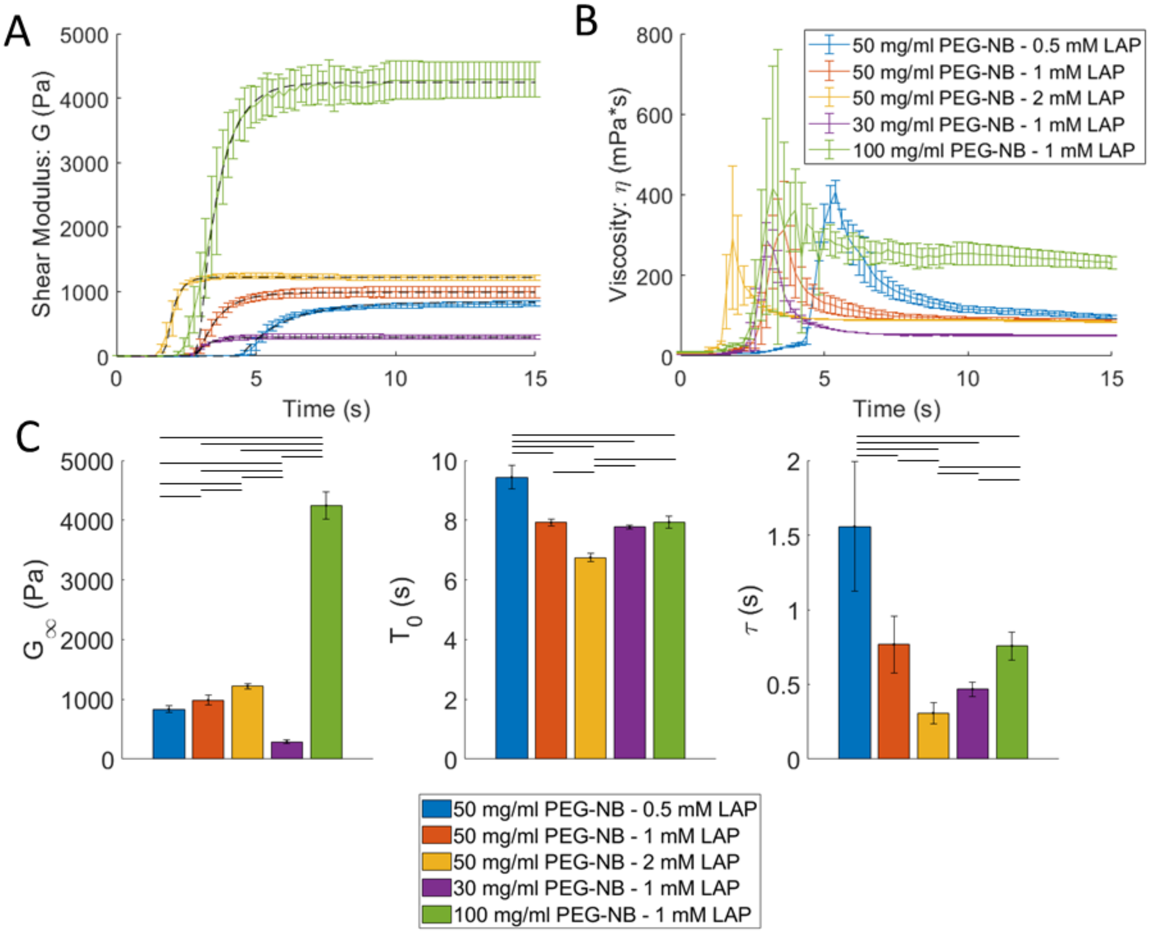

Figure 3.9: A) Combined shear modulus (G) and B) viscosity ($\boldsymbol{\eta}$) measurements of PEG-NB gels generated using rRAR over the first 15 seconds of UV crosslinking. Dashed black line represents exponential model fitting. Comparison of the fitted parameters C) final shear modulus ($\boldsymbol{G}_\infty$), D) lag-time (T_0), and E) time constant ($\boldsymbol{\tau}$). Error bars represent standard deviation (n>3). Horizontal lines indicate significant differences between groups with $p < 0.05$.

To compare the dynamic changes in elastic properties, the combined shear modulus was fit to the following exponential model using a least-squares optimization,

$$G(T) = G_{\infty}(1 - e^{-\frac{(T-T_0)}{\tau}}), \tag{15}$$

to extract the final shear modulus (G_{∞}), the lag-time before gelation (T_0), and a time constant for the rate of gelation τ. The average of fittings for each material formulation are shown in Fig. 3.8A as dashed lines, and the fitted parameters are shown in Fig. 3.8C-E.

The maximum resonant frequency achieved (Fig. 3.9C) correlates with increasing PEG-NB concentration, corresponding to final shear moduli of 291 ± 36 Pa, 990 ± 86 Pa, and 4245 ± 230 Pa for the 30, 50, and 100 mg/ml gels, respectively. These differences in shear modulus were significant ($p < 0.005$). PEG-NB solutions with a constant 50 mg/ml polymer concentration, and LAP concentrations of 0.5, 1, and 2 mM, were also measured to explore differences in crosslinking kinetics due to changes in the rate of free-radical production. Although smaller than differences due to PEG-NB concentration, changes in LAP did have a small but significant effect on the G_{∞} ($P < 0.05$), increasing from 837 ± 56 Pa to 990 ± 86 Pa to 1221 ± 42 s Pa for 0.5, 1 and, 2 mM LAP, respectively. The different LAP concentrations also result in clear kinetic differences in the dynamic resonant frequency curves. The lag-time before gelation (Fig. 3.9D) did not show any relationship with bulk polymer concentration, as there were no significant differences in T_0 between gels made with 1 mM LAP, but the lag-time before gelation decreased with LAP concentration, ranging from 1.8 ± 0.2 s, 2.9 ± 0.1 s, and 5.4 ± 0.4 s for 0.5, 1 and, 2 mM LAP, respectively. Finally, the time-constant (Fig. 3.9D) also showed a significant decrease with increasing LAP concentration (0.3 ± 0.1 s, 0.8 ± 0.2 s, and 1.6 ± 0.4 s for 0.5, 1 and, 2 mM LAP). Also, while there was no significant difference in τ between 50 and 100 mg/ml PEG gels, the 30 mg/ml gels did have a significantly lower value.

These results highlight the modularity of photopolymerized PEG system when compared to fibrin. While increasing polymer concentration leads to an increase in modulus and viscosity for both PEG and fibrin hydrogels, the kinetics of the fibrin gels vary significant with concentration where the PEG gels do not.

3.3.10 Overdamped phase

A small discontinuity was observed in the extracted measurements of both resonant frequency and damping shortly after the beginning of gelation for 30, 50, and 100 mg/ml PEG gels with 1 mM LAP. Close observation of the dynamic power spectra (Fig. 3.10A-C) showed that during this period the peak spectral frequency shifts abruptly to 0 rad/s. This can be seen by the thin band of yellow at 0 rad/s between 2 and 4 seconds of elapsed time. This indicates that the resonant surface waves are no longer forming a completely underdamped harmonic oscillator. This transition occurs when the damping ratio, defined as $\zeta = \frac{\Gamma}{\omega_0}$, is equal to or greater than one, respectively indicating a critically damped or overdamped system. Our extraction of resonant parameters relies on the identification and fitting of Lorentzian peaks in the power spectrum, but this only functions with an underdamped oscillation so we are unable to quantitatively measure when $\zeta > 1$. However, we can observe the asymptotic shape of the damping ratio time series (Fig. 3.9A-C) and infer that the missing points are crossing that threshold value of $\zeta \geq 1$. Comparing individual power spectra at times before, during, and after this transition, there are notable differences in the shape of the middle peak (Fig. 3.10D-F). There is still a measurable frequency peak at the 3 second elapsed time for the 30 mg/ml PEG-NB gel, but it is no longer the global maximum in the power spectrum and is significantly broader than the 0 and 6 second peaks. The power spectra for 50 mg/ml and 100 mg/ml PEG-NB do contain any recognizable Lorentzian peak at the 3 second point, demonstrating the reason for the gap in fitted resonant parameters at this time. This phenomenon can also be observed directly in the displacement time-series data (Fig. 3.10G-I). Displacement curves for both the uncrosslinked solutions (0 s) and fully crosslinked gels (6 s) have the expected shape of an exponentially decaying sinusoidal oscillation. The curve of displacement at 3 s, however, shows only an exponential decay following the initial deformation, the characteristic shape for a critically-damped or over-damped oscillator. This is particularly pronounced in the 100 mg/ml PEG-NB gel, where the surface does not oscillate at all, slowly returning to the baseline position after the initial excitation.

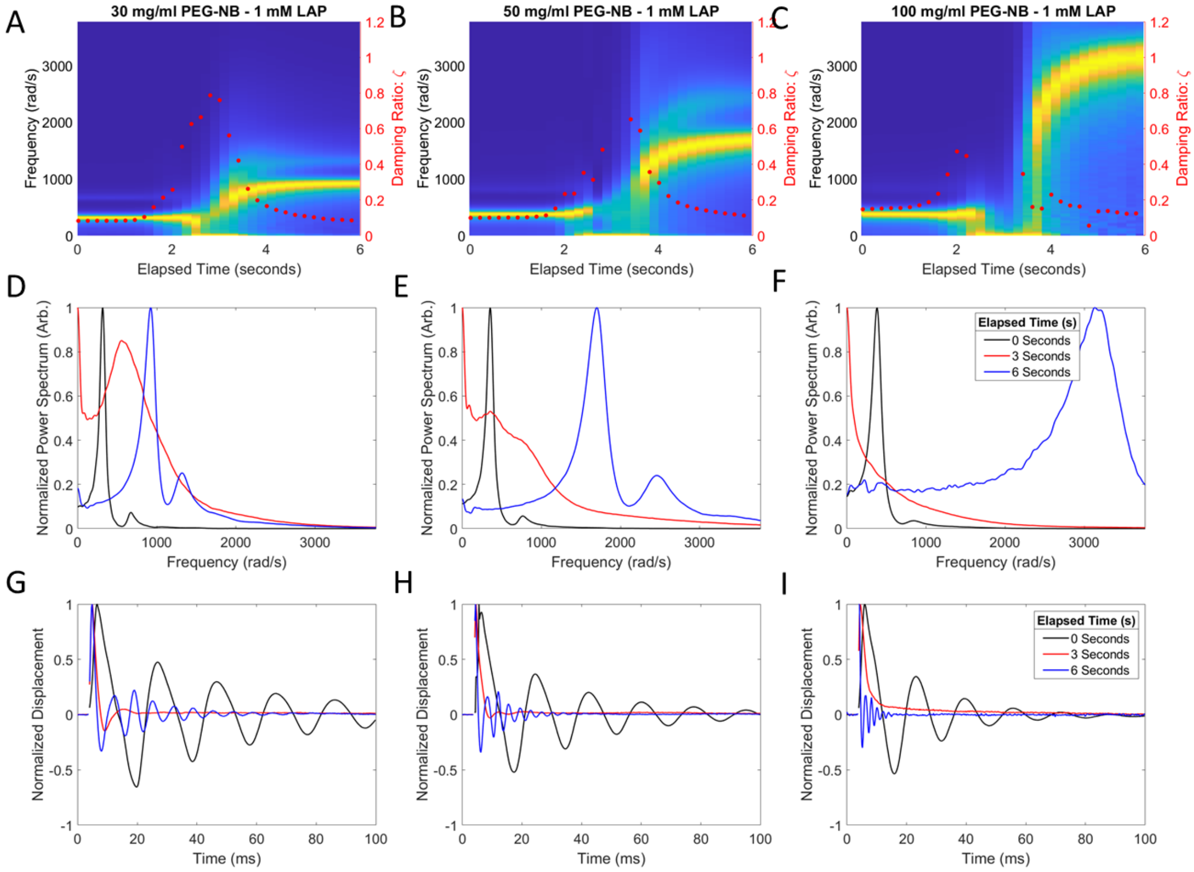

Figure 3.10: Close-up view of the power spectrum heatmap at the crossover for UV crosslinked PEG-NB with concentrations of A) 30, B) 50, and C) 100 mg/ml. The red dots indicate the damping ratio (ζ), showing the drastic increase during crossover. D-F) Power spectra and G-I) displacement time series for D&G) 30, E&H) 50, and F&I) 100 mg/ml PEG-NB gels before, during and after UV crosslinking.

As previously discussed, this dramatic increase in damping relative to resonant frequency occurs as the solution reaches the gel point. While a sharp peak in damping has been observed in other materials discussed in this study, we only observed this phenomenon of overdamping in PEG hydrogels. This difference in the viscoelastic kinetics may be explained as resulting from the structural and mechanistic differences in gels and polymerization, with PEG gels forming from the UV initiated covalent crosslinking of individual branched polymer chains and the natural materials, including fibrin and LAL gels, forming as enzymatic cleavage of precursor proteins, fibrinogen and coagulin respectively, generating the building blocks for solid fibrillar gels. Alternatively, temporary overdamping during phase transition may not be unique to PEG but is only detected in this system due the higher measurement sampling rate of rRAR.

3.3.11 LAL kinetics:

The most common LAL based methods for endotoxin detection are the gel clot, turbidimetric, and chromogenic assays [20]. The gel clot assay looks at the simple presence or absence of a solid clot after the addition of a solution that may contain endotoxin. This approach is semi-quantitative, only identifying whether or not a solution is above or below a threshold endotoxin concentration that will form a clot in a defined time frame. Unlike the gel clot assay, the turbidimetric and chromogenic assays do not utilize mechanical changes, but track optical changes due, respectively, to either increased absorbance during coagulin polymerization or to the release of a chromophore from a modified coagulogen during the enzymatic cleavage. The approaches allow for dynamic monitoring of the clotting process, enabling quantification of the endotoxin concentration as a function of the time delay to reach a set optical threshold. This approach however is limited in the case of samples that interfere with optical measurements, such as those containing chromophores or colloidal suspensions.

In order to overcome conventional limitations to the robust quantification of endotoxin concentration, we have used RAR to measure the changing viscoelastic properties of LAL solutions. Spectral heatmaps generated from dynamic measurements of coagulin gels forming with endotoxin added to a DI water medium, ranging from 0.002 to 0.5 EU/mL, showed a sigmoidal kinetic profile (Fig. 3.11). As with fibrin, we can see a discontinuity in the frequency early in the gelation process. The timing of this discontinuity varies with endotoxin concentration, occurring as early as 20 minutes and as late as 80 minutes after the addition of endotoxin.

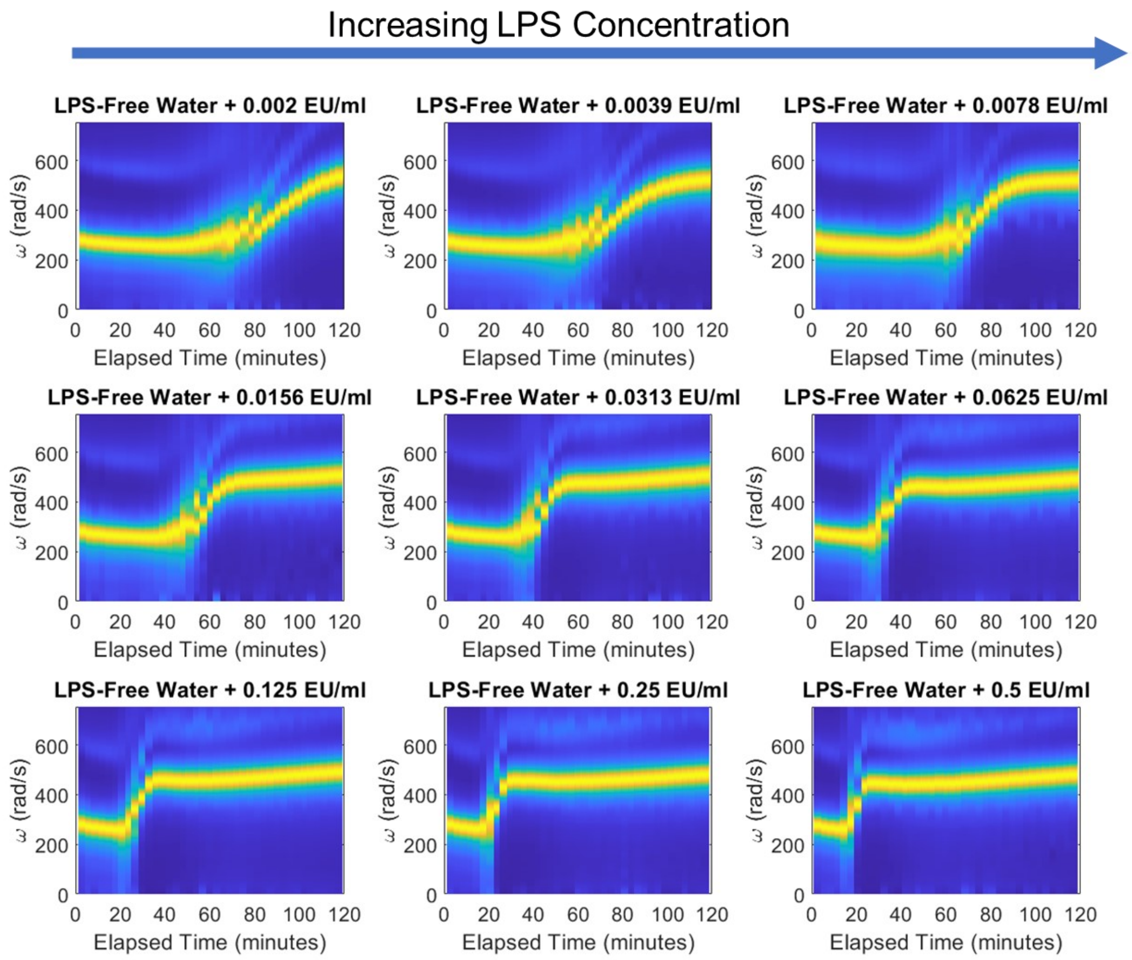

Figure 3.11: Heatmaps of changing power spectra for LAL gel clots crosslinked with endotoxin concentration ranging from 0.002 EU/ml to 0.5 EU/ml**.** Color indicates the normalized power over the frequency spectrum (vertical axis) as a function of the elapsed time since the initiation of gelation (horizontal axis).

Extraction of the resonant frequency allows for direct comparison of the gelation kinetics (Fig. 3.12A), showing a clear decrease in both the duration of the capillary phase and a decrease in the final frequency with increasing endotoxin concentration. The slight differences in kinetics for replicate measurements does result in the loss of a clear discontinuity when comparing average frequencies Similar to damping measurements in fibrin or PEG, the dynamic damping behavior of

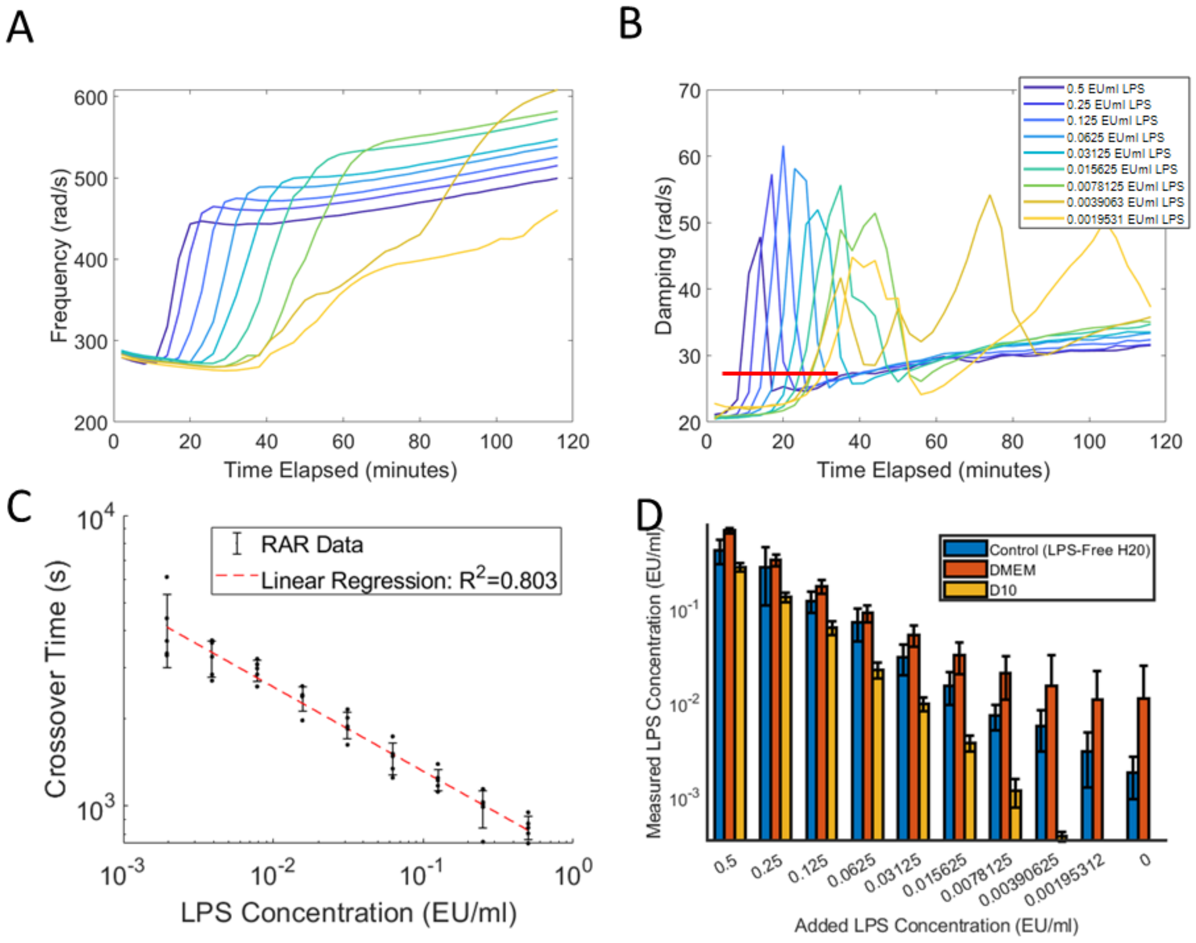

Figure 3.12: Dynamic measurements of LAL gel clots. A) Natural frequency and B) damping coefficient measured repeatedly for 2 hours after the addition of endotoxin at concentrations ranging from 0.002 EU/ml to 0.5 EU/ml. Lines show the mean measurements at interpolated time points (n>3). Red Line represent the threshold damping value for determining the starting of the phase transition. C) Calibration curve, relating endotoxin concentration to crossover time on a log-log axis with a dashed red line for the linear regression. Error bars represent standard deviation (n>3). D) Comparison between the concentration of endotoxin added to D10, DMEM, and water and the concentrations measured using the dynamic RAR measurements.

LAL gels (Fig. 3.12B) is characterized by a rapid increase as gelation initiates followed by a rapid decline as the surface waves transfer from primarily pseudocapillary to Rayleigh. With increasing endotoxin concentration, we observed a clear increase in the rate of gel formation. Increases in the rate were characterized by a decreased delay before pseudocapillary frequency or damping increase, a decrease in delay before pseudocapillary to Rayleigh transition, and an increase in the maximum slope of Rayleigh frequency increase. The role of endotoxin in controlling the kinetics of gel formation is expected, as explained earlier, due to its role as the initiator of the clotting cascade.

3.3.12 RAR-LAL Gel Clot Assay:

As a direct comparison to conventional gel clot LAL assays, we compared the resonant frequency and damping for samples at each endotoxin concentration exactly 1 hour after the assay start. While the single-point measurements of frequency (Fig. 3.13A) show significant differences between the high (>0.015 EU/ml) and low (<0.005 EU/ml) endotoxin concentrations, there is no consistent correlation between the measured frequency and endotoxin concentration this approach, meaning that this will still only provides a binary output. Single-point measurements of damping (Fig. 3.13B) do not show any significant differences between higher endotoxin concentration samples. There is an increase in the variability of this measurement at concentrations below 0.01 EU/ml, but there is no trend that could aid in the quantification using this metric. The use of RAR to quantify the mechanics may increase the assay sensitivity beyond the manufacturer's designated sensitivity for this assay of 0.03 EU/ml.

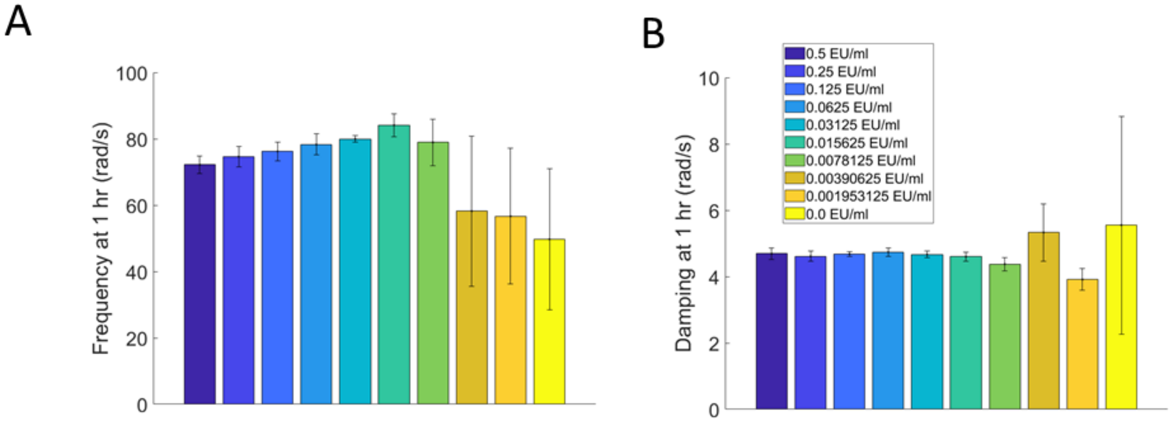

Figure 3.13: Analog to traditional gel clot measurements. A) Natural frequency and B) damping coefficient measured 1 hr after the addition of endotoxin at concentrations ranging from 0.002 EU/ml to 0.5 EU/ml.

This application of RAR can reduce the subjectivity of a conventional gel clot assay, by providing a quantitative output for discriminating between positive and negative samples. It does not, however, overcome the inherent qualitative limitation of the gel clot method. The quantitative measurement of endotoxin using LAL gel mechanical properties required the use of dynamic results.

3.3.13 RAR-LAL Dynamic Quantification:

We identified a metrics for quantification based on the dynamic RAR measurements, utilizing the stark changes in damping that occur during the transition from pseudocapillary to Rayleigh wave behavior. Like the optical threshold used to in turbidimetric or chromogenic assays, we defined a damping threshold of 7 Hz, shown as a dashed red line in Fig. 3.12B, to identify the early stages of gelation, referring to this event as the crossover time. Fig. 3.12C shows the crossover time plotted against the endotoxin concentration in standards prepared with DI water. When plotted on a logarithmic scale there is a clear linear relationship with a decreasing slope, indicating a consistent decrease in gelation time with increasing sample endotoxin concentration.

A linear regression was performed (R^2 = 0.803) and used to compare the added endotoxin concentration with that measured using RAR. With this approach we found the limit of blank (LOB) to be 0.003 EU/ml and the limit of detection (LOD) to be 0.006 EU/ml. This indicates that we can quantify endotoxin concentrations far below the reported gel clot sensitivity for this assay of 0.03 EU/ml.

3.3.14 RAR-LAL Interference:

The ability of this assay to function with various mediums was also tested. In addition to endotoxin diluted in DI water, DMEM, and D10 were also tested as potential diluents. These mediums are commonly used in mammalian cell culture, providing a practical test of our dynamic RAR-LAL assay. Crossover times were calculated from dynamic RAR as previously detailed and was used to calculate predicted endotoxin concentrations (Fig. 3.12D). Endotoxin concentrations in DMEM were slightly overpredicted for all concentrations. This overprediction of endotoxin concentration relative to control indicates that the addition of DMEM increases the kinetics of coagulin gelation. The addition of 10% FBS also impacted the dynamic gelation of the LAL reagent. The measured endotoxin concentrations in D10 were significantly lower than control, with no detectable crossover for the lowest concentrations of endotoxin after 2 hours. This indicates that while DMEM may increase the rate of coagulin gelation, FBS inhibits this enzymatic process.

A variety of media components present in DMEM, including sodium chloride, L-arginine, and glucose, have been identified as potential inhibitors of the LAL clotting cascade. However, the mechanical RAR method was not significantly affected by these medium components, maintaining a sensitivity similar to the control for most concentrations. This result is particularly important due to the presence of phenol red in DMEM. While inconsequential to a mechanical assay, Phenol red acts as both a chromophore and fluorophore, with spectral properties influenced by pH, adding a potentially variable interference to an optical assay. While interference was observed with the D10 media, this is expected as serum is known to be a potent inhibitor of the LAL assay clotting potential. Despite inhibition, a clear relationship was still, observed between crossover time and endotoxin concentrations well below the reported 0.03 EU/ml, indicating that a dynamic mechanical assay of LAL using RAR is robust enough to be used in samples that possess some level of assay inhibition.

3.4 Conclusions

This study using RAR obtained longitudinal measurements of the same samples at high temporal resolution in a sterile condition, capturing the dynamic changes during fibrin, PEG, and coagulin gelation, and revealing the capillary to elastic transition. We were able to identify unique phenomena in the resonant oscillations measured by RAR, identifying a transition between capillary and Rayleigh waves during phase transition, as well as a pronounced elevated damping during this intermediate period. Building upon these observations, dynamic RAR measurements of coagulin gels formed during an LAL gel clot assay were used to identify the gel point. This further was demonstrated to be a robust and quantitative predictor of endotoxin concentration.

These dynamic studies used initial measurements, at the start of the gelation process to calculate the surface tension of the polymer solutions. While surface tension of liquids is well-established, the relevant question whether soft biomaterials such as hydrogels exhibit detectable effect of surface tension has only been examined in more detail recently. Jagota et al. [2] reported direct measurement of surface tension of soft solids by observing the changes in deformation of gel replicas of poly (dimethysiloxane) masters with rippled surfaces over time driven by surface tension and resisted by elasticity. However, shear modulus must be determined using other method independently and fabrication of rippled substrates are needed. Similarly, other traditional studies of viscoelastic solution or soft solids, measurement of either surface tension or the shear modulus requires the other parameter to be determined using a different method independently [2,6,8]. In contrast, RAR offers the advantage of measuring both surface tension and shear modulus of soft biomaterials, either by examining the two surface waves in the elastocapillary crossover region or by performing parallel experiments of similar sample using microwells with different well sizes. The capability of RAR to measure surface tension soft gels is particularly important because conventional techniques including Wilhelmy plate and du Nuoy ring, spinning drop, and pendant drop methods, are not suitable for soft gels. These contact-require approaches either fracture the gel or unable to detangle the effects of elasticity from the surface tension [6,8]. A recent study measured surface tension from planar elastocapillary waves [6] but required a large material surface.

In addition, the dimensionless elastocapillary number for RAR, $\Lambda=aG/\sigma$, may be easily adjusted by using different sized sample chamber to match the characteristic elastocapillary length scale σ/G, thus the technique offers the flexibility to examine the elastocapillarity in materials with a wide range of properties. Finally, as noted by Shao et al. [8] regarding the study of elastocapillarity based on gel drop shape oscillation, study of the dynamics of soft materials may have the potential to gain insights into the naturally more complex characteristics than statics due to multiple relaxation time scales. Compared to the study of gel drop oscillation using acoustic levitation and optical imaging [8], RAR uses acoustic pulses for excitation and detection, and when coupled with standard labware, offers a platform decidedly simple and suitable for long term study of biomaterials as well as biological samples such as coagulating blood.

3.5 References

[1] M.L. Oyen, Mechanical characterisation of hydrogel materials, Int. Mater. Rev. 59 (2014) 44–59. https://doi.org/10.1179/1743280413Y.0000000022.

[2] A. Jagota, D. Paretkar, A. Ghatak, Surface-tension-induced flattening of a nearly plane elastic solid, Phys. Rev. E - Stat. Nonlinear, Soft Matter Phys. 85 (2012) 1–6. https://doi.org/10.1103/PhysRevE.85.051602.

[3] R.W. Style, A. Jagota, C.Y. Hui, E.R. Dufresne, Elastocapillarity: Surface tension and the mechanics of soft solids, Annu. Rev. Condens. Matter Phys. 8 (2017) 99–118. https://doi.org/10.1146/annurev-conmatphys-031016-025326.

[4] F. Monroy, Surface hydrodynamics of viscoelastic fluids and soft solids: Surfing bulk rheology on capillary and Rayleigh waves, Adv. Colloid Interface Sci. 247 (2017) 4–22. https://doi.org/10.1016/j.cis.2017.07.006.

[5] S. V. Murphy, A. Atala, 3D bioprinting of tissues and organs, Nat. Biotechnol. 32 (2014) 773–785. https://doi.org/10.1038/nbt.2958.

[6] X. Shao, J.R. Saylor, J.B. Bostwick, Extracting the surface tension of soft gels from elastocapillary wave behavior, Soft Matter. 14 (2018) 7347–7353. https://doi.org/10.1039/c8sm01027g.

[7] J.L. Harden, H. Pleiner, P.A. Pincus, Hydrodynamic surface modes on concentrated polymer solutions and gels, J. Chem. Phys. 94 (1991) 5208–5221. https://doi.org/10.1063/1.460525.

[8] X. Shao, S.A. Fredericks, J.R. Saylor, J.B. Bostwick, Elastocapillary Transition in Gel Drop Oscillations, Phys. Rev. Lett. 123 (2019) 188002. https://doi.org/10.1103/PhysRevLett.123.188002.

[9] F. Monroy, D. Langevin, Direct experimental observation of the crossover from capillary to elastic surface waves on soft gels, Phys. Rev. Lett. 81 (1998) 3167–3170. https://doi.org/10.1103/PhysRevLett.81.3167.

[10] R.B. Dorshow, L.A. Turkevich, First observation of capillary to Rayleigh mode crossover on the surface of polymer solutions, Phys. Rev. Lett. 70 (1993) 2439–2442. http://link.aps.org/doi/10.1103/PhysRevLett.70.2439%0Apapers3://publication/uuid/090B2735-C155-4FD5-A60B-84D4B9BB007E.

[11] E.C. Hobson, W. Li, B.A. Juliar, A.J. Putnam, J.P. Stegemann, C.X. Deng, Resonant acoustic rheometry for non-contact characterization of viscoelastic biomaterials, Biomaterials. 269 (2021) 120676. https://doi.org/10.1016/j.biomaterials.2021.120676.

[12] W.L.M. Nyborg, Acoustic Streaming, ACADEMIC PRESS INC., 1965. https://doi.org/10.1016/B978-0-12-395662-0.50015-1.

[13] Y. Onodera, P.-K. Choi, Surface-wave modes on soft gels, J. Acoust. Soc. Am. 104 (1998) 3358–3363. https://doi.org/10.1121/1.423919.

[14] H. Takahashi, P.-K. Choi, Sol – Gel Transition in Gelatin Observed with Surface Waves, Jpn. J. Appl. Phys. 35 (1996) 2939–2943.

[15] P.-K. Choi, E. Jyounouti, K. Yuuki, Y. Onodera, Experimental observation of pseudocapillary and Rayleigh modes on soft gels, J. Acoust. Soc. Am. 106 (2002) 1591–1593. https://doi.org/10.1121/1.427156.

[16] B.H. Cao, M.W. Kim, H.Z. Cummins, Surface waves on polymer solutions: Complete capillary wave-elastic wave crossover, J. Chem. Phys. 102 (1995) 9375–9379. https://doi.org/10.1063/1.468805.

[17] J.R. Harris, D.J.S. Hulmes, Fibrous Proteins: Structures and Mechanisms, 2017.

[18] N. Tynngård, T. Lindahl, S. Ramström, G. Berlin, Effects of different blood components on clot retraction analysed by measuring elasticity with a free oscillating rheometer, Platelets. 17 (2006) 545–554. https://doi.org/10.1080/09537100600759238.

[19] J.C. Chapin, K.A. Hajjar, Fibrinolysis and the control of blood coagulation, Blood Rev. 29 (2015) 17–24. https://doi.org/10.1016/j.blre.2014.09.003.

[20] M.E. Dawson, A Wealth of Options: Choosing an LAL Test Method, LAL Updat. 13 (1995) 1–3.

Chapter 4 Demonstration of combinatorial material design using RAR

4.1 Introduction

A quick review of the recent tissue engineering literature will undoubtedly demonstrate an incredible diversity of hydrogels currently being developed for medical applications. These materials are used for a variety of roles, such as synthetic ECM, drug delivery systems, contact lenses, and wound closure, and can be constructed from both natural and synthetic polymers. These materials can be precisely tailored, altering structural properties of the physical gel such as elasticity [1,2], viscosity [3,4], or porosity [5–7], as well as those modifying its bioactive potential, such as binding ligand availability [8,9], degradability [10,11], and retention or release of paracrine signaling molecules [12,13].

The flexibility of hydrogel systems may provide the potential to precisely tune a material for any application, however, in practice this is incredibly challenging. Even the simplest hydrogel systems can have a broad range of compositional parameters [14,15], from the polymer chemistry, molecular weight, and concentration to the pH, ionic strength, and temperature of the solution, that can influence the physical properties of the resulting material. Many of these parameters have been studied individually, and while that has helped to form a broad base of knowledge to inform the development new hydrogel formulations, few studies have explored the synergistic relationships between design parameters. To gain insight on these complex, multiparametric relationships it is necessary to apply combinatorial methods to the development and characterization of soft biomaterials [16].

There has been some work applying combinatorial methods to explore the design of tissue engineering materials [8,17,18], however the lack of mechanical characterization tools with sufficient throughput has been identified as a critical bottleneck. Few commercial platforms for high-throughput mechanical testing are available for researchers in an academic setting, there have been reported applications of modified compression or indentation systems to enable to rapid or simultaneous testing of multiple samples [19–21]. While these methods represent an important advancement in high-throughput mechanical characterization, they are limited by requirement for direct material contact during testing. This can damage the hydrogel microstructure and introduce contamination, which may limit these methods to end-point measurements for each sample. This will require additional material samples to be prepared and sacrificed for each measured time-point, generating a substantial experimental burden, particularly in the case of combinatorial studies where there may be tens or hundreds of samples being tested. Bioreactor systems, with integrated force transduction and measurement, have been developed to enable longitudinal material testing, however, scaling these systems for multiple sample testing results in a proportional increase in cost and complexity, limiting their feasibility in high-throughput combinatorial testing [22–24].

In order to address the limitations of existing mechanical characterization techniques we have recently developed a novel methodology, called Resonant Acoustic Rheometry (RAR) [25]. This non-contact method utilizes focused ultrasonic pulses to generate and track oscillatory perturbations on the surface of materials that can be used to quantify the bulk viscoelastic properties. These measurements are performed on samples contained within the sealed wells of a standard cell culture microplate, as shown in Figure 4.1A-C, allowing for the use of conventional automated fluid handling systems for high throughput sample generation and eliminating the risk of contamination during testing. Each measurement only requires a fraction of a second, making it possible to rapidly measure material arrays of up to 96 samples in less than 2 minutes. Additionally, these rapid, non-contact measurements can be repeatedly applied to each sample in a microplate without damage or degradation, allowing for the simultaneous longitudinal measurement of a large number of samples to identify changes in material mechanical over seconds, minutes, and even days (Fig. 4.1D). The throughput of this system is not even limited by

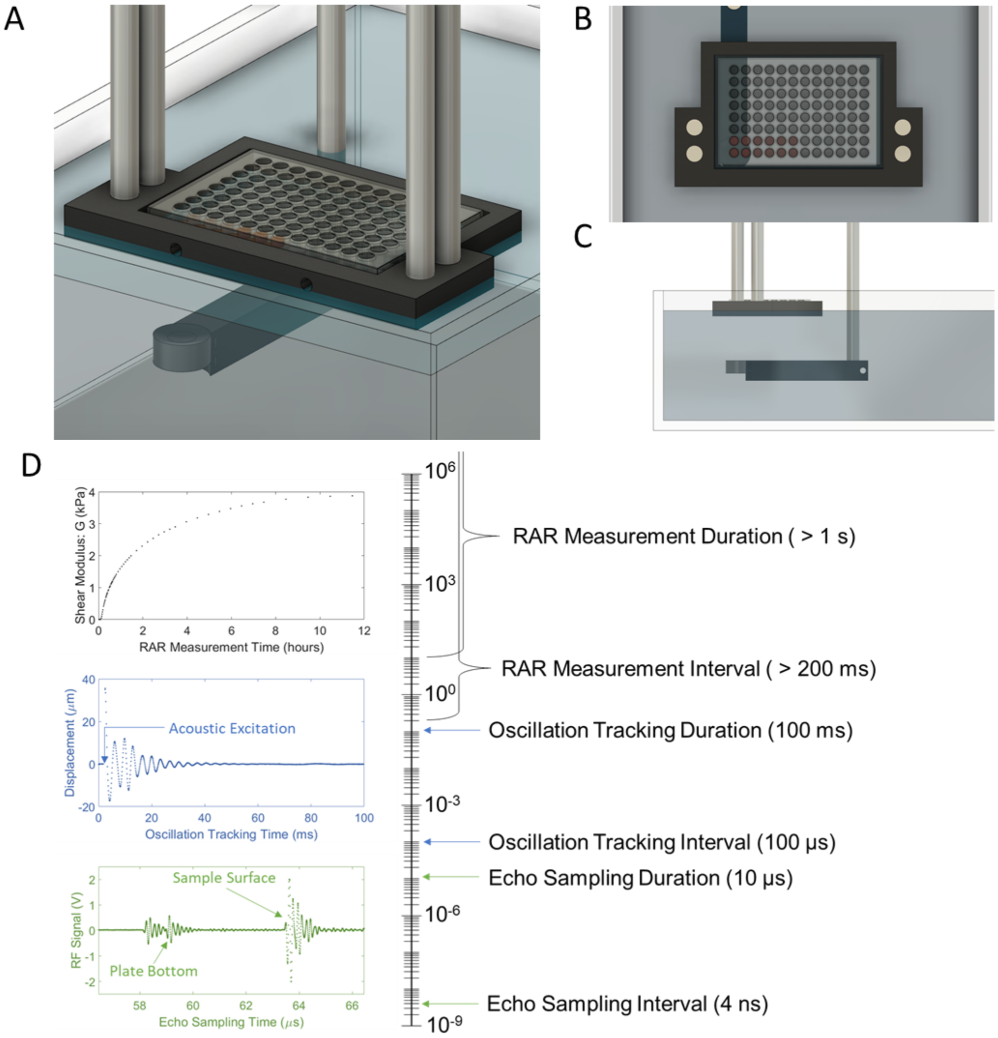

Figure 4.1: 3D model of RAR experimental setup in A) isometric, B) top, and C) side views, showing how the alignment of the transducer and microplate enable plates to be easily switched for high-throughput measurements. D) Logarithmic time scale show how time scales involved in RAR range from nanoseconds for the RF sampling of ultrasonic echoes to thousands and millions of seconds for the duration of longitudinal studies.

the number of wells in a microplate. The experimental setup enables the microplates to rapidly be removed or replaced without interrupting the ongoing study. This is critical for extended kinetic studies, enabling the return of plates to appropriate storage or incubation between measurements. Even more significantly, the ability to quickly swap plates removes any theoretical maximum on the number of samples that can be longitudinally tracked at the same, allowing for numerous studies to be completed in parallel without tying up the instrument. Taken together, RAR is the first mechanical testing platform for viscoelastic characterization with the convenience and throughput of an optical microplate reader.

To demonstrate the utility of RAR for high-throughput, combinatorial material testing we studied the mechanical properties of various formulations of gelatin and fibrin hydrogels. Repeated mechanical measurements with a progressive sampling interval were implemented to explore multiscale temporal changes in gelatin hydrogels during the process of crosslinking using an enzyme, transglutaminase, or a bifunctional crosslinking agent, genipin. We also examined the dynamic mechanical behavior of transglutaminase crosslinked fibrin hydrogels, looking at the interplay between thrombin and transglutaminase concentrations on the coagulation process. From these studies, were able to quantify the differences in gelation kinetics and ultimate mechanical properties between gel formulations, relating these changes to the individual and synergistic contributions of the multiple hydrogel components.

4.2 Materials and Methods:

4.2.1 RAR Method

RAR measurements were conducted as described in Chapter 3, using the standard (not rRAR) methodology. All experiments described in this chapter were performed in 96-well plates filled with material samples in all wells. The average movement speed between wells was optimized by using a snake scan, to avoid the unnecessary moves in a raster scan.

RAR analysis was performed as described in Chapter 3, using the exponentials decay window (R=20) for all measurement. Viscoelastic properties for all gelatin samples were calculated using the Rayleigh model (Equations 10 and 11 from Chapter 3). Fibrin mechanical properties were calculated according to the piecewise method, using the pseudocapillary model (Equations 8 and 9 from Chapter 3) before crossover, and the Rayleigh model (Equations 10 and 11 from Chapter 3) afterwards.

4.2.5 Hydrogel Stock Preparations

Type A gelatin powder (275 Bloom, Nitta Gelatin) was prepared by dissolving into PBS with continuous stirring heating and stirring to form a 100 mg/ml gelatin stock solution. Fibrinogen stock solutions of 4.0 and 8.0 mg/ml (clottable) were prepared by dissolving lyophilized bovine fibrinogen (F8630, Sigma) in phosphate buffered saline (PBS; Gibco) at 37°C. The fibrinogen solutions were filtered using a 0.2 um PVDF syringe filter. Genipin (078-03021, Wako) was dissolved in DMSO at a 200 mg/ml concentration and vortexed until fully dissolve. Microbial transglutaminase (Activa-TI, Ajinomoto) was dissolved in sterile DI water at a stock concentration of 10 Unit/ml. Bovine thrombin (T6634; Sigma) was dissolved in a sterile-filtered solution of 0.1 %w/v bovine serum albumin (Sigma) in DI water to form a 50 Unit/ml stock solution.

4.2.6 Mixed Gelapin Experiments

The 100 mg/ml gelatin solution was diluted with pre-heated PBS to generate solutions with 22, 44, 66, and 88 mg/ml gelatin concentrations. A 1:2 dilution series of the 200 mg/ml Genipin-DMSO stock solution in DMSO was performed to generate solutions with 200, 100, 50, 25, and 12.5 mg/ml genipin concentrations. 10 μL genipin solution or control DMSO was added to each well of a Syl-Off (Q2-7785, Dow) coated 96-well microplate (269620, Nunc) placed on ice. 90 uL of gelatin solution was added to using a 12-well micropipette in order to generate a combinatorial array of each gelatin and genipin concentration. An adhesive plate seal (Axygen) was applied to minimize evaporation, and the plate was cooled to 4°C for 15 minutes to rapidly form a solid gel. After cooling the plate was transferred to a 25°C water bath and longitudinal RAR measurements of each sample were immediately initiated, with automated resampling at 5-minute intervals for the first hour progressively increasing to 1-hour intervals during an 8-hour period. Plates were then transferred to a 25°C incubator. Plates were remeasured using RAR at 12-hour intervals progressing to 24 hour intervals for the final 2 days of an 8 day study.

4.2.7 Sequential Gelapin Experiments

The 100 mg/ml gelatin solution was diluted with pre-heated PBS to generate solutions with 20, 40, 60, and 80 mg/ml gelatin concentrations. 100 uL of gelatin solution was added using a 12-well micropipette in order to generate a combinatorial array of each gelatin and genipin concentration. A silicone plate seal (Fisher) was applied to minimize evaporation, and the plate was cooled to 4°C for 15 minutes to rapidly form a solid gel. After cooling, 100 uL of PBS were added to each well and the plate was resealed and transferred to a 25°C incubator. After 24 hours, the liquid was removed and RAR measurements of each sample were taken. Solutions of 10, 5, 2.5, 1.25, and 0.625 mg/ml genipin were generated by diluting the Genipin-DMSO stock solution in PBS. 100 uL of the diluted genipin solutions were add to each well of the microplate. The removal of the liquid, RAR measurement, addition of fresh solution was repeated at 12-hour increments for 3 days and then at 24 increments for the duration of a 5 day study.

4.2.8 Transglutaminase Crosslinked Gelatin Experiments

The 100 mg/ml gelatin solution was diluted with pre-heated PBS to generate solutions with 22, 44, 66, and 88 mg/ml gelatin concentrations. The 10 U/ml transglutaminase stock solution was diluted in PBS, to an array of concentrations, such that combined 1:10 with gelatin solutions they would generate final concentrations 10, 5, 2,5 1,25 0 0.625 U/gram of gelatin. 10 μL of each transglutaminase solution or control PBS was added to each well of a Syl-Off (Q2-7785, Dow) coated 96-well microplate (269620, Nunc) placed on ice. 90 uL of gelatin solution was added to using a 12-well micropipette in order to generate a combinatorial array of each gelatin and enzyme concentration. An adhesive plate seal (Axygen) was applied to minimize evaporation, and the plate was cooled to 4°C for 15 minutes to rapidly form a solid gel. After cooling the plate was transferred to a 25°C water bath and longitudinal RAR measurements of each sample were immediately initiated, with automated resampling at 5-minute intervals for the first hour

4.2.9 Fibrin Gelation Experiments

Thrombin and transglutaminase stock solutions were added to Syl-Off coated microplates such that there would be a final thrombin concentration of 100, 50, or 25 U/gram fibrinogen and a final transglutaminase concentration of 20, 10, 5, or 0 U/gram fibrinogen when combined with 100 ul fibrinogen solutions were added. After adding fibrinogen an adhesive plate seal was applied to minimize evaporation. RAR measurements were initiated exactly 60 seconds after the addition of fibrinogen to the plated enzymes and were repeated at 1-minute intervals for the first 30 minutes progressively increasing to 1-hour intervals during a 12-hour period. The plates were divided into 48 well groups that with staggered initiation times to reduce the number of samples that needed to be measured at each time point. Fibrin turbidity was measured 24 hours after the start of gelation, using a Biotek plate reader to measure absorbance at 405 nm.

4.2.10 Statistical analysis

All data is presented as mean ± standard deviation. Significant differences between fitted parameters were determined using a Student's two-tailed t-test with $\alpha = 0.05$.

4.3 Results

4.3.1 Gelatin stiffens over time

A set of gelatin solutions were prepared with concentrations of 20, 40, 60, and 80 mg/ml, and after being added to a microplate they were rapidly cooled to 4°C for 15 minutes. Following this rapid initial gelation, the plate was moved to a 25°C water bath and longitudinal multiscale RAR measurements were performed at various time intervals, beginning with 5-minute intervals for the first hour and progressively increasing to a 24-hour interval after approximately 6 days of measurement.

All gelatin samples showed a significant increase in shear modulus over the study period (Fig. 4.2A). The mean kinetic curves were fitted to a modified exponential distribution function,

$$G(T) = G_0 + (G_\infty - G_0)\left(1 - \frac{1}{\mathrm{e}^{\frac{(\mathrm{T}-\mathrm{T}_0)}{\tau}}}\right) \tag{1}$$

to quantify the initial shear modulus, G_0, final shear modulus, G_∞, lag duration before elastic increase, T_0, and time constant for growth, τ. The modeled curves are displayed alongside the experimental results as dashed black lines in Figure 4.2A, and the fitted parameters are displayed in Figure 4.2C. The initial and final shear moduli both increased significantly with each successive increase in gelatin concentration ($p < 10^{-4}$). The kinetic parameters, T_0 and τ, did not show a relationship with gelatin concentration aside from a significantly elevated time constant with the 20 mg/ml gelatin.

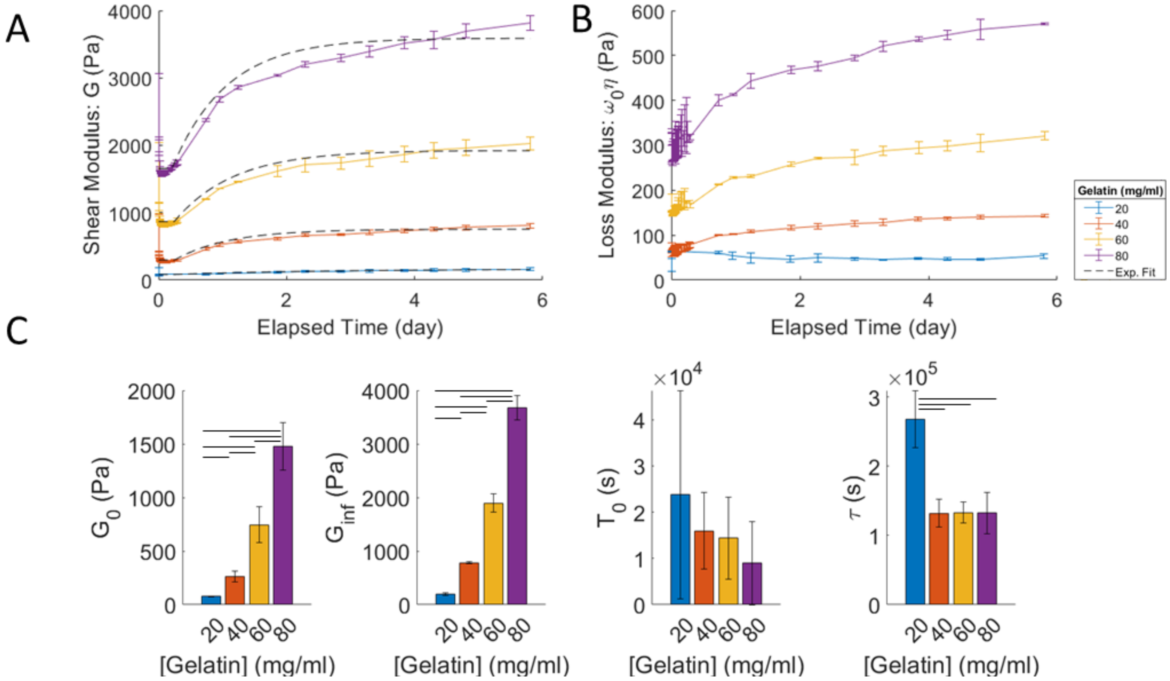

Figure 4.2: A) Shear modulus (G) and B) loss modulus ($\boldsymbol{\omega_0\eta}$) measurements of 20-80 mg/ml gelatin hydrogels collected using RAR at multiple time scales for a total of 6 days. Dashed black line represents exponential model fitting. C) Comparison of the fitted parameters, initial shear modulus ($\boldsymbol{G_0}$), final shear modulus ($\boldsymbol{G_\infty}$), lag-time (T_0), and time constant ($\boldsymbol{\tau}$). Error bars represent standard deviation of fitted parameters (n=4). Horizontal lines indicate significant differences between groups with $p < 0.05$.

4.3.2 Increasing gelatin stiffness with genipin crosslinking

The formation of genipin crosslinked gelatin, sometimes called "gelapin", has been well studied, however systematic exploration of the crosslinking kinetic has typically relied on assays to measure the number of free amines, such as a Ninhydrin assay, rather than characterizing the mechanical changes directly [11,35,36]. This approach is likely driven by the absence of high-throughput mechanical testing methods available, where common optical plate readers used for Ninhydrin assays would allow for rapid, high-throughput measurements at a variety of time scales. Here we demonstrate RAR as a mechanical testing methodology that is able to achieve a high throughput of easily repeatable non-destructive measurements, enabling mechanical measurements in longitudinal and combinatorial studies that would have not been previously possible.

A set of gelapin solutions were generated in a combinatorial method, with gelatin concentrations of 20, 40, 60, and 80 mg/ml and genipin concentrations of 1.25, 2.5, 5, 10, and 20 mg/ml, and multiscale longitudinal mechanical measurements were performed using RAR.

We observed an increase in the shear modulus, G, over time for all gelapin formulations tested (Fig. 4.3A). The shear modulus initially increased rapidly with a decreasing rate over time, appearing to asymptotically approach a maximum shear modulus. Both gelatin and genipin concentration drove significant differences in the magnitude and kinetics of the modulus growth curves, with increasing genipin concentration leading to a clear increase in the kinetics of elastic stiffening and gelatin concentration driving significant differences in both initial and final moduli.

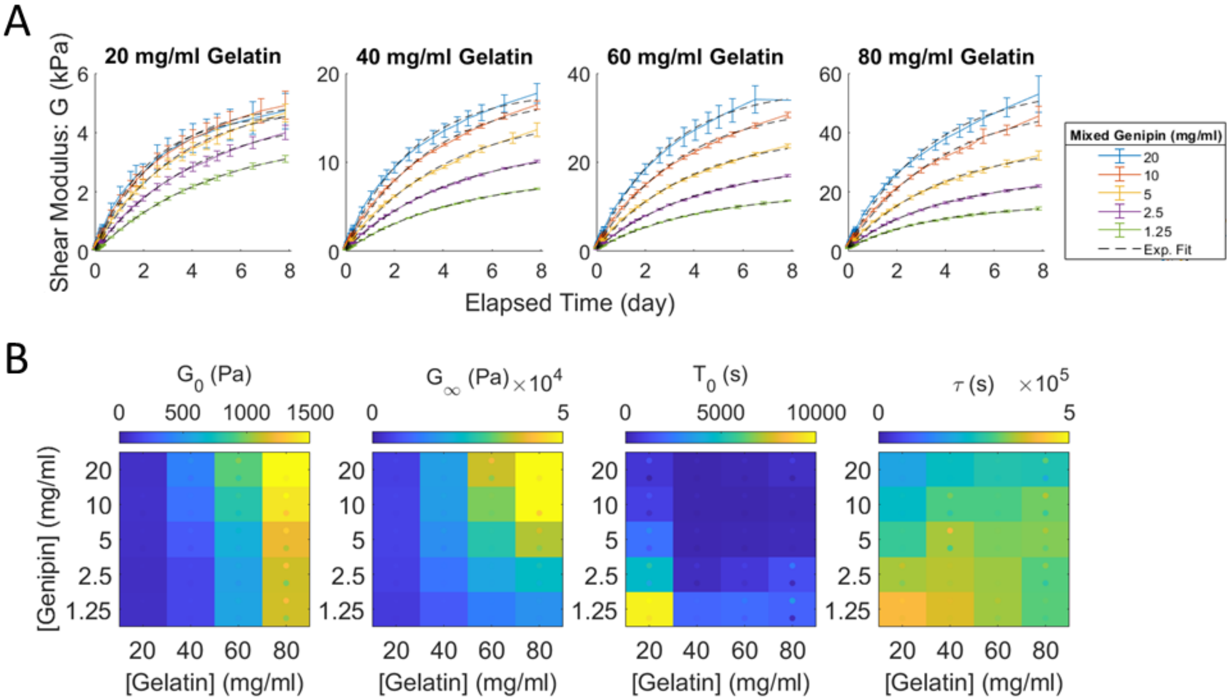

Figure 4.3: A) Shear modulus (G) of 20 to 80 mg/ml gelatin hydrogels mixed with between 1.25 and 20 mg/ml genipin and measured using RAR at multiple time scales for a total of 8 days. Dashed black line represents exponential model fitting. Error bars represent standard deviation (n=4). B) Heatmaps comparing the fitted parameters, initial shear modulus ($\boldsymbol{G_0}$), final shear modulus ($\boldsymbol{G_\infty}$), lag-time (T_0), and time constant ($\boldsymbol{\tau}$), for all combinations of gelatin and genipin concentrations. The color of each tile represents the mean parameter value (n = 4). The color of the upper and lower dots on each tile represents the parameter values one standard deviation above and below the mean, respectively.

The shear modulus kinetic curves were fitted to a modified exponential distribution function (Equation 1), and the mean fitted curves ($R^2>0.99$) are displayed alongside the experimental results as dashed black lines in Figures 4.3A. Heatmaps were generated for the fitted parameters to compare the relationship between gelatin concentration on the horizontal axis and genipin concentration on the vertical axis (Fig. 4.3B). Unsurprisingly, a clear increase in G_0 and G_∞ is visible with increasing gelatin concentration at any genipin concentration, as was seen in the control (Fig. 4.2C). There is a dramatic and significant increase in G_∞ between samples with genipin and those without ($p < 10^{-5}$), however, the relationship between G_∞ and genipin concentration in the gelapin samples is more complex. At higher gelatin concentrations (40 through 80 mg/ml) we observed significant increases in G_∞ with increasing genipin for all concentrations except 20 mg/ml genipin ($p < 0.05$), but at lower gelatin concentrations we no longer see significant differences between the genipin concentrations above 5 mg/ml ($p > 0.1$). There is a slight reduction in the mean G_∞ for 20 mg/ml gelatin with 20 mg/ml genipin, compared to 10 mg/ml genipin, indicating that excessive genipin concentrations may inhibit the stiffening effect of crosslinking. However, this reduction was not significant ($p = 0.25$).

The remaining parameters, T_0 and τ, describe the kinetics of the mechanical change due to crosslinking (Fig. 4.3B). For samples with genipin, there is a slight gradient across the heatmap, with the lag time decreasing with genipin concentration. The lag time for the 20 mg/ml gelatin was significantly higher than other gelatin concentrations for all but the 20 mg/ml genipin concentration ($p < 0.05$). However, average duration of this lag phase, ~2hrs, is small compared to the total duration of the nearly 200 hour study. The final parameter, tau, is the time constant and is inversely related to the slope of the curve, with greater values indicating a slower growth rate (Fig. 4.3B). For samples of gelatin with genipin we see a saddle distribution, where low gelatin and high genipin concentrations or high gelatin and low genipin both have reduced time constant values compared to samples where genipin and gelatin concentrations are either both high or both low. This pattern may indicate that we are seeing a reduced time constant in situation where the reaction is limited by either a low concentration of the crosslinker relative to the substrate or vice-versa.

4.3.3 Sequential addition of genipin to gelatin scaffolds

Genipin is also commonly used for the stabilization of hydrogel scaffolds after the formation of a solid gel. This requires the solid, uncrosslinked gels to be immersed in an aqueous solution containing genipin. Genipin is then able to diffuse through the porous matrix and react with free amines. As above, we performed a combinatorial study, measuring the temporal changes in 20, 40, 60, and 80 mg/ml gelatin hydrogels that were soaked in PBS containing genipin at concentrations between 0 and 10 mg/ml. Tracking the evolving shear modulus over time, we saw a substantial increase in the gel elasticity following the addition of genipin (Fig. 4.4A). Trends in the magnitude and kinetics of these curves showed similar concentration trends with the mixed gelatin and genipin, but the shape of the modulus growth curves differed significantly for the sequential addition of genipin. The sequential addition resulted in a sigmoidal kinetic profile, with the elastic growth rate starting slow, rising to a maximum at the curves inflection point and then declining as the modulus approached a maximum value.

The exponential distribution function (Equation 1) assumes that the maximum kinetic rate occurs at the beginning, and while this was true for the mixed gelapin, this assumption does not hold for the sequential crosslinking. The logistic function,

$$G(T) = G_0 + (G_\infty - G_0)\left(1 - \frac{1}{1+e^{\frac{(T-T_0)}{\tau}}}\right) = G_0 + \frac{(G_\infty - G_0)}{1+e^{\frac{-(T-T_0)}{\tau}}} \qquad [2]$$

is similar in appearance to exponential distribution function, but is an odd function, and therefore reaches horizontal asymptotes in both the positive and negative directions. This function better captures the growth curve for the sequential genipin crosslinking with each fitted $R^2 > 0.99$. It is important to note that while G_∞ can be compared directly between the models, T_0 and τ magnitudes will differ and should not be directly compared. We were unable to generate measurable surface perturbations in 60 and 80 mg/ml gelatin with 5 or 10 mg/ml genipin after 2 days of crosslinking due to the significant increase in stiffness and were therefore unable to include these materials in the logistic fitting.

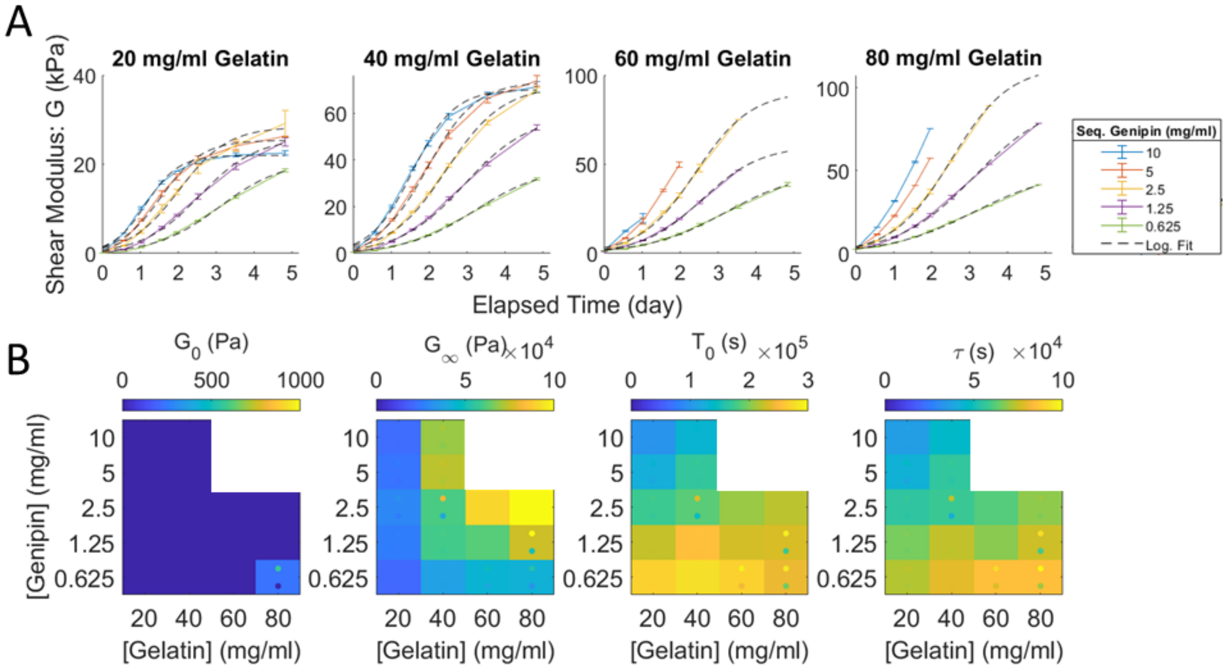

Figure 4.4: A) Shear modulus (G) of 20 to 80 mg/ml gelatin hydrogels that were allowed to solidify for 24 hours and then were covered in genipin solutions between 0.625 and 10 mg/ml and measured longitudinally using RAR for a total of 5 days. Dashed black line represents logistic model fitting. Error bars represent standard deviation (n=4). B) Heatmaps comparing the fitted parameters, initial shear modulus ($\boldsymbol{G_0}$), final shear modulus ($\boldsymbol{G_\infty}$), lag-time (T_0), and time constant ($\boldsymbol{\tau}$), for all combinations of gelatin and genipin concentrations. The color of each tile represents the mean parameter value (n = 4). The color of the upper and lower dots on each tile represents the parameter values one standard deviation above and below the mean, respectively.

As with the mixed gelapin, heatmaps were generated to compare the fitted logistic parameters with varying gelatin and genipin concentrations (Fig. 4.4B). Compared to mixed gelapin, the sequential genipin had significantly greater final moduli for all formulations, with the highest G_∞ for the 20 and 40 mg/ml gelatin being more than 4-fold greater with sequential genipin addition. G_∞ increased with increasing gelatin concentration for all genipin concentrations (Figure 4D), however only some differences between successive concentrations were significant. There is significant increase in G_∞ with the addition of genipin ($p < 0.005$), however the relationship with genipin concentration is not strictly monotonic. The maximum G_∞ for 20 and 40 mg/ml gelatin occurred at 2.5 and 5 mg/ml genipin respectively, with decreasing moduli for higher or lower doses.

The time delay before the maximum rate of elastic growth, T_0, showed a decreasing trend with increasing genipin concentration at 20 and 40 mg/ml gelatin concentrations with significant differences between successive genipin concentrations ($p < 0.05$). There was no consistent trend with gelatin concentration (Fig. 4.4B). The time constant, τ, also showed a clear decreasing trend with increasing genipin concentration, although this was also only significant at lower gelatin concentrations ($p < 0.05$) (Fig. 4.4B).

4.3.4 Enzymatic crosslinking of gelatin using transglutaminase

In addition to bifunctional crosslinkers like genipin or glutaraldehyde that form the link between amino acids, enzymes, such as transglutaminase, can catalyze the direct covalent crosslinking of functional groups on amino acids. We combined microbial transglutaminase with the same gelatin concentrations used above, keeping enzyme concentrations proportional to the gelatin concentration ranging from 0 to 10 Units/g of gelatin. Samples were prepared and RAR measurements were performed as with the mixed gelapin samples.

The shear modulus increased monotonically for all samples tested (Fig. 4.5A) with significant differences between the kinetics and final moduli. The elastic growth curves were quantified using the modified exponential distribution function (Equation 1), generating heatmaps for each modeled parameter comparing gelatin and enzyme concentrations (Fig. 4.5B). We saw significant increases in G_0 and G_∞ with increasing gelatin concentration ($p < 0.05$), but only G_∞ increased with increasing transglutaminase concentration (Fig. 4.5B). While transglutaminase crosslinking led to a significant increase in G_∞ compared to the base gelatin, it was comparatively weaker than gelapin formulations. The maximum fitted G_∞ of transglutaminase crosslinked gelatin was less than 20 kPa, substantially softer than maximum G_∞ of the mixed and sequential gelapins which were greater than 50 kPa and 100 kPa, respectively.

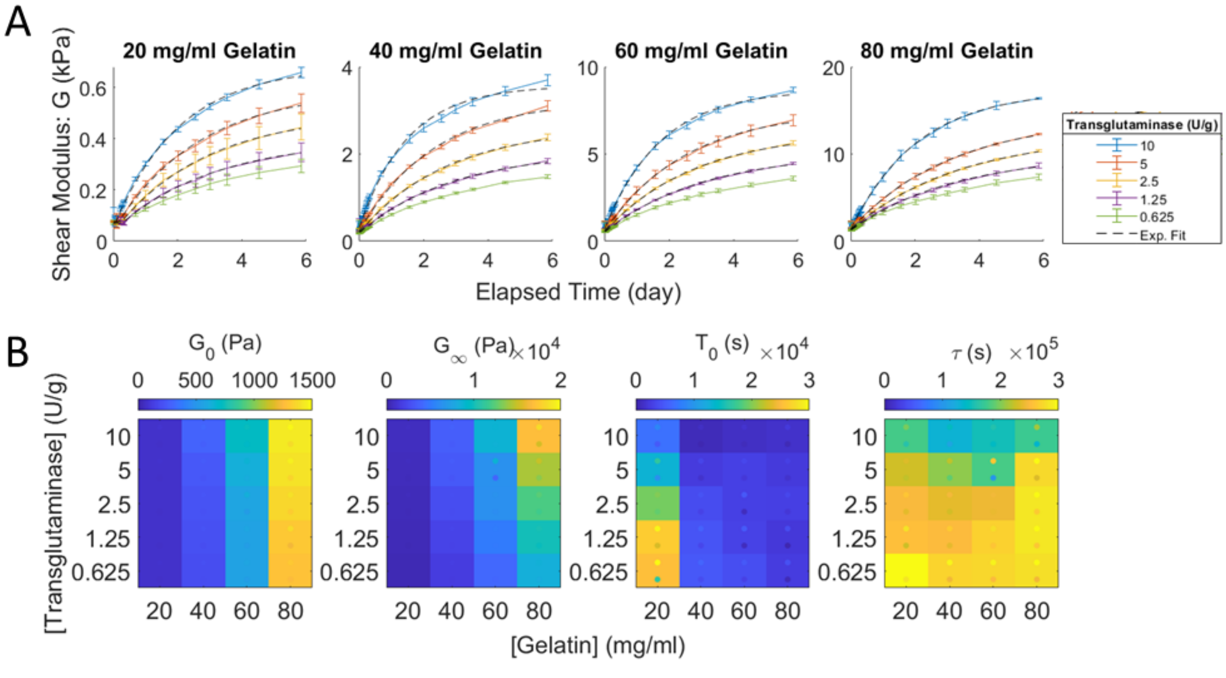

Figure 4.5: A) Shear modulus (G) of 20 to 80 mg/ml gelatin hydrogels mixed with between 0.625 and 10 U/g of transglutaminase and measured using RAR at multiple time scales for a total of 6 days. Dashed black line represents exponential model fitting. Error bars represent standard deviation (n=4). B) Heatmaps comparing the fitted parameters, initial shear modulus ($\boldsymbol{G_0}$), final shear modulus ($\boldsymbol{G_\infty}$), lag-time (T_0), and time constant ($\boldsymbol{\tau}$), for all combinations of gelatin and genipin concentrations. The color of each tile represents the mean parameter value (n = 4). The color of the upper and lower dots on each tile represents the parameter values one standard deviation above and below the mean, respectively.

The elastic growth kinetics for transglutaminase crosslinking were comparable to those of the mixed gelapin hydrogels. Both crosslinking additions led to a decrease in T_0 with increasing concentration. We also observed a significantly elevated lag duration with the 20 mg/ml gelatin formulations, relative to other concentrations ($p < 0.005$). As expected, the time constant showed a strong negative correlation with the transglutaminase concentration, but did not show a consistent effect when compared to gelatin concentration.

4.3.5 Viscous changes with gelatin crosslinking

The covalent crosslinking of gelatin hydrogels had a substantial impact on the measured viscous properties of these hydrogels. The loss modulus, $\omega_0\eta$, was tracked over time using RAR for the gelatin samples crosslinked using either genipin, both mixed and sequential additions, and transglutaminase (Fig. 4.6A-C). The loss modulus generally increased with crosslinking for gelapin formulations relative to an uncrosslinked control (Fig. 4.2B). The loss modulus for mixed gelapin at both high genipin and/or low gelatin concentrations was observed to initially decrease rapidly with increasing genipin concentrations driving a more rapid decrease and a lower minimum shear modulus (Fig. 4.7). This reduction was temporary with the loss modulus steadily increasing over the duration of the study, eventually reaching, or exceeding, the initial and baseline gelatin values (Fig. 4.6A). This initial decrease in loss modulus was most prominent in the 20 mg/ml gelatin samples, where the loss modulus decreases as much as 80% in just a few hours, before slowly increasing over the subsequent week (Fig. 4.7). We also observed an increase in final loss modulus with increasing mixed genipin concentration, with higher genipin concentration reaching values significantly higher than baseline all but the 20 mg/ml gelatin. Unlike the mixed gelapin, the sequential genipin crosslinking did not result in a temporary reduction in measured viscosity, instead displaying a sigmoidal increase over time, with final loss moduli significantly greater than the uncrosslinked gelation for all genipin and gelatin concentrations (Fig. 4.6B).

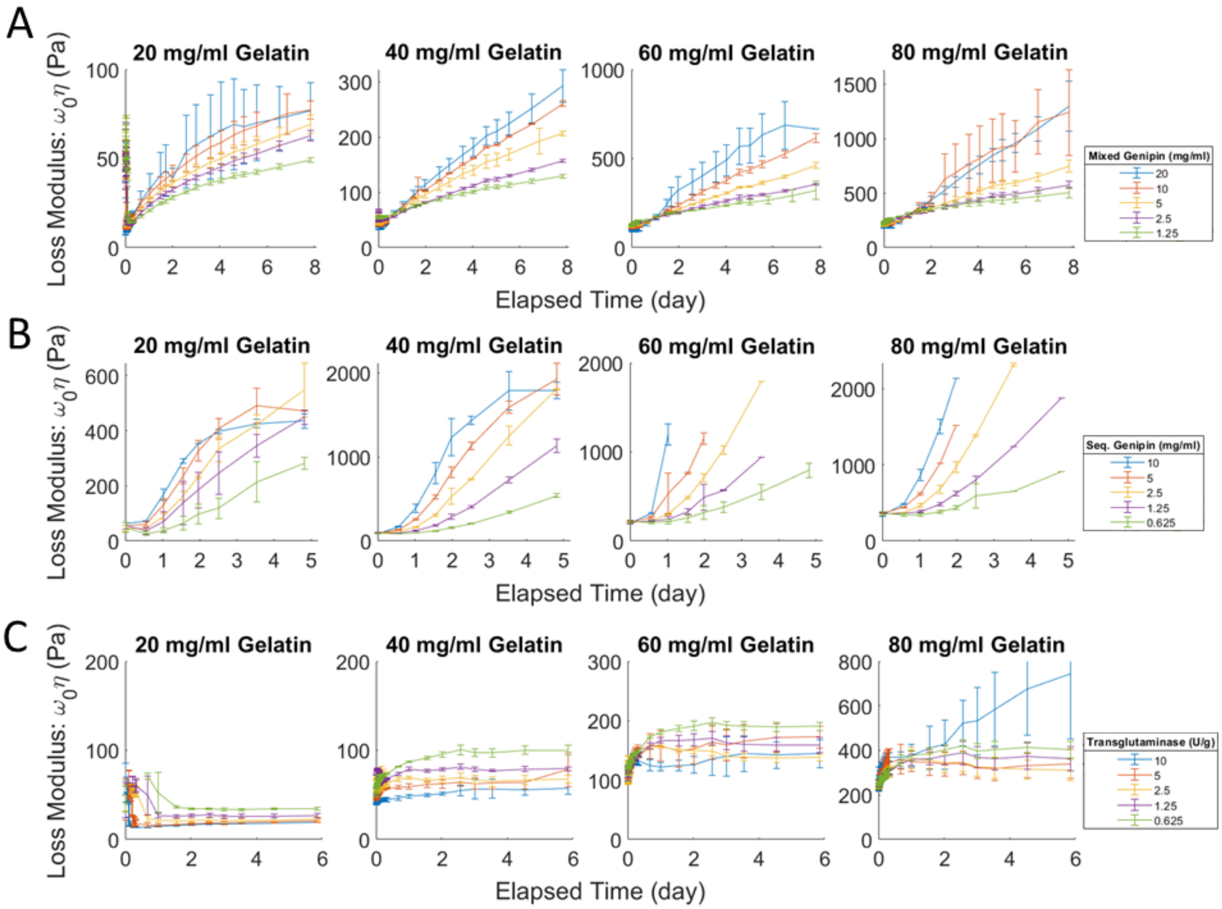

Figure 4.6: Loss modulus ($\omega_0\eta$) measurements of 20 to 80 mg/ml gelatin hydrogels A) mixed with genipin, B) soaked in a genipin solution, or C) missed with transglutaminase and measured using RAR at multiple time scales for a minimum of 5 days. Error bars represent standard deviation (n=4).

Unlike the gelapin samples, where increased genipin led to a higher terminal viscosity, the increases in transglutaminase concentration resulted in a reduction in the loss modulus (Figure 6C). The loss modulus for gelatin with low concentrations of transglutaminase was similar to the base gelatin in both magnitude and kinetics showing a slight initial increase, or decrease in the case of 20 mg/ml gelatin, and reaching a plateau after a few days (Fig. 4.2B). Additional transglutaminase led to a negative shift in the loss modulus curves, with the one exception being the 80 mg/ml gelatin with 10 U/g transglutaminase resulting in a dramatic increase in loss modulus over time, more like the gelapin samples.

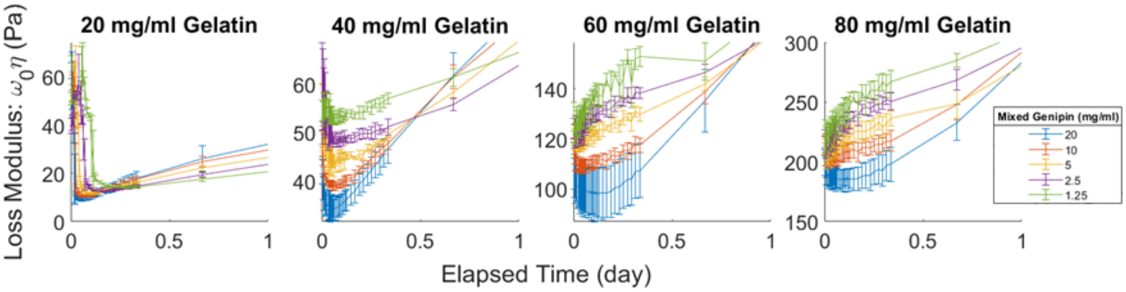

Figure 4.7: Rapid changes in the loss modulus ($\boldsymbol{\omega_0\eta}$) were observed over the first day of crosslinking for the mixed gelapin gels. Error bars represent standard deviation (n=4).

4.3.6 Combinatorial effects of thrombin and transglutaminase during fibrinogenesis

Unlike the thermal gelation of gelatin, fibrin gels require a proteolytic enzyme, commonly thrombin, to cleave the fibrinopeptides from fibrinogen and enable the self-assembly of protofibrils and their lateral aggregation into the fibrous structure of the hydrogel. These macromeric structures can be further stabilized via enzyme catalyzed covalent crosslinking. We tracked dynamic viscoelastic properties in combinatorial set of fibrin gels produced from fibrinogen (4 or 8 mg/ml), thrombin (25, 50, or 100 U/g fibrinogen), and transglutaminase (0, 5, 10, or 20 U/g fibrinogen). While gelatin hydrogels were solid at the beginning of the dynamic study, fibrin gels were initially in a liquid phase, transitioning to a solid phase within 30 minutes of transglutaminase and thrombin addition. This phase change was identified in the resonant parameters extracted from measured surface oscillations with an observable discontinuity in the frequency and a temporary local maximum in the damping coefficient that indicate the shift from pseudocapillary to Rayleigh surface waves (Fig. 4.8A-B). This phenomenon has been discussed in much greater detail in Chapter 3 of this dissertation.

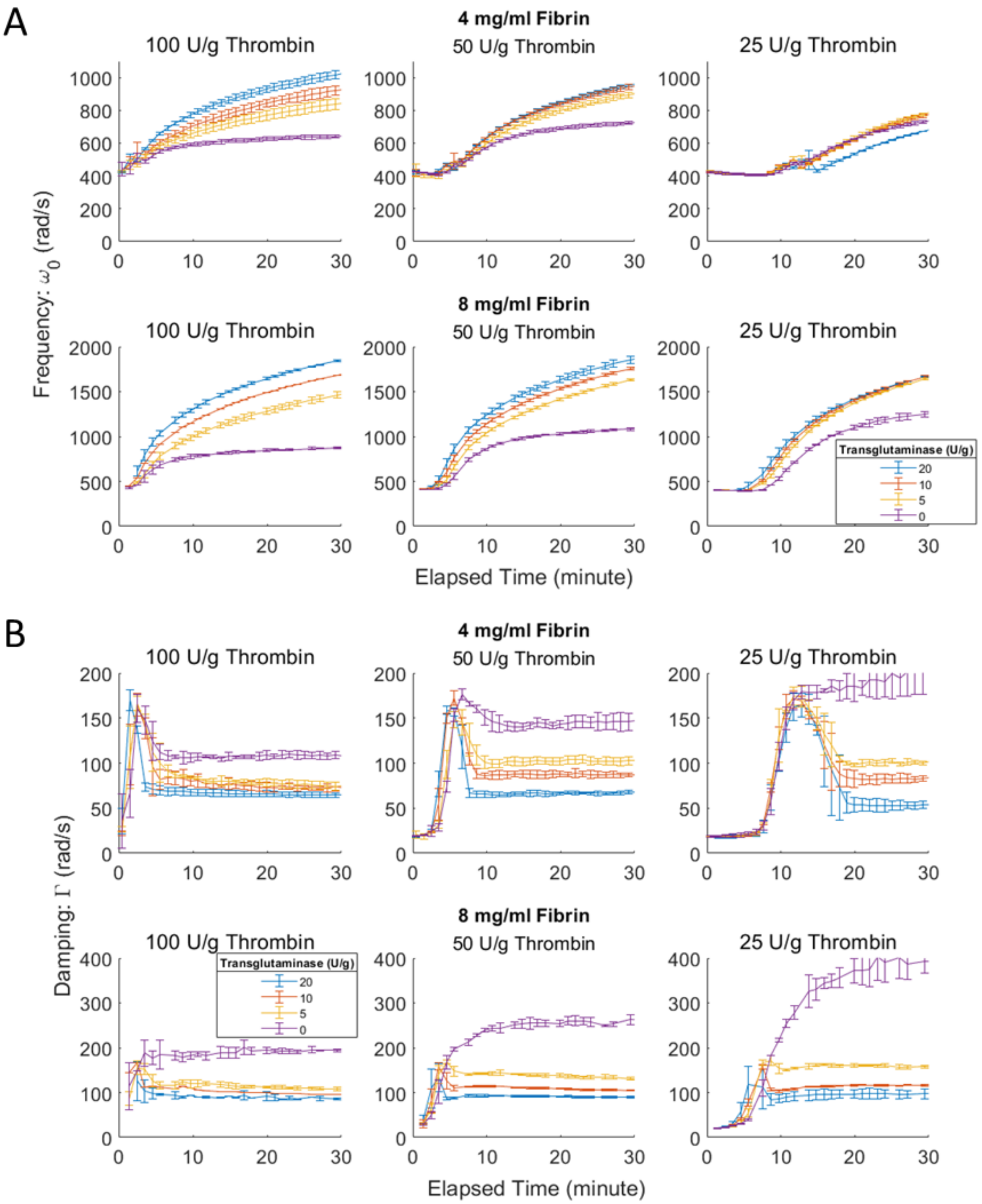

Figure 4.8: Dynamic RAR measurements of A) natural frequency ($\boldsymbol{\omega_0}$) and B) damping coefficient ($\boldsymbol{\Gamma}$) extracted during gelation of 4 and 8 mg/ml fibrin gels formed with between 25 and 100 U/g thrombin and between 0 and 20 U/g transglutaminase. Discontinuity in the frequency and the temporary peak in damping are indicative of the phase transition during fibrinogenesis. Error bars represent standard deviation (n=4).

The dynamic shear modulus was calculated using a piecewise function for time points before or after the phase transition for all fibrin formulations (Fig. 4.9A). The elastic growth curves

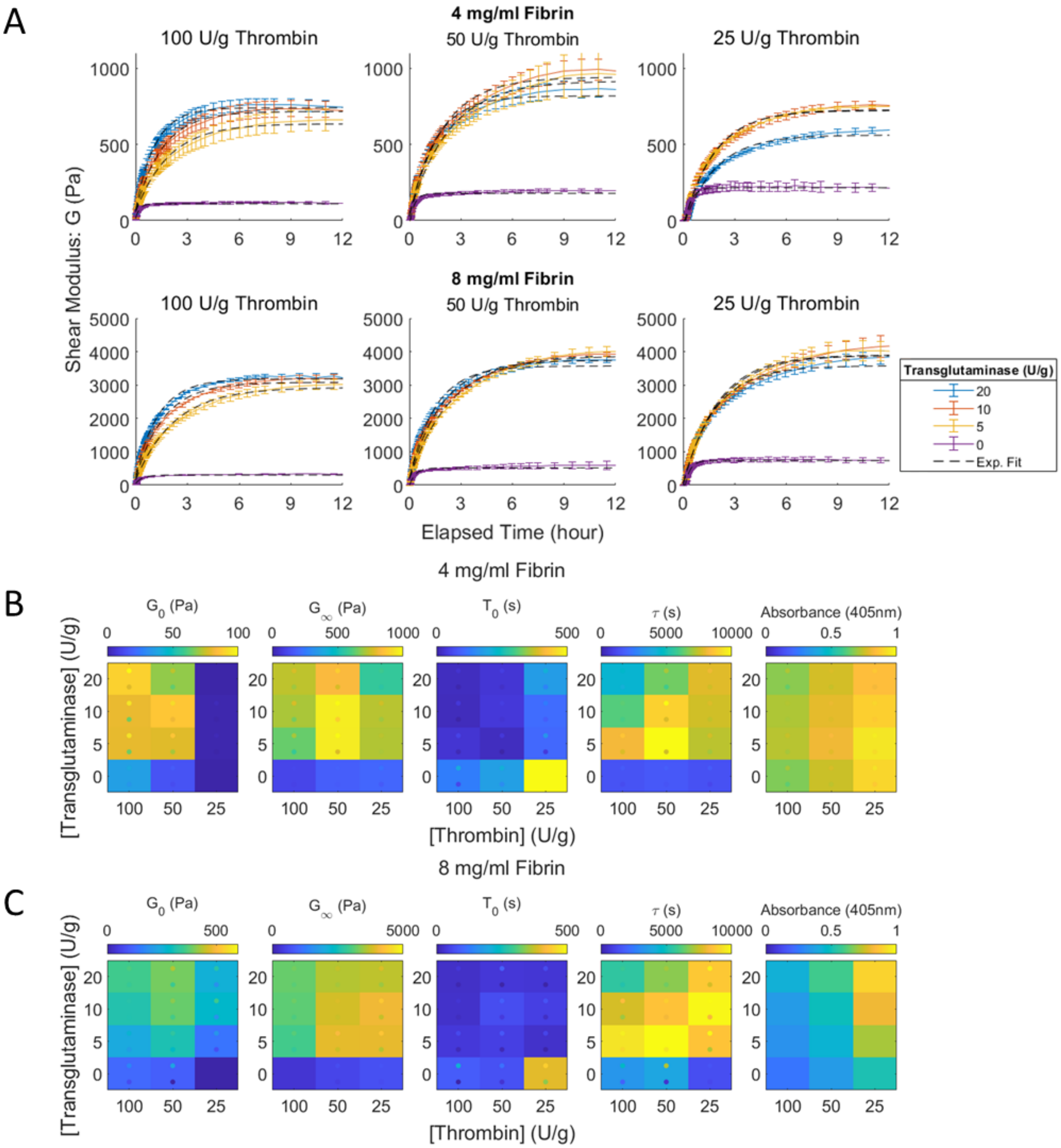

Figure 4.9: A) Shear modulus (G) of 4 and 8 mg/ml fibrin gels formed with between 25 and 100 U/g thrombin and between 0 and 20 U/g transglutaminase and measured using RAR at multiple time scales for a total of 12 hours. Dashed black line represents exponential model fitting. Error bars represent standard deviation (n=4). Heatmaps compare the fitted parameters, initial shear modulus ($\boldsymbol{G_0}$), final shear modulus ($\boldsymbol{G_\infty}$), lag-time (T_0), and time constant ($\boldsymbol{\tau}$), as well as absorbance for all combinations of thrombin and transglutaminase concentrations in B) 4 mg/ml and C) 8 mg/ml fibrin gels. The color of each tile represents the mean parameter value (n = 4). The color of the upper and lower dots on each tile represents the parameter values one standard deviation above and below the mean, respectively.

were quantified using the modified exponential growth function (Equation 1). We would expect the initial shear modulus, G_0, to be zero for a fibrinogen solution before the enzyme mediated gelation. The fitted values, however, showed a non-zero G_0 for fibrin samples with elevated thrombin and transglutaminase concentrations, indicating that there may be some formation of an elastic network during the 60 second period before measurements could be initiated (Figure 4.9B-C). The final shear modulus, G_∞, showed effects due to the concentration of all three gel components. An increased fibrin concentration resulted in a significant increase to G_∞ for any set of enzyme concentrations ($p < 0.0005$). A reduction in thrombin concentration from 100 U/g to 50 U/g resulted in an increased G_∞ for all fibrin and transglutaminase concentration ($p < 0.05$). However, further reduction to 25 U/g thrombin concentration only significantly increased the shear modulus for uncrosslinked 8 mg/ml fibrin. There was a decrease in G_∞ for the crosslinked 4 mg/ml fibrin samples at the lowest thrombin concentration, and this reduction was significant for samples with 10 U/g transglutaminase or more ($p < 0.005$). The 4 mg/ml fibrin gel with 25 U/g thrombin and 20 U/g transglutaminase had a significantly lower G_∞ than all crosslinked 4 mg/ml fibrin samples ($p \leq 0.005$) except for the 100 U/g thrombin and 5 U/g transglutaminase composition.

The lag duration, T_0, generally decreased with increasing thrombin and transglutaminase. The uncrosslinked fibrin samples reached a stable maximum elasticity within 5 hours, and, as a result, has lower values of τ compared to all crosslinked fibrins with significant differences ($p < 0.05$) between the uncrosslinked time constants and all comparable crosslinked time constants except the 8 mg/ml with 20 U/g transglutaminase and 50 or 100 U/g thrombin. The time constant increased with a reduction in thrombin concentration from 100 U/g to 50 U/g and decreased with increasing transglutaminase concentrations at these thrombin levels.

In addition to the fitted parameters derived from mechanical RAR measurements, we also measured the optical absorbance of these samples at 450nm, as the optical properties of fibrin gels have been identified as important indicators of gel microstructure [31]. Turbidity increased with decreasing fibrin concentration and with decreasing thrombin concentration (Fig. 4.9B-C). Turbidity also increased with increasing transglutaminase concentration in the 8 mg/ml fibrin gels, but only increased with a transglutaminase increase from 0 to 5 U/g in 4 mg/ml fibrin gels, with the absorbance decreasing with transglutaminase concentration above this point.

4.3.7 Viscous changes in fibrin gels

The dynamic loss modulus measured in fibrin gels increased rapidly following the addition of thrombin, reaching a stable plateau before the end of the 12 hour study (Fig. 4.10). The reduction of thrombin. The loss modulus for crosslinked fibrin gels did not vary as substantially

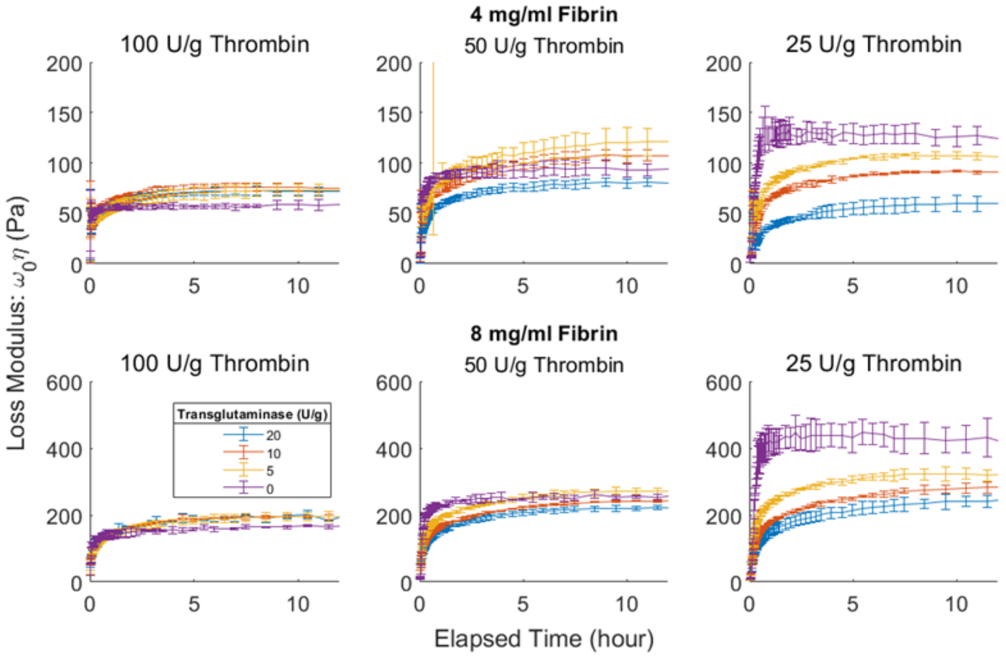

Figure 4.10: Loss modulus ($\omega_0\eta$) measurements of 4 and 8 mg/ml fibrin gels formed with between 25 and 100 U/g thrombin and between 0 and 20 U/g transglutaminase and measured using RAR at multiple time scales for a total of 12 hours. Error bars represent standard deviation (n=4).

with thrombin concentration, resulting in a relative increase in loss modulus for crosslinked gels, compared to uncross linked fibrin, at 100 U/g thrombin and a relative decrease at 25 U/g thrombin. Additionally, at lower thrombin concentrations the loss moduli values differed significantly with transglutaminase concentration, showing a negative correlation with the enzyme.

4.4 Discussion

4.4.1 Temporal changes in gelatin microstructure

Gelatin rapidly forms a solid gel when cooled below a threshold value, typically ~37C, this transition occurs rapidly as the flexible polymer chains in solution undergo intramolecular crosslinking and form a helical structure [15]. While the gel will become solid after a certain proportion of polymer chains undergo conversion, this process has been reported to continue for hundreds and even thousands of hours, potentially indefinitely [32]. Our RAR measurements, tracking gelatin mechanical properties over ~150 hours (Fig. 4.2A), clearly showed this continual monotonic increase in the gel elasticity and viscosity, confirming that the tertiary protein structure continued to evolve for the duration of the study.

The addition of genipin led to the formation of intermolecular crosslinks between polymer chains. Gelapin gels have been demonstrated to be more stable than plain gelatin, both to thermal and proteolytic degradation [33]. This crosslinking may also impact the ability for gelatin peptides to undergo the transition to a helical structure, reducing the maximum possible elasticity [15]. Our results have shown that the maximum shear moduli for some low concentration gelatins are reduced with genipin concentrations above some threshold value (Fig. 4.3B and 4.4B). These samples have the highest genipin concentration relative to gelatin concentration, increasing the likelihood that these rapidly forming crosslinks inhibit the gels conformational flexibility. This reduction of conformational flexibility may also play a role in the increased mechanical strength of the sequential gelapin. These samples were allowed to gel for 24 hours prior to genipin addition, which can be a critical period in the helix formation [34], providing additional time for development of a helical structure before any genipin constraints were introduced. In addition to the nanoscale conformational changes, previous studies have identified microscale differences in lyophilized gelapin formed using a mixed or sequential protocol, with the sequential gel exhibiting a smaller pore structure [35]. Unlike this study, where genipin crosslinking was monitored mechanically, most studies quantify the kinetics of this reaction using a Ninhydrin assay to quantify the remaining free amino groups [13,33,35,36]. While this does give an indication of the reaction progress, it does not provide any information of the resulting structure, potentially missing the substantive mechanical differences we observed in gels formed with different concentrations or sequences of genipin addition. In further work we may compare these chemical crosslinking assays to the mechanical determination of crosslinking demonstrated using RAR.

Microbial transglutaminases provide an alternative method for the stabilization of fibrous protein hydrogels, like gelatin or fibrin, through the formation of covalent bonds between the carboxamide and amine functional groups of glutamine and lysine [37]. These crosslinks, like those from genipin, have been demonstrated to reduce the confirmation flexibility of gelatin microstructure, increasing the thermal stability, while reducing the potential for subsequent helices formation [38]. We did not see a reduction in final shear modulus with increasing transglutaminase concentration at any gelatin concentration, but this may be due to the maximum concentration, 10 U/g, and temperature, 25C, used in these experiments resulting in an insufficient reaction rate to interfere with the intrinsic gelatin restructuring or not reaching crosslinking completion to a degree there the tertiary polymer structure has a significant impact (Fig 4.5B).

4.4.2 Enzymatic competition during fibrinogenesis

We observed a complex interplay between thrombin and transglutaminase concentrations during the formation of fibrin gels. We measured clear reduction in the shear modulus for crosslinking gels generated using higher thrombin concentrations. The inverse relationship between thrombin concentration and elastic modulus has been reported previously [39,40]. In addition to mechanical differences, numerous studies have explored the microstructural differences in fibrin gels [39–43], observing that higher thrombin concentration leads to a "fine" clot with a high density of thin fibers, while a low thrombin density results in a "coarse" clot with thicker fibers and fewer branching points.

Factor XIII, a transglutaminase involved the mammalian coagulation cascade, has a critical role in increasing the elasticity and stability of blood clots, and has been reported partially mediate this effect through of fiber compaction [44,45]. The RAR testing clearly demonstrated the mechanical impact of this enzymatic fibrin modification, showing dramatically increase moduli with and transglutaminase addition. However, our results did not show a monotonic dose dependence of transglutaminase, with increasing dose increasing elasticity in high thrombin gels and decreasing elasticity in low thrombin gels (Fig 4.9B). Elevated transglutaminase concentrations relative to thrombin was shown to negatively impact the ultimate shear modulus of the fibrin gels (Fig 4.9B-C), likely due to the premature crosslinking of fibrinogen and fibrin monomers before they can fully assemble into the ordered protofibril and fiber structure [46]. This result illustrates the importance of reaction kinetics during fibrin coagulation, with the sequence of proteolytic, aggregating, and cross-linking steps directly impacting the microstructure and mechanics of the final gel.

The optical absorbance of fibrin clot is known to increase with fiber diameter [41], and our turbidity measurements therefore help to confirm the reciprocal relationship between thrombin concentration and fiber diameter in our study, showing a clear decrease in absorbance with increasing thrombin concentration (Fig 4.9B-C). Counterintuitively, there was also a reduction in absorbance increased fibrin concentration, demonstrating that the initial fibrinogen concentration but may impact not only the overall fiber density but the structure of individual fibers [47]. Interestingly, we would have also expected to also see a decrease in in turbidity with increasing transglutaminase, indicating further decreases in fiber diameter. While we did observe this dose dependence in the 4 mg/ml fibrin, we saw an inverse trend in the 8 mg/ml fibrin. This may be explained by other microstructural changes, aside from fiber diameter, that are altered by transglutaminase and impact turbidity [31] but will need confirmation using SEM to make any definitive conclusions.

4.5 Conclusions

The mechanical properties of soft biomaterials are critical to their function. Extensive research has been done to understand the role of physical material properties, such as elasticity, viscosity, and porosity, in driving cellular phenotype. This type of information is incredibly important to the field of tissue engineering, helping to identify hydrogels that can effectively operate as synthetic ECM. As demonstrated in this study, the mechanical and structural properties of hydrogels depend on a wide variety of compositional and environmental factors, including those we examined, such polymer concentration and structural stabilization through crosslinking, and many we did not, like temperature, pH, or ionic strength. Understanding the how these definable parameters influence material properties both individually and synergistically will require the implementation of combinatorial methods in biomaterials research [16].

An important requirement for the expansion of combinatorial studies for biomaterial is the development of high-throughput methods for both the fabrication and characterization of soft biomaterials. While limitations in production throughput may be addressed using automated liquid handling platforms or microfluidic systems, there are no readily available tools for high throughput mechanical characterization at the scale required for combinatorial studies. In this study we have demonstrated the capability of RAR to measure the mechanical properties in hydrogels with shear moduli ranging from below 50 Pa to greater than 50 kPa. Additionally, leveraging the non-destructive nature of ultrasonic pulses these measurements were repeated with a temporal resolution as small as one minute for longitudinal studies lasting up to a week. All of the experimental data used in this study, over 15,000 individual viscoelastic measurements performed on 352 samples with 88 distinct material composition, was collected in a single 15 day period on a single experimental platform by a single researcher. From these results, we were able to gain insight into the mechanical and microstructural differences between gelatin and fibrin hydrogels with and without the addition of chemical and enzymatic crosslinkers. While many of the composition-structure relationships identified are not novel, the ease with which they could be generated was.

Future work with RAR will involve the implementation of machine learning tools to utilize the types of multiparametric compositional – mechanical relationships to optimize hydrogel design. This capability could have significant impact in the field of tissue engineering, enabling the intelligent design of materials to better control cellular behavior and replicate native tissue. Additionally, the multiscale dynamic mechanical information that is unique to RAR experiments can be used to help design materials where the kinetics of gelation and temporal evolution of mechanical properties are critical to their function, such as hydrogel based surgical sealants, bioinks for 3D bioprinting, and degradable scaffolds for drug delivery. With ability to perform mechanical characterization with the speed and convenience of a plate reader, RAR has the potential to transform material optimization from costly and time-intensive academic exercise to a fundamental step in every biomaterial workflow.

4.6 References

[1] A.J. Engler, S. Sen, H.L. Sweeney, D.E. Discher, Matrix Elasticity Directs Stem Cell Lineage Specification, Cell. 126 (2006) 677–689. https://doi.org/10.1016/j.cell.2006.06.044.

[2] D.E. Discher, D.J. Mooney, P.W. Zandstra, Growth factors, matrices, and forces combine and control stem cells., Science (80-.). 324 (2009) 1673–7. https://doi.org/10.1126/science.1171643.

[3] A.R. Cameron, J.E. Frith, G.A. Gomez, A.S. Yap, J.J. Cooper-White, The effect of time-dependent deformation of viscoelastic hydrogels on myogenic induction and Rac1 activity in mesenchymal stem cells, Biomaterials. 35 (2014) 1857–1868. https://doi.org/10.1016/j.biomaterials.2013.11.023.

[4] O. Chaudhuri, L. Gu, D. Klumpers, M. Darnell, S.A. Bencherif, J.C. Weaver, N. Huebsch, H.P. Lee, E. Lippens, G.N. Duda, D.J. Mooney, Hydrogels with tunable stress relaxation regulate stem cell fate and activity, Nat. Mater. 15 (2016) 326–334. https://doi.org/10.1038/nmat4489.

[5] B. Trappmann, J.E. Gautrot, J.T. Connelly, D.G.T. Strange, Y. Li, M.L. Oyen, M.A. Cohen Stuart, H. Boehm, B. Li, V. Vogel, J.P. Spatz, F.M. Watt, W.T.S. Huck, Extracellular-matrix tethering regulates stem-cell fate, Nat. Mater. 11 (2012) 642–649. https://doi.org/10.1038/nmat3339.

[6] M.S. Hall, F. Alisafaei, E. Ban, X. Feng, C.-Y. Hui, V.B. Shenoy, M. Wu, Fibrous nonlinear elasticity enables positive mechanical feedback between cells and ECMs, Proc. Natl. Acad. Sci. U. S. A. 113 (2016) 14043–14048. https://doi.org/10.1073/pnas.1613058113.

[7] D.L. Matera, W.Y. Wang, M.R. Smith, A. Shikanov, B.M. Baker, Fiber Density Modulates Cell Spreading in 3D Interstitial Matrix Mimetics, ACS Biomater. Sci. Eng. 5 (2019) 2965–2975. https://doi.org/10.1021/acsbiomaterials.9b00141.

[8] S.L. Vega, M.Y. Kwon, K.H. Song, C. Wang, R.L. Mauck, L. Han, J.A. Burdick, Combinatorial hydrogels with biochemical gradients for screening 3D cellular microenvironments, Nat. Commun. 9 (2018) 1–10. https://doi.org/10.1038/s41467-018-03021-5.

[9] M.S. Weiss, B.P. Bernabe, A. Shikanov, D.A. Bluver, M.D. Mui, S. Shin, L.J. Broadbelt, L.D. Shea, The impact of adhesion peptides within hydrogels on the phenotype and signaling of normal and cancerous mammary epithelial cells, Biomaterials. 33 (2012) 3548–3559. https://doi.org/10.1016/j.biomaterials.2012.01.055.

[10] J.A. Beamish, B.A. Juliar, D.S. Cleveland, M.E. Busch, L. Nimmagadda, A.J. Putnam, Deciphering the relative roles of matrix metalloproteinase- and plasmin-mediated matrix degradation during capillary morphogenesis using engineered hydrogels, J. Biomed. Mater. Res. - Part B Appl. Biomater. (2019) 1–10. https://doi.org/10.1002/jbm.b.34341.

[11] P.A. Turner, J.S. Thiele, J.P. Stegemann, Growth factor sequestration and enzyme-mediated release from genipin-crosslinked gelatin microspheres, J. Biomater. Sci. Polym. Ed. 28 (2017) 1826–1846. https://doi.org/10.1080/09205063.2017.1354672.

[12] N.J. Walters, E. Gentleman, Evolving insights in cell-matrix interactions: Elucidating how non-soluble properties of the extracellular niche direct stem cell fate, Acta Biomater. 11 (2015) 3–16. https://doi.org/10.1016/j.actbio.2014.09.038.

[13] S.E. Sakiyama-Elbert, J. a Hubbell, Development of fibrin derivatives for controlled release of heparin-binding growth factors., J. Control. Release. 65 (2000) 389–402. https://doi.org/10.1016/S0168-3659(99)00221-7.

[14] R.I. Litvinov, J.W. Weisel, Fibrin mechanical properties and their structural origins, Matrix Biol. 60–61 (2017) 110–123. https://doi.org/10.1016/j.matbio.2016.08.003.

[15] S.B. Ross-Murphy, Structure and rheology of gelatin gels, Imaging Sci. J. 45 (1997) 205–209. https://doi.org/10.1080/13682199.1997.11736407.

[16] L. Smith Callahan, Combinatorial Method/High Throughput Strategies for Hydrogel Optimization in Tissue Engineering Applications, Gels. 2 (2016) 18. https://doi.org/10.3390/gels2020018.

[17] C. Moraes, J.-H. Chen, Y. Sun, C. a Simmons, Microfabricated arrays for high-throughput screening of cellular response to cyclic substrate deformation., Lab Chip. 10 (2010) 227–234. https://doi.org/10.1039/b914460a.

[18] K. Chatterjee, S. Lin-Gibson, W.E. Wallace, S.H. Parekh, Y.J. Lee, M.T. Cicerone, M.F. Young, C.G. Simon, The effect of 3D hydrogel scaffold modulus on osteoblast differentiation and mineralization revealed by combinatorial screening, Biomaterials. 31 (2010) 5051–5062. https://doi.org/10.1016/j.biomaterials.2010.03.024.

[19] B. Mohanraj, C. Hou, G.R. Meloni, B.D. Cosgrove, G.R. Dodge, R.L. Mauck, A high throughput mechanical screening device for cartilage tissue engineering, J. Biomech. 47 (2014) 2130–2136. https://doi.org/10.1016/j.jbiomech.2013.10.043.

[20] C.A. Tweedie, D.G. Anderson, R. Langer, K.J. Van Vliet, Combinatorial material

mechanics: High-throughput polymer synthesis and nanomechanical screening, Adv. Mater. 17 (2005) 2599–2604. https://doi.org/10.1002/adma.200501142.

[21] X. Zhang, Y. Xiang, Combinatorial approaches for high-throughput characterization of mechanical properties, J. Mater. 3 (2017) 209–220. https://doi.org/10.1016/j.jmat.2017.07.002.

[22] T.J. Lujan, K.M. Wirtz, C.S. Bahney, S.M. Madey, B. Johnstone, M. Bottlang, A novel bioreactor for the dynamic stimulation and mechanical evaluation of multiple tissue-engineered constructs, Tissue Eng. - Part C Methods. 17 (2011) 367–374. https://doi.org/10.1089/ten.tec.2010.0381.

[23] D.J. Salvetti, C.J. Pino, S.G. Manuel, I. Dallmeyer, S. V. Rangarajan, T. Meyer, M. Kotov, V.P. Shastri, Design and validation of a compressive tissue stimulator with high-throughput capacity and real-time modulus measurement capability, Tissue Eng. - Part C Methods. 18 (2012) 205–214. https://doi.org/10.1089/ten.tec.2011.0233.

[24] D.S. Tzeranis, I. Panagiotopoulos, S. Gkouma, G. Kanakaris, N. Georgiou, N. Vaindirlis, G. Vasileiou, M. Neidlin, A. Gkousioudi, V. Spitas, G.A. Macheras, L.G. Alexopoulos, A device for high-throughput monitoring of degradation in soft tissue samples, J. Biomech. 74 (2018) 180–186. https://doi.org/10.1016/j.jbiomech.2018.04.040.

[25] E.C. Hobson, W. Li, B.A. Juliar, A.J. Putnam, J.P. Stegemann, C.X. Deng, Resonant acoustic rheometry for non-contact characterization of viscoelastic biomaterials, Biomaterials. 269 (2021) 120676. https://doi.org/10.1016/j.biomaterials.2021.120676.

[26] W.L.M. Nyborg, Acoustic Streaming, ACADEMIC PRESS INC., 1965. https://doi.org/10.1016/B978-0-12-395662-0.50015-1.

[27] J.L. Harden, H. Pleiner, P.A. Pincus, Hydrodynamic surface modes on concentrated polymer solutions and gels, J. Chem. Phys. 94 (1991) 5208–5221. https://doi.org/10.1063/1.460525.

[28] Y. Onodera, P.-K. Choi, Surface-wave modes on soft gels, J. Acoust. Soc. Am. 104 (1998) 3358–3363. https://doi.org/10.1121/1.423919.

[29] F. Monroy, Surface hydrodynamics of viscoelastic fluids and soft solids: Surfing bulk rheology on capillary and Rayleigh waves, Adv. Colloid Interface Sci. 247 (2017) 4–22. https://doi.org/10.1016/j.cis.2017.07.006.

[30] H. Takahashi, P.-K. Choi, Sol – Gel Transition in Gelatin Observed with Surface Waves, Jpn. J. Appl. Phys. 35 (1996) 2939–2943.

[31] M. Pieters, M. Guthold, C.M. Nunes, Z. De Lange, Interpretation and Validation of Maximum Absorbance Data Obtained from Turbidimetry Analysis of Plasma Clots, Thromb. Haemost. 120 (2020) 44–54. https://doi.org/10.1055/s-0039-1698460.

[32] V. Normand, S. Muller, J.C. Ravey, A. Parker, Gelation kinetics of gelatin: a master curve and network modeling, Macromolecules. 33 (2000) 1063–1071. https://doi.org/10.1021/ma9909455.

[33] S. Even-Ram, V. V. Artym, Extracellular Matrix Protocols, 2011.

[34] V. Normand, S. Muller, J.C. Ravey, A. Parker, Gelation kinetics of gelatin: a master curve and network modeling, Macromolecules. 33 (2000) 1063–1071. https://doi.org/10.1021/ma9909455.

[35] S.M. Lien, W. Te Li, T.J. Huang, Genipin-crosslinked gelatin scaffolds for articular cartilage tissue engineering with a novel crosslinking method, Mater. Sci. Eng. C. 28 (2008) 36–43. https://doi.org/10.1016/j.msec.2006.12.015.

[36] M.F. Butler, Y.F. Ng, P.D.A. Pudney, Mechanism and kinetics of the crosslinking reaction between biopolymers containing primary amine groups and genipin, J. Polym. Sci. Part A Polym. Chem. 41 (2003) 3941–3953. https://doi.org/10.1002/pola.10960.

[37] K. Yokoyama, N. Nio, Y. Kikuchi, Properties and applications of microbial transglutaminase, Appl. Microbiol. Biotechnol. 64 (2004) 447–454. https://doi.org/10.1007/s00253-003-1539-5.

[38] Y. Liu, R. Weng, W. Wang, X. Wei, J. Li, X. Chen, Y. Liu, F. Lu, Y. Li, Tunable physical and mechanical properties of gelatin hydrogel after transglutaminase crosslinking on two gelatin types, Int. J. Biol. Macromol. 162 (2020) 405–413. https://doi.org/10.1016/j.ijbiomac.2020.06.185.

[39] S.L. Rowe, S.Y. Lee, J.P. Stegemann, Influence of thrombin concentration on the mechanical and morphological properties of cell-seeded fibrin hydrogels, Acta Biomater. 3 (2007) 59–67. https://doi.org/10.1016/j.actbio.2006.08.006.

[40] S.L. Rowe, J.P. Stegemann, Microstructure and mechanics of collagen-fibrin matrices polymerized using ancrod snake venom enzyme, J. Biomech. Eng. 131 (2009) 1–9. https://doi.org/10.1115/1.3128673.

[41] A.S. Wolberg, Thrombin generation and fibrin clot structure, Blood Rev. 21 (2007) 131–142. https://doi.org/10.1016/j.blre.2006.11.001.

[42] P.A. Janmey, J.P. Winer, J.W. Weisel, Fibrin gels and their clinical and bioengineering applications, J. R. Soc. Interface. 6 (2009) 1–10. https://doi.org/10.1098/rsif.2008.0327.

[43] M.S. Weiss, B. Peñalver Bernabé, S. Shin, S. Asztalos, S.J. Dubbury, M.D. Mui, A.D. Bellis, D. Bluver, D.A. Tonetti, J. Saez-Rodriguez, L.J. Broadbelt, J.S. Jeruss, L.D. Shea, Dynamic transcription factor activity and networks during ErbB2 breast oncogenesis and targeted therapy., Integr. Biol. (Camb). 6 (2014) 1170–82. https://doi.org/10.1039/c4ib00086b.

[44] N.A. Kurniawan, J. Grimbergen, J. Koopman, G.H. Koenderink, Factor XIII stiffens fibrin clots by causing fiber compaction, J. Thromb. Haemost. 12 (2014) 1687–1696. https://doi.org/10.1111/jth.12705.

[45] E.L. Hethershaw, A.L. Cilia La Corte, C. Duval, M. Ali, P.J. Grant, R.A.S. Ariëns, H. Philippou, The effect of blood coagulation factor XIII on fibrin clot structure and fibrinolysis, J. Thromb. Haemost. 12 (2014) 197–205. https://doi.org/10.1111/jth.12455.

[46] E. Akpalo, V. Larreta-Garde, Increase of fibrin gel elasticity by enzymes: A kinetic approach, Acta Biomater. 6 (2010) 396–402. https://doi.org/10.1016/j.actbio.2009.08.001.

[47] J. Wedgwood, A.J. Freemont, N. Tirelli, Rheological and turbidity study of fibrin hydrogels, Macromol. Symp. 334 (2013) 117–125. https://doi.org/10.1002/masy.201300111.

Chapter 5 Summary and Future Work

RAR is a novel acoustic method that enables high-throughput, non-contact characterization of soft material mechanics. This dissertation describes the development, implementation, and validation of RAR, from initial theory to demonstration of its unique capabilities for exploring the physical transition during hydrogel gelation and enabling high-throughput mechanical testing in combinatorial studies. The rapid, non-contact measurements of RAR have the potential to provide new capabilities over conventional, contact-based mechanical testing in a variety of applications, making viscoelastic characterization not only easier, but faster, cheaper, and more consistent. This chapter summarizes the major findings of this dissertation and discusses future work, including the development of new analytical approaches to allow measurement of a wider variety of soft biomaterials and sample geometries, as well as algorithms to synthesize combinatorial measurements and apply them to the design of materials with tailored mechanical properties.

5.1 Summary of Dissertation and Conclusions

The initial work developing and validating the experimental and analytical methods used in RAR, is detailed in Chapter 2. We explained methods for generating and tracking resonant surface waves on confined hydrogels and were able to demonstrate that two parameters of the damped oscillations, the natural frequency and damping coefficient, were independent of the actual pushing force or duration. This indicates that RAR measurements are extremely robust to small differences in equipment or protocol; a claim that cannot be made about conventional mechanical testing approaches, where changes protocol for pre-strain or pre-conditioning are known to significantly alter results. We validated that these parameters could be used to calculate the intrinsic viscoelastic properties of the materials both computationally, using a custom FEA model of RAR surface excitation, and experimentally, by comparing viscoelastic measurements from RAR and conventional shear rheometry for fibrin, gelatin, and agarose hydrogels with shear moduli ranging from 0.1 to 30 kPa. Not limited to single measurements, we used RAR to repeatedly sample during the gelation of fibrin, showing that RAR was able to quantitatively measure viscoelastic properties in both stable and dynamic materials.

Moving past the initial validation of the technique, RAR was applied to characterizing the process of gelation in Chapter 3. Dynamic RAR studies were performed with a high sampling rate during the gelation of fibrin to identify changes in resonant oscillations with high temporal sensitivity. We were able to utilize these results to identify an abrupt shift between the types of surface waves as the gel moved from a liquid to solid state. With this knowledge we were then able to calculate the viscoelastic properties throughout the entire gelation process, starting as purely viscous fluid, developing into a viscoelastic fluid, and finally transitioning to a viscoelastic solid. An alternative protocol, rRAR, was developed to enable rapid sampling and allow for the dynamic measurements of gelation in UV crosslinked PEG-NB. This study demonstrated not only the ability to achieve sub-second temporal resolutions for characterizing fast reactions but to identify a brief phase of overdamped oscillations during the phase transition. While the exact mechanisms of this phenomena have not yet be identified, this finding highlights the importance of convenient, rapid mechanicals measurements in enabling exploratory mechanical testing. Finally, we were able to apply the observed resonant phenomena from the fibrin and PEG experiments to improve the traditional gel clot LAL assay, identifying the timing of phase transition to and allowing for endotoxin quantification.

While the dynamic RAR studies in Chapters 2 and 3 measured changes over seconds and minutes, RAR has the potential to continue longitudinal measurements over much longer time scales, as demonstrated in Chapter 4. Gelatin and fibrin gels were modified with chemical and enzymatic crosslinkers, tracking viscoelastic changes over hours and even days using RAR. Testing the combined roles of multiple hydrogel components in a combinatorial manner, we identified that not only the degree, but also the timing, of crosslinking can significantly alter the mechanics of a hydrogel. These finding resulted from over 15,000 individual RAR measurements that were conducted on hundreds of samples. Using conventional mechanical characterization, this many measurements could take months or even years to complete, however, because RAR does not rely on contact with materials, it was possible to conduct these longitudinal studies on hundreds of individual samples simultaneously with the entire study taking less than 2 weeks to complete. The combination of dynamic mechanical measurements with a high sample throughput, will enable RAR to facilitate mechanical testing and allow comprehensive and combinatorial studies on soft material design to become the norm.

This dissertation describes the development and first applications of a high-throughput, non-contact method for mechanical characterization in soft materials. Our results showcase the ability of RAR to measure viscoelastic material properties in a robust and quantitative manner, to utilize these rapid, non-destructive measurements for longitudinal mechanical tracking over various time scales, and to enable systematic and combinatorial material testing by expanding throughput. While these experiments have demonstrated RAR in relatively simple, well-studied material systems, they were crucial in validating its capabilities, allowing us to move forward in testing more complex and unknown materials. Despite all that has been demonstrated with RAR, this is still a new technique, and as such it will continue to undergo rapid development, providing new capabilities and improving upon those already present. No published technique has demonstrated the capability to simultaneously perform quantitative, non-contact, and high-throughput measurements, setting RAR apart as a powerfully flexible platform for a variety of mechanical testing applications.

5.2 Future Work

5.2.1 Clinical Applications

Appropriate blood coagulation is a critical element in hemostasis and wound healing, however abnormalities in this process, coagulopathies, can play a role in a variety of serious health conditions. This is particularly relevant in the wake of COVID-19, where associated coagulopathies are common and contribute to the severity of disease [1–4]. Currently, thromboelastography (TEG) is used for the dynamic assessment of blood elasticity by measuring the shear forces on a pin suspended in a rotating blood-filled cup [5]. Multiple quantitative measures, including thrombin generation (R), fibrin polymerization (K and α-Angle), maximum clot stiffness (MA), and fibrinolysis (LY30), can be extracted from the resulting mechanical information, (Fig 5.1). These parameters provide information on multiple stages in the process of coagulation, allowing clinicians to quickly understand the coagulative potential of a patient and determine the appropriate treatment regimen [5,6]. In chapters 2, 3, and 4, RAR is demonstrated to measure the gelation of fibrin gels, both with and without transglutaminase crosslinking.

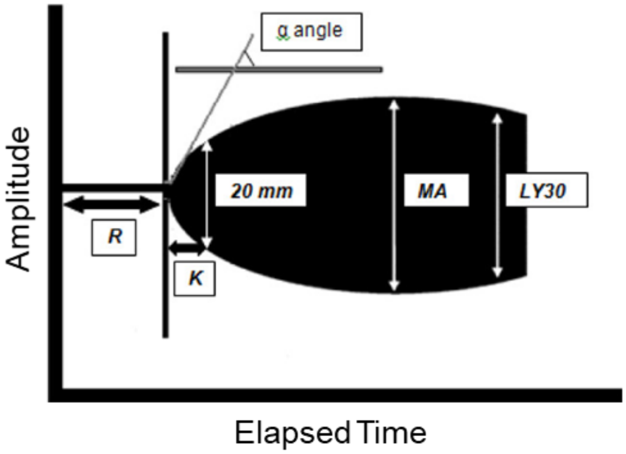

Figure 5.1: Example of TEG results showing amplitude changes over time during coagulation. Image adapted from original by Luis Teodoro da Luz, Bartolomeu Nascimento, and Sandro Rizoli, distributed under CC-BY 2.0 license.

A brief, proof-of-concept study was performed, tracking changing mechanical properties during the coagulation of citrated porcine blood following the addition 0.02M $CaCl_2$ using RAR (Figure 3.7). The clear similarities between the shape of a generic TEG curve and the dynamic RAR viscoelastic parameters indicates that these same clinically relevant parameters can be derived from RAR. However, RAR has a significant advantage of TEG in the smaller sample volume requirements (100 vs ~350 μL) and higher throughput using a microplate format. The rapid, non-contact measurements of RAR have the potential to allow for improved throughput in the mechanical measurements of blood coagulation, aiding both future research into the mechanisms and potential treatment of various coagulopathic disorders, as well as aiding in their clinical detection.

5.2.2 Longitudinal measurements in tissue engineered constructs

Chapters 3 and 4 demonstrate the capability of RAR to measure mechanical changes in soft materials over a variety of time scales, with sampling intervals ranging from seconds to days. This demonstration included not only the gelation of materials, but longitudinally monitoring subsequent mechanical changes in the material due to chemical and enzymatic crosslinking. While, as previously discussed, these studies provide important insight into the design of complex material systems, they also suggest the capability to extend these types of mechanical measurements to tissue engineering constructs with a live cellular component.

While traditional, contact-based methods have been applied for measuring the changing mechanical properties of cell laden hydrogels, these methods require the destruction of samples at each measured time point, multiplying the material and labor cost involved in a study [9]. Longitudinal measurements have been demonstrated in sealed, bioreactor systems but these systems are typically very low throughput and cannot be easily scaled up [10,11]. RAR, by taking non-contact measurements of samples in a separate sealed chamber, allows for longitudinal testing of multiple samples in a single plate or even multiple plates simultaneously. Reducing the experimental burden of viscoelastic characterization for tissue engineered constructs will not only improve our understanding of complex cell-matrix interactions in tissue engineering but may help to translate these discoveries to the clinic as a robust method for non-destructive quality control for tissue engineered products.

5.2.3 Intelligent material design

The capability for high-throughput viscoelastic material characterization using RAR helps to address a critical weakness in the design of combinatorial studies on soft materials [12]. New material systems are constantly being developed and modified for applications such as tissue engineering or drug delivery. A wide variety of material design parameters, from polymer concentration to the ionic strength of the liquid medium, have the potential to impact the mechanical properties, and therefore the functionality, of these materials [13,14]. Current studies that do explore mechanical changes with different materials typically explore the impact of design parameters individually, however, as was demonstrated in Chapter 4, these parameters can have synergistic effects on the final properties, requiring the use of combinatorial studies to explore the entirety of the multivariate parameter space. With a more complete understanding of these complex material systems, it will be possible to predict material formulations to optimize functional properties, such as elasticity, viscosity, degradation rate, or gelation kinetics [12,15].

While it is simple to optimize a material's design with regards to a single design parameter, tailoring the functional properties within a multiparameter design space will require not only the experimental capability to map the space, but computational tools to apply this knowledge [15]. This will involve the development of complex machine learning tools to synthesize the complex materials characterizations and designs and identify rules. Starting with multiple linear regression, or partial least squares regression to minimize issues with collinearity, it will be possible to identify the most important design variables for a given material property and to generate predictive models for designing new materials [16,17]. Additionally, as new materials are designed and implemented it will be possible to incorporate functional outcomes, such as the printability of bioinks or cell differentiation in a synthetic ECM, into this machine learning toolkit [15,18]. Many fields can benefit from a toolset to design soft materials, ranging from those traditionally associated with biomedical research, such as bioprinting or tissue engineering, to more industrial sectors, like food science or cosmetics. This approach for predicting, and iteratively optimizing, material function, by combining a novel, high-throughput testing modality with a complementary analysis pipeline, will allow for soft material research and development to move beyond the limitations of traditional ad-hoc design.

5.2.4 Future applications of RAR

There are a variety of potential applications where we plan to implement RAR testing. As briefly discussed in Chapter 1, resonant surface oscillations can be modeled as a vibrating membrane. While this is not the appropriate model for liquid oscillations, it could be applied to study the mechanics of thin films, such as cell sheets or even cellular monolayers. The measurement of mechanical properties in single layers of cells currently presents a substantial mechanical challenge, but it may be possible to utilize non-contact RAR measurements to study these systems. Cells could be cultured on the surface of soft non-degradable hydrogels or on a flexible membrane, such as a transwell. RAR could then be performed on this system, longitudinally measuring changes in surface oscillations due to the cellular membrane and utilizing models for surface waves in multilayer materials to calculate the mechanical properties. Prior studies of the cell monolayer mechanics have measured intercellular adhesion energy densities of 0.07 N/m. This is approximately the same as the surface energy of a water-air interface, 0.072 N/m, indicating that intercellular forces in cultured monolayers may similarly impact surface oscillations in soft gels or on soft membranes [19].

The high efficiency and throughput of RAR make it an ideal technique for industrial applications, such as in the food industry. Manufacturing processes for a wide variety of foods require control over the viscoelastic properties of the final product. RAR could be applied to the development of new products, enabling rapid mechanical testing to quantitatively identify textural difference between difference formulation or preparations. Additionally, RAR would be highly effective in quality control, detecting both the consistency of the manufacturing process and even identifying longitudinal mechanical changes that could indicate food safety concerns.

5.2.5 Implementation of multiple transducer arrays

While the current implementation of RAR is capable of markedly higher throughput in relation to any comparable mechanical testing technique, it could be further improved. When characterizing multiple samples in a microplate array the single, the two-element transducer moves from well to well, measuring each sample one at a time. This results in a substantial bottleneck in efficiency as the movement between wells takes approximately 1 second, nearly 10-times longer than the actual oscillatory measurement. To address this limitation, we will develop an array of transducers, as well as the necessary electrical driving hardware, to measure multiple samples simultaneously. The individual elements are only 5 mm in diameter and will be fitted with custom lens for point focusing. When spaced a minimum of 9 mm apart, the well spacing of a 96 well microplate, we expect minimal crosstalk, but, if present, we can double the spacing to every other well to further reduce any interference. While it may be possible to generate a full 96 transducer array, this is likely unnecessary and will result in a dramatic increase in cost and complexity for the updated RAR system. Instead, we will focus on the development of a 4 or 8 transducer array which can be quickly scanned over a microplate, reducing the measurement time required for a full 96-well plate from 2 minutes to 30 or even 15 seconds, respectively.

5.2.6 Increasing flexibility in sample size and geometry

The RAR studies detailed in Chapters 2-4 all were conducted with materials that had been cast directly into the microplates they were measured in. This ensured not only a cylindrical outer geometry, but a planar top surface due to the low-surface energy of the fluorosilicone coating. This controlled geometry was important for the analytical predictions of intrinsic material properties, with changes in the sample diameter or non-planar surface, impacting the resonant properties. While generally avoided in this initial exploration of RAR, these geometric changes can be unavoidable in situations where materials expand or contract, such as in the swelling or compaction often seen in acellular and cellular hydrogels. It may be possible to analytically account for surface concavity or convexity generated through these processes, using RAR thickness measurement to determine changes in surface geometry and applying then to analytical models from literature [20,21]. It will be important to introduce these corrections to the RAR analytical pipeline to increase the flexibility of this technique.

Changes in sample diameter have a significant effect on the surface oscillations generated during RAR. While this difference can be corrected analytically, as demonstrated in this thesis (Chapters 2 and 3), it may be beneficial to utilize this resonant difference to control the oscillation frequency independent of material properties. We can fabricate custom microplates with variable well diameters, allowing the systematic study of the frequency dependence of viscoelastic material properties using RAR. Additionally, we may be able to improve the range of material that can be measured, using larger or smaller diameters for stiffer or softer materials respectively to keep oscillation frequencies within the measurable range.

Additionally, it may be possible to expand RAR to materials that were not cast in the well of a microplate. It is likely possible to generate and measure resonant oscillation on the surface of soft material samples with a generally cylindrical shape, such as tissue biopsies, either inside or outside the well of a microplate. As described above, there will need to be changes to the RAR analytical process in order to accommodate geometric differences between samples or changes in the boundary condition for samples that are no longer bound to the walls of the microplate. While standard RAR measurements do not use the ultrasonic pulses to generate 2D or 3D images, it is very possible to adapt the protocol to include a 2D raster scan underneath a sample, enabling the 3D mapping of a sample's surface geometry. Deviation from a cylindrical geometry, if substantial, may potentially require a switch from the analytical models of propagating surface waves to the use of computational tools, such as FEA, in conjunction with the individually imaged 3D geometry to identify the relationships between resonant parameters and intrinsic material properties. Developing alternate methods for the analysis of RAR experimental results will enable the expansion of this technique to a greater range of soft biomaterials, from synthetic hydrogels to soft tissues.

5.3 References

[1] J.M. Connors, J.H. Levy, COVID-19 and its implications for thrombosis and anticoagulation, Blood. 135 (2020) 2033–2040. https://doi.org/10.1182/blood.2020006000.

[2] D. Giannis, I.A. Ziogas, P. Gianni, Coagulation disorders in coronavirus infected patients: COVID-19, SARS-CoV-1, MERS-CoV and lessons from the past, J. Clin. Virol. 127 (2020) 104362. https://doi.org/10.1016/j.jcv.2020.104362.

[3] X. Bi, Z. SU, H. Yan, J. Du, J. Wang, L. Chen, M. Peng, S. Chen, B. Shen, J. Li, Prediction

of severe illness due to COVID-19 based on an analysis of initial Fibrinogen to Albumin Ratio and Platelet count, Platelets. 31 (2020) 674–679. https://doi.org/10.1080/09537104.2020.1760230.

[4] J. Thachil, The protective rather than prothrombotic fibrinogen in COVID-19 and other inflammatory states, J. Thromb. Haemost. (2020) 1–4. https://doi.org/10.1111/jth.14942.

[5] V.G. Nielsen, R.T. Lyerly, W.Q. Gurley, The effect of dilution on plasma coagulation kinetics determined by thrombelastography is dependent on antithrombin activity and mode of activation, Anesth. Analg. 99 (2004) 1587–1592. https://doi.org/10.1213/01.ANE.0000136843.58799.AB.

[6] N.J. White, J.C. Newton, E.J. Martin, B.M. Mohammed, D. Contaifer, J.L. Bostic, G.M. Brophy, B.D. Spiess, A.E. Pusateri, K.R. Ward, D.F. Brophy, Clot formation is associated with fibrinogen and platelet forces in a cohort of severely injured emergency department trauma patients, Shock. 44 (2015) 39–44. https://doi.org/10.1097/SHK.0000000000000342.

[7] N. Tynngård, T. Lindahl, S. Ramström, G. Berlin, Effects of different blood components on clot retraction analysed by measuring elasticity with a free oscillating rheometer, Platelets. 17 (2006) 545–554. https://doi.org/10.1080/09537100600759238.

[8] J.C. Chapin, K.A. Hajjar, Fibrinolysis and the control of blood coagulation, Blood Rev. 29 (2015) 17–24. https://doi.org/10.1016/j.blre.2014.09.003.

[9] B.A. Juliar, J.A. Beamish, M.E. Busch, D.S. Cleveland, L. Nimmagadda, A.J. Putnam, Cell-mediated matrix stiffening accompanies capillary morphogenesis in ultra-soft amorphous hydrogels, Biomaterials. 230 (2020). https://doi.org/10.1016/j.biomaterials.2019.119634.

[10] T.J. Lujan, K.M. Wirtz, C.S. Bahney, S.M. Madey, B. Johnstone, M. Bottlang, A novel bioreactor for the dynamic stimulation and mechanical evaluation of multiple tissue-engineered constructs, Tissue Eng. - Part C Methods. 17 (2011) 367–374. https://doi.org/10.1089/ten.tec.2010.0381.

[11] D.J. Salvetti, C.J. Pino, S.G. Manuel, I. Dallmeyer, S. V. Rangarajan, T. Meyer, M. Kotov, V.P. Shastri, Design and validation of a compressive tissue stimulator with high-throughput capacity and real-time modulus measurement capability, Tissue Eng. - Part C Methods. 18 (2012) 205–214. https://doi.org/10.1089/ten.tec.2011.0233.

[12] L. Smith Callahan, Combinatorial Method/High Throughput Strategies for Hydrogel Optimization in Tissue Engineering Applications, Gels. 2 (2016) 18. https://doi.org/10.3390/gels2020018.

[13] S. Eggert, M. Kahl, N. Bock, C. Meinert, O. Friedrich, D.W. Hutmacher, An open-source technology platform to increase reproducibility and enable high-throughput production of

tailorable gelatin methacryloyl (GelMA) - Based hydrogels, Mater. Des. 204 (2021) 109619. https://doi.org/10.1016/j.matdes.2021.109619.

[14] R.I. Litvinov, J.W. Weisel, Fibrin mechanical properties and their structural origins, Matrix Biol. 60–61 (2017) 110–123. https://doi.org/10.1016/j.matbio.2016.08.003.

[15] J. Lee, S.J. Oh, S.H. An, W.D. Kim, S.H. Kim, S.H. Kim, Machine learning-based design strategy for 3D printable bioink: Elastic modulus and yield stress determine printability, Biofabrication. 12 (2020). https://doi.org/10.1088/1758-5090/ab8707.

[16] S. Wold, M. Sjöström, L. Eriksson, PLS-regression: A basic tool of chemometrics, in: Chemom. Intell. Lab. Syst., 2001: pp. 109–130. https://doi.org/10.1016/S0169-7439(01)00155-1.

[17] K.A. Janes, M.B. Yaffe, Data-driven modelling of signal-transduction networks, Nat. Rev. Mol. Cell Biol. 7 (2006) 820–828. https://doi.org/10.1038/nrm2041.

[18] D.E. White, J.B. Sylvester, T.J. Levario, H. Lu, J.T. Streelman, T.C. McDevitt, M.L. Kemp, Quantitative multivariate analysis of dynamic multicellular morphogenic trajectories., Integr. Biol. (Camb). 7 (2015) 825–33. https://doi.org/10.1039/c5ib00072f.

[19] A.R. Harris, L. Peter, J. Bellis, B. Baum, A.J. Kabla, G.T. Charras, Characterizing the mechanics of cultured cell monolayers, Proc. Natl. Acad. Sci. U. S. A. 109 (2012) 16449–16454. https://doi.org/10.1073/pnas.1213301109.

[20] R. Kidambi, Meniscus effects on the frequency and damping of capillary-gravity waves in a brimful circular cylinder, Wave Motion. 46 (2009) 144–154. https://doi.org/10.1016/j.wavemoti.2008.10.001.

[21] J.A. Nicolás, Effects of static contact angles on inviscid gravity-capillary waves, Phys. Fluids. 17 (2005) 1–10. https://doi.org/10.1063/1.1829111.

Appendix A: RAR Experimental Protocol

A.1 Summary

The experimental setup is prepared by connecting the required instruments and a setting up the heated water tank. Next, a custom MATLAB script is used to define instrument settings, input sample arrangement and contents, and align the microplate and transducer. A MATLAB structure is generated containing metadata describing exact protocol for each upcoming measurement, including sample names, geometries, 3D positions, ARF parameters, tracking parameters, and timings. Finally, once samples are prepared the RAR measurements are initiated, following the predefined protocol automatically.

A.2 Detailed Protocol

1) Prepare heated water tank.
    a) Degassing water.
        i) Fill 3.3-gallon acrylic vacuum chamber (BVV) 1/2 full with DI water.
        ii) Place on top of magnetic stir plate and begin stirring (~300rpm).
        iii) Apply vacuum (< 0.5 Bar) for at least 1 hour.
    b) Preheat water.
        i) Move degassed water tank to RAR setup.
        ii) Place copper coil heat exchanger in water tank.
        iii) Start flow of heating fluid (water) through coil.
            (1) Set heating fluid 1°C above desired tank temperature.
        iv) Insert thermometer into water tank.
    c) Wait until tank temperature reaches stable temperature.
        i) Adjust heating fluid temperature to until tank reaches desired temperature.
2) Connect instruments using BNC cables according to Figure 0.1
3) Turn on RAR equipment.
    a) Function generators (Agilent 33220A)
    b) Digital delay generator (BNC 565)
    c) 3D Motion System (Velmex VXM)
    d) Pulser/Reciever (Panametric 5900 PR)
        i) Settings
            (1) MODE: P/E

        (2) PRF: EXT-BNC
        (3) ENERGY: 1uJ
        (4) DAMPING: 50 Ohm
        (5) HP FILT = 3 MHz
        (6) LP FILT = 20 MHz
        (7) ATTENUATORS = 13.0 dB
        (8) GAIN: 26.0 dB
        (9) RF OUTPUT PHASE= 180°

4) Lower transducer into water tank.
   a) Approximately 2” below water surface.
   b) Minimum of 1” above tank bottom to protect cords (add water if needed).
5) Lower plate holder to water surface .
   a) LOWER SLOWLY AND DO NOT HIT TRANSDUCER.
   b) Submerge halfway.
   c) Secure in place with set screws.
6) Open “RAR_Measure_Picosocpe_*.m” script in MATLAB.
   a) Sperate scripts for each application.
      i) “UV” for rRAR with triggered UV illumination.
      ii) “multiRadius” for custom microplates with mixed sample sizes.
      iii) “Rapid” for standard high-throughput measurements .
7) Run Section 1: Initialize and Select Transducer Setup.
   a) Connects to instruments via GPIB and USB connections.
   b) Loads transducer properties and calibration data.
   c) Enter experiment name and save location when prompted.
8) Run Section 2: Initial Setup of Instruments.
   a) Automatically sets parameters for all instruments (except P/R)
   b) Enter water temperature when prompted.
      i) Used to calculated speed of sound for accurate alignment and motion estimation.
9) Run Section 3: Select Plate Arrangement.
   a) Select microplate type.
      i) 96-well, 48-well, 24-well, 12-well, 6-well or custom geometry.
   b) Define samples.
      i) Select wells containing samples.
      ii) Name samples.
         (1) Fill in name, prefix, and suffix.
         (2) Enter individually, by column, by row, or all selected wells.
10) Place empty plate into plate holder (A1 at upper right)
   a) Use suction to remove all air beneath plate
11) Run Section 4: Find Plate Zero at Top-Left.
   a) Zeros the 3D motion system to the upper left well (H1 for 96-well plate).
   b) Move the transducer roughly under highlighted well using on screen controls.
12) Run Section 5: Find Sample Positions.
   a) Automated alignment to define exact 3D position of each microplate well.
      i) 3 alignment modes.
         (1) Single well: Adjusts for plate translation relative to Velmex.
         (2) Corners: Adjusts for plate translation or rotation.

        (3) All wells: Adjusts for plate translation or rotation or warp.
13) Run Section 6: Adjust Windowing.
    a) Select alignment well.
    b) Displays pulse-echo RF signal.
        i) Verify that reflections from plate bottom near bottom collected range.
14) Run Section 7: Setup Data Acquisition.
    a) Define PRFs, ARF pressure, ARF duration, and timing of repeated measurements.
    b) Creates Matlab structure containing instructions for each RAR measurement.
15) Place samples plate into plate holder (A1 at upper right).
    a) Use suction to remove all air beneath plate.
16) Turn on power amplifier (Amplifier Research 75A250).
    a) Set gain to 2 o'clock position.
17) Prepare samples to measure.
    a) For static materials: just add plate seal.
    b) For dynamic materials:
        i) Mix hydrogel precursor solution (eg. Fibrinogen and Thrombin).
            (1) Start stopwatch after combination.
        ii) Pipette into the appropriate wells of microplate.
        iii) Add plate seal.
        iv) Wait until 60 seconds have passed.
18) Run Section 8: Run RAR.
    a) Completes RAR measurements according to predefined instructions.
        i) Moves transducer along plate bottom, measuring all samples at each time point.
        ii) Saves RF signal while moving transducer to reduce any delay.
    b) Pauses if current elapsed time is less than the desired sampling time.

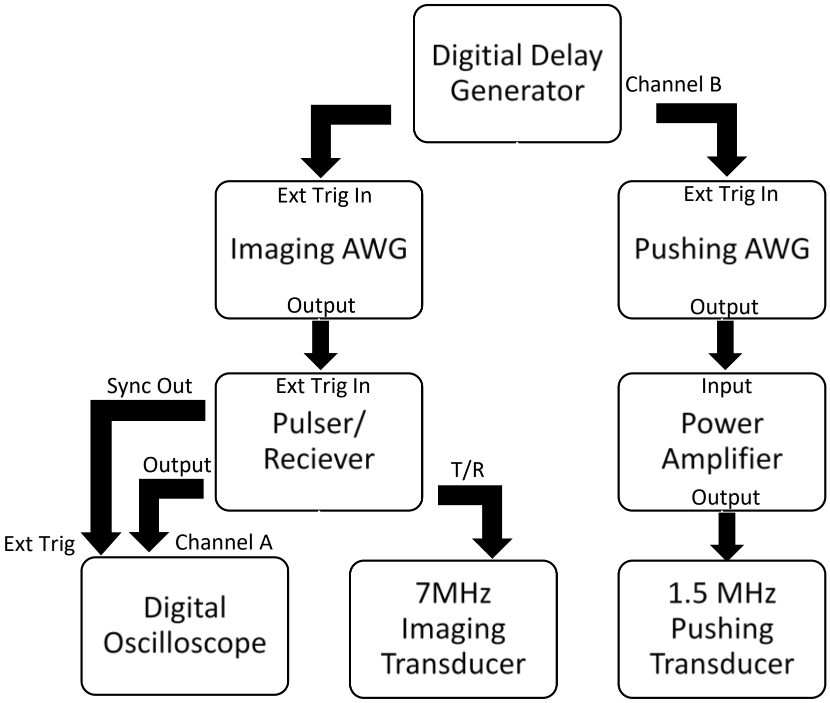

Figure A.1: Schematic of instruments and connections used in the RAR experimental setup.

Appendix B: RAR Analysis

B.1 **Summary**

The RAR analysis is performed using a set of custom MATLAB tools to measure displacements from pulse-echo RF data, find the resonant parameters to describe the surface oscillations using Fourier analysis, and calculate the viscoelastic properties of each sample at each measure time point. Figure 0.2 shows flow diagram of general analysis protocol.

B.2 Protocol

1) Start with "RAR_Interface_Analysis_*.m" script in MATLAB.
    a) Run Section 1.
        i) Select the directory(s) containing the RAR experimental data to be processed.
    b) Define processing parameters as true or false.
        i) "file_check"
            (1) True: Select of individual measurements or groups of measurements for processing.
            (2) False: Process all measurements in the selected directories.
        ii) "corr_check"
            (1) True: Checks for previously saved NCC uses those if available.
            (2) False: Performs NCC for all measurements (overwrite saved values).
        iii) "thick_plate"
            (1) True: Assumes a plate bottom thickness of ~1 mm in subsequent analysis.
            (2) False: Assumes a plate bottom thickness of ~0.3 mm in subsequent analysis.
    c) Run Section 2.
        i) Find displacements from first measurement.
            (1) Loads raw RF data.
            (2) Use peak fitting to locate reflections from plate-sample and sample-air interfaces.
            (3) Define control A-line from average of pre-deformation echoes.
            (4) Measure time-shift in interface reflections.
                (a) Define a 10-wavelength window around the top or bottom sample surface for the averaged control and first individual A-line.
                (b) Calculate lag in reflection using NCC.
                (c) Repeat for each A-line.
            (5) Calculate displacements from NCC using the known RF sampling rate and speed of sound at the sample temperature.
        ii) Repeat for all measurements.
2) Use "RAR_FFT_Processing.m" function in MATLAB.

a) Define the directory(s) containing the processed RAR data.
b) Find resonant parameters.
  i) Run FFT of each displacement time-series to generate power spectrums.
  ii) Fit position and HWHM of highest amplitude Lorentzian peak.
    (1) Damping (Γ) = HWHM for a rectangular window (apply correction for other windows).
    (2) Natural Frequency (ω_0) = $\sqrt{Peak\ Position^2 + Damping^2}$
  iii) Repeat for all measured displacement time-series.
c) Reorder resonant parameters to sort longitudinal measurements for each sample.
d) Calculate the viscoelastic properties for each sample at each time point.
  i) Use wave dispersion models as described in chapters 2-3.

3) Perform subsequent analysis of viscoelastic dynamics, including:
a) Crossover detection using Damping threshold.
b) Exponential or logistic fitting of combined shear modulus kinetics

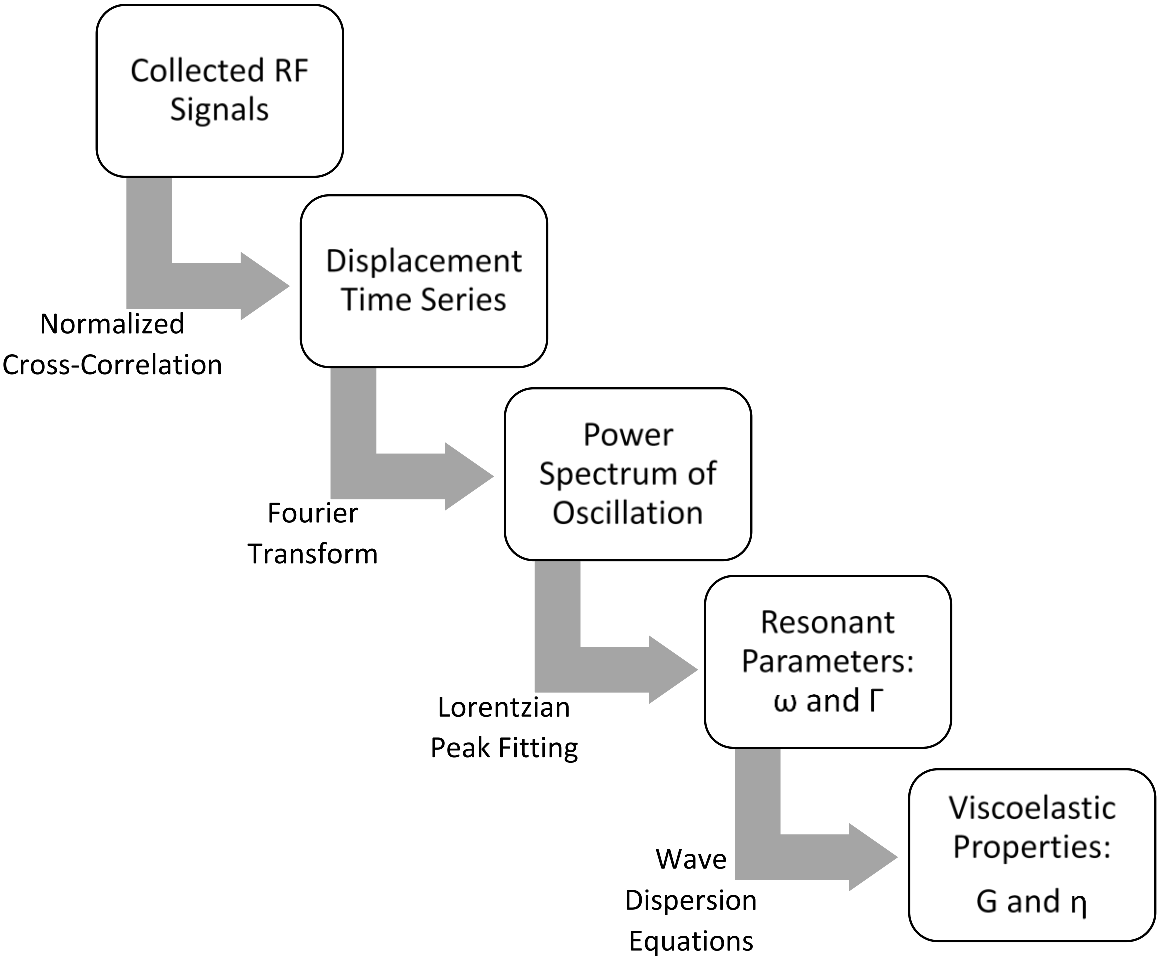

Figure B.1: Flowchart of the overall process for RAR analysis.